

Investigation of novel quasiparticles in topological materials

Dissertation

zur Erlangung des Doktorgrades der Naturwissenschaften
(Dr. rer. nat.)

der

Naturwissenschaftlichen Fakultät II
Chemie, Physik und Mathematik

der Martin-Luther-Universität
Halle-Wittenberg

vorgelegt von

Herr **Hao Yang**

geb. am 18.02.1991 in Jiangxi, China

Gutachter:

1. Prof. Dr. Stuart S. P. Parkin
2. Prof. Dr. Ingrid Mertig
3. Prof. Dr. Deng-Feng Li

Verteidigungsdatum: 17.10.2019

“学而不思则罔，思而不学则殆”
*(To learn without thinking is blindness,
to think without learning is idleness)*

孔子 Confucius
551-479 BC

Contents

Contents	iii
List of Figures	v
Abbreviations	vii
Abstract	ix
1 Introduction	1
1.1 Topological materials	1
1.2 Outline of the Thesis	4
2 Numerical methods	6
2.1 <i>Ab-initio</i> calculations based on density functional theory	6
2.1.1 Hohenberg-Kohn theorem	8
2.1.2 Kohn-Sham equation	9
2.1.3 Exchange-correlation interaction	10
2.1.4 Spin-orbit interaction	11
2.2 Green's functions	13
2.2.1 Introduction of the method of Green's functions	13
2.2.2 Green's functions for Schrödinger equation	14
2.2.3 Green's functions for surface states	16
3 Berry curvature	20
3.1 Basic concepts of Berry curvature	20
3.2 Berry curvature correction to the semiclassical equations of motion	24
3.2.1 Bloch theorem in crystalline solids	24
3.2.2 Intrinsic electronic transports and Berry curvature correction	25
3.2.3 Anomalous Hall effect and spin Hall effect	28
3.3 Symmetry analysis of Berry curvature	29
4 Quasiparticles in condensed materials	32

4.1	Weyl fermions	32
4.1.1	Introducation	32
4.1.2	Topological charge	36
4.1.3	Symmetry of Weyl fermions	37
4.1.4	Fermi arcs	39
4.2	Dirac fermions	41
4.2.1	Dirac fermions in three-dimensional materials	41
4.2.2	Surface states of Dirac semimetals	43
4.3	Triple point fermions	44
4.3.1	Triple point fermions in three-dimensional materials	45
4.3.2	Topological invariants and surface states	46
5	Selected results	50
5.1	Introduction	50
5.2	Paper I: Topological Weyl semimetals in the chiral antiferromagnetic materials Mn_3Ge and Mn_3Sn	50
5.3	Paper II: Strong anisotropic anomalous Hall effect and spin Hall effect in the chiral antiferromagnetic compounds Mn_3X ($X= Ge, Sn, Ga, Ir, Rh,$ and Pt)	59
5.4	Paper III: Prediction of triple point fermions in simple half-Heusler topological insulators	69
5.5	Paper IV: Quantum oscillations in the type-II Dirac semi-metal candidate $PtSe_2$	85
6	Summary	93
	Bibliography	96
	Publications	107
	Acknowledgements	109
	Curriculum Vitae	111
	Eidesstattliche Erklärung	113

List of Figures

2.1	The schematic figure of a half-infinite surface	17
3.1	Berry curvature under time-reversal, inversion and mirror symmetries. . .	31
4.1	Energy dispersions of Weyl equations with positive and negative signs . .	34
4.2	Energy dispersions of two types of Weyl points.	35
4.3	Topological charges of Weyl points.	36
4.4	Berry curvature distribution near two opposite Weyl points.	37
4.5	Weyl points under inversion, time-reversal and mirror-reflection symmetries.	38
4.6	Origin of Fermi arcs in the WSM.	40
4.7	Surface states on the surface of topological DSM which originates from band inversion or accidental band crossings.	44
4.8	Energy dispersions and topological charges of TPFs.	47

Abbreviations

AFM	Antiferromagnetic
AHE	Anomalous Hall effect
AHC	Anomalous Hall conductivity
ARPES	Angle-resolved photoemission spectroscopy
BZ	Brillouin Zone
BO	Bohn-Oppenheimer
DFT	Density functional theory
DWN	Double-Weyl node
FCC	Face-centered cubic
FM	Ferromagnetic
GGA	Generalized gradient approximations
LDA	Local density approximations
LDOS	Local density of states
LSDA	Local spin density approximations
MLWFs	Maximally localized Wannier functions
MR	Magnetoresistance
PDEs	Partial differential equations
QHE	Quantum Hall effect
QSHE	Quantum spin Hall effect
SGF	Surface Green's functions
SHC	Spin Hall conductivity

SHE	Spin Hall effect
SOI	Spin-orbit interaction
SOC	Spin-orbit coupling
TI	Topological insulator
TMD	Transition-metal dichalcogenides
TPF	Triple point fermion
TPFM	Triple point fermion metal/semimetal
TRIM	Time-reversal invariant momentum
TSM	Topological semimetal/metal
WSM	Weyl semimetal
3D	Three-dimensional
2D	Two-dimensional
<i>xc</i>	exchange and correlation

Abstract

In the present thesis, the electronic properties of three types of quasiparticles are investigated in topological non-trivial materials: Weyl fermions, triple point fermions and Dirac fermions. Theoretical calculations of electronic band structures for these systems are performed by means of *ab-initio* methods and in the framework of Density functional theory. The related topological invariants are calculated based on Berry curvature concept within the basis of maximum localized Wannier functions. The electronic transport properties of the Weyl metals, such as the intrinsic anomalous Hall effect (AHE) and spin Hall effect, are analyzed and calculated using Kubo formula. To investigate the surface states originating from these quasiparticles, both a half-infinite surface model and a slab model are utilized and give consistent results. The prior model is performed using a Green's function technique and the latter via the *ab-initio* methods. Some of our predictions have been observed experimentally, such as the AHE in Mn_3Ge and the quantum oscillations in PtSe_2 , while others still require experimental verification.

Chapter 1

Introduction

1.1 Topological materials

Topology is a fundamental branch of mathematics. It is used to study the qualitative properties of certain objects by abstracting those properties that are invariant under a certain kind of continuous transformation. For a long time, these concepts evaded the attention of most physicists, even though some topological effects, such as the quantum Hall effect (QHE), were uncovered in the 1980s[1–3]. It was only in the past few years that researchers begin to realize that topology can be a key attribute of condensed-matter and that it might be responsible for a variety of novel effects.

In the mathematical field of geometric topology, geometric quantities, such as angle, length and curvature, vary under continuously adiabatic transformations, whereas quantities such as the number of holes of an object, will not change. From this aspect, an orange and a spoon are topologically the same because the shape of the orange can be smoothly deformed into the shape of the spoon without creating a hole. In this sense, a cup with a handle has a hole and is therefore topologically different from the one without a handle.

In solid-state physics, the electron is described by the wavefunction which encodes information of the particle's spin, charge, and momentum. Counterintuitively, if the variables of a wavefunction in the parameter space trace back to itself on a closed parameter space loop, the wavefunction will not necessarily be the same as the initial state — namely, the wavefunction can be multivalued. The use of a gauge transformation shows that the multivalued wavefunction along this loop is equivalent to a single-valued wavefunction along a closed loop enclosing a charged particle. This particle gives rise to a constant flux of a pseudovector[4]. The flux, which is nothing but the Berry phase, is independent of the path, allowing us to claim that it is topological in nature [5]. In the field of solid states physics, materials with occupied electron wavefunctions that consist of the previously mentioned properties are termed topological materials [6, 7].

Topological materials have emerged as one of the most significant frontiers in condensed-matter physics in the last two decades. It is of strong interests because many of the non-trivial topological states are intimately linked with a verity of phenomena, such as the novel topological surface states, suppressed backscattering, peculiar transport properties, and low-energy excited quasiparticles which are analogues of particle physics.

The first observation of topological effect, namely the quantum Hall effect, was in a two-dimensional (2D) insulating system [1]. Until the mid-2000s, the QHE has been seen only in the presence of a strong magnetic field, which breaks the time-reversal symmetry. However, several groups have realized that the internal interaction between the electrons and the atomic nuclei could provide the effective magnetic field and thus realize this topological state, that gives rise to the quantum spin Hall effect (QSHE) [8–10]. Unlike the QHE, the time-reversal symmetry in QSHE is not broken. Moreover, instead of one helix edge state in the QHE system, the QSHE system has two helix edge states, in which the up and down spins propagate in opposite directions. Soon after that, the QSHE in 2D materials was generalized to three-dimensional (3D) materials, leading to the emergent area of “topological insulators” (TIs) [6, 7, 11–13]. One of the

most striking phenomena in TIs is the time-reversal symmetry protected surface states which host the 2D Dirac points.

Furthermore, the recent research progress verifies that not only in insulating systems but also in metal/semimetal materials, new types of topological states can exist. These topological states are related to the band crossings of the band structure and can give rise to fundamentally new physical phenomena. This has stimulated tremendous research interests in topological semimetals/metals (TSM), such as Weyl, Triple points, Dirac [14, 15] and nodal line semimetal/metal [16–21], as a new frontier of condensed matter physics after the discovery of TIs.

Among those discoveries, the point type topological band crossings form the quasiparticles in condensed matter and are of particular interests. Some of them have the same Hamiltonian as particles in high-energy physics such as Dirac points and Weyl points, making the corresponding TSMs ideal platforms for studying high-energy particles. Although the triple point has no analogue of the standard model in particle physics, it is topologically important since it acts as the charged particle enclosed by the loop as previously mentioned. Moreover, these three types of quasiparticles give special surface states, the so-called Fermi arcs, which are related to the special performance of TSMs under electric and magnetic fields. Due to their peculiar properties, the TSMs are proposed as promising candidates for various applications in spintronics.

In the present thesis, each of the quasiparticles is investigated by theoretical calculations. Firstly, as a complement to the previous studies of the Weyl semimetal/metal family, we proposed the possibility of finding Weyl points in the non-collinear antiferromagnetic system and studied their transport properties. Secondly, for the triple points, we showed that they can stably exist in the cubic structure system, which is in short of experimental verification. Due to the highly symmetric cubic system, more triple points will be projected to the surface without breaking the C_{3v} symmetry and it will be experimentally feasible to observe, compared with the previous hexagonal system.

Finally, in combination with quantum oscillation experiments, we validated the band structure calculation and the existence of Dirac points in PtSe₂.

1.2 Outline of the Thesis

The present work reports the selected *ab – initio* investigations of the quasiparticles in topological materials, including the Weyl fermion, the triple point fermion and the Dirac fermion. This thesis is structured as follows. The second chapter details a brief primer on density functional theory (Sec. 2.1) and the method of Green’s functions (Sec. 2.2), which is followed by an introduction to the basic concepts of Berry curvature in Chapter 3. This chapter aims to provide the most fundamental description of the origin (Sec. 3.1) and symmetry (Sec. 3.2) of Berry curvature, as well as its correction to electronic velocity (Sec. 3.3). Lastly, we introduce the recent research progress and properties of the Weyl fermion (Sec. 4.1), Triple point fermion (Sec. 4.3) and Dirac fermion (Sec. 4.2) in crystalline materials in Chapter 4.

The results of this thesis are given in form of four publications Paper I-IV (Chapter 5), which appeared in peer-reviewed journals. Each of them addresses one of the three quasiparticles of interest and can be classified according to the symmetry of the materials. If either the time reversal or the inversion symmetry is broken, Weyl fermion may exist. We demonstrate that the chiral antiferromagnetic (AFM) ordered compounds Mn₃Ge and Mn₃Sn are Weyl metals in **Paper I**, and that they have non-zero intrinsic anomalous Hall conductivity (AHC) and spin Hall conductivity (SHC) in **Paper II**.

Crystalline symmetries can also play an important role in forming topological quasiparticles. In **Paper III** we propose the possibility of finding triple point fermions in cubic half-Heusler compounds, which host four C₃ axes, and indeed we found several candidates which call for verification from experiments.

Preserving both time reversal and inversion symmetries, PtSe₂ is predicted to hold type-II Dirac nodes. In **Paper IV**, the electronic structure and Fermi surface of PtSe₂

are calculated theoretically and studied experimentally by quantum oscillations. The excellent agreement between the calculations and the experiments confirm the existence of Dirac fermions in the transition-metal dichalcogenides (TMD) materials.

Chapter 2

Numerical methods

2.1 *Ab-initio* calculations based on density functional theory

Schrödinger equation is the basic equation for describing the microscopic physical system and calculating the physical properties of materials. It has the form:

$$\hat{H}\Psi(\mathbf{R}, \mathbf{r}, t) = i\hbar \frac{\partial}{\partial t} \Psi(\mathbf{R}, \mathbf{r}, t), \quad (2.1)$$

where \mathbf{r} represents the set of all the electronic coordinations $\{\mathbf{r}_i\}$, \mathbf{R} represents the set of all nuclear coordinations $\{\mathbf{R}_j\}$. The Hamiltonian \hat{H} is the sum of kinetic and potential energy operators of all the particles in the system, in which the potential energy includes the internal interactions and the external field.

In the absence of external potential, the Hamiltonian can be expressed as:

$$\begin{aligned}
\hat{H} &= \hat{T}_N + \hat{T}_e + \hat{V}_{NN} + \hat{V}_{ee} + \hat{V}_{Ne} \\
&= - \sum_I \frac{\hbar^2}{2M_I} \nabla_I^2 - \sum_i \frac{\hbar^2}{2M_i} \nabla_i^2 + \frac{e^2}{2} \sum_I \sum_{J \neq I} \frac{Z_I Z_J}{|\mathbf{R}_I - \mathbf{R}_J|} \\
&\quad + \frac{e^2}{2} \sum_i \sum_{j \neq i} \frac{1}{|\mathbf{r}_i - \mathbf{r}_j|} - e^2 \sum_I \sum_j \frac{Z_I}{|\mathbf{R}_I - \mathbf{r}_j|}.
\end{aligned} \tag{2.2}$$

Here the first and the second terms are the kinetic energy of nuclei and electrons, respectively. The rest of the terms account for nuclear-nuclear interactions, electron-electron interactions and electron-nuclear interactions, respectively. This is a many-body problem which requires the solution of an equation with $3N$ spatial degrees of freedom and time.

In the case of a time-independent Hamiltonian \hat{H} , the static wavefunction satisfies the following stationary Schrödinger equation:

$$\hat{H}\Psi(\mathbf{R}, \mathbf{r}, t) = E\Psi(\mathbf{R}, \mathbf{r}). \tag{2.3}$$

However, the stationary Schrödinger equation still has $3N$ spatial degrees of freedom. In real-world system, the computational complexity can be huge, which makes the exact solution unreachable. In practice, to solve for the ground state, one has to use the Born-Oppenheimer (BO) approximation which first solves a conditional electronic Schrödinger equation:

$$\hat{H}_{BO}\Phi_{\mathbf{R}}(\mathbf{r}) = E_{BO}(\mathbf{R})\Phi_{\mathbf{R}}(\mathbf{r}), \tag{2.4}$$

where $\hat{H}_{BO} = \hat{H} - \hat{T}_N$. Here $E_{BO}(\mathbf{R})$ is called the ground BO potential energy surface and is a function of nuclear coordinations. Therefore, the ground state of the electronic wavefunction can be calculated by minimizing $E_{BO}(\mathbf{R})$. Then the total wavefunction can be expressed as:

$$\Psi(\mathbf{R}, \mathbf{r}) = \Theta(\mathbf{R})\Phi_{\mathbf{R}}(\mathbf{r}), \tag{2.5}$$

where $\Theta(\mathbf{R})$ is called the nuclear wavefunction and satisfies the nuclear dynamic equation.

$$\left[\hat{T}_N + E_{BO}(R)\Theta(\mathbf{R}) \right] = E\Theta(\mathbf{R}). \quad (2.6)$$

Since the nuclear mass is much larger than the electronic mass, in most cases, the dynamic equation of the nuclei can be treated classically and only the electronic equation needs to be considered. Despite this simplification, when the system becomes a bit more complicated, the computational cost is formidable.

2.1.1 Hohenberg-Kohn theorem

Density-functional theory (DFT) has achieved great progress in computational science, making the calculation of complex system possible. Instead of using the wavefunction, the ground-state electron density is used as the basic variable in DFT. Thus, the degree of freedom of the system decreases from $3N$ to 3 , making DFT the most widely used method for electronic structure calculations. Although this theory was originated from the Thomas-Fermi model, it was first justified by Pierre Hohenberg and Walter Kohn in the framework of the two Hohenberg-Kohn theorems (HK theorems)[22]:

HK theorem 1: There exists one to one mapping between the external potential and the electron density.

HK theorem 2: The ground state energy and density in a given external potential can be simply determined by the minimization of a universal energy functional of density.

Based on these two theorems, the energy functional of a system is:

$$E[n] = \int v(\mathbf{r})n(\mathbf{r})d\mathbf{r} + \frac{1}{2} \iint \frac{n(\mathbf{r})n(\mathbf{r}')}{|\mathbf{r} - \mathbf{r}'|} d\mathbf{r}d\mathbf{r}' + G[n], \quad (2.7)$$

where $v(\mathbf{r})$ is the external potential from the nuclei, $G[n]$ is a universal function of the density. The correct density function $n(\mathbf{r})$ will minimize the energy functional and gives the ground state.

2.1.2 Kohn-Sham equation

The HK theorems provide the proof and approach to calculate the ground state of a system. However, it has no guidance to construct the density functionals. Kohn and Sham (KS) [23] proposed a scheme of separating the energy functional as the sum of the kinetic energy of a non-interacting electron ($T_s[n]$), the classical static Coulomb repulsion energy of the density, and the exchange and correlation (xc) energy of the interacting system ($E_{xc}[n]$).

$$E[n] = \int v(\mathbf{r})n(\mathbf{r})d\mathbf{r} + \frac{1}{2} \iint d\mathbf{r}d\mathbf{r}' \frac{n(\mathbf{r})n(\mathbf{r}')}{|\mathbf{r} - \mathbf{r}'|} + T_s[n] + E_{xc}[n]. \quad (2.8)$$

Since the kinetic energy of the non-interaction system is not the exact kinetic energy of the system of interest, the difference is merged into the xc term. $E_{xc}[n]$ is very complicated in principle, but if the density is sufficiently slowly varying, the $E_{xc}[n]$ can be simplified to:

$$E_{xc}[n] = \int n(\mathbf{r})\epsilon_{xc}d\mathbf{r}, \quad (2.9)$$

where ϵ_{xc} is the xc energy density of a uniform electron gas. Higher order corrections to ϵ_{xc} can be added if necessary. After applying the stationary condition $\int \delta n(\mathbf{r})d\mathbf{r} = 0$ and performing the variation, we arrive at the famous Kohn-Sham equation:

$$\left\{ -\frac{1}{2}\nabla^2 + [v(\mathbf{r}) + \int \frac{n(\mathbf{r}')}{|\mathbf{r} - \mathbf{r}'|}d\mathbf{r}' + u_{xc}(n(\mathbf{r}))] \right\} \psi_i(\mathbf{r}) = \epsilon_i \psi_i(\mathbf{r}). \quad (2.10)$$

Here $u_{xc} = d(n(\mathbf{r})\epsilon_{xc})/dn$ is the xc potential of a uniform gas with density $n(\mathbf{r})$. ψ_i and ϵ_i are called the Kohn-Sham orbital and orbital energy, respectively. For a system with N electrons the density is calculated via:

$$n(\mathbf{r}) = \sum_i^N |\psi_i(\mathbf{r})|^2. \quad (2.11)$$

2.1.3 Exchange-correlation interaction

As we can see, until now, not many approximations are used. The solution of the Kohn-Sham equation is exact if we could find the correct xc potential. Unfortunately, the exact form of the xc potential is still unknown, and approximations are needed. The homogeneous electron gas can be described as one limit of solids. In this limit, the local density approximations (LDA)[22] are suitable approximations.

The LDA assume that the xc energy density ϵ_{xc} is only related to the value of charge density in space and neglects the fluctuation of charge density. Under these approximations, the xc energy density of the system of interest is replaced by that of the homogenous electron gas:

$$E_{xc}^{LDA}[n] = \int n(\mathbf{r})\epsilon_{xc}^{hom} d\mathbf{r}. \quad (2.12)$$

In LDA, the xc energy density can be separated into the exchange and correlation parts:

$$\epsilon_{xc} = \epsilon_x + \epsilon_c. \quad (2.13)$$

If the spin polarization is considered in the system, the local spin density approximations (LSDA) are straightforwardly generalized by neglecting the exchange interaction between the electrons with the opposite spin. Under this assumption, the exchange part of xc energy is expressed as:

$$E_x^{LSDA}[n_\uparrow, n_\downarrow] = \sum_{\sigma=\uparrow,\downarrow} \int \epsilon_x(n_\sigma)n_\sigma(\mathbf{r})d\mathbf{r}. \quad (2.14)$$

In particular, the exchange energy density is given by

$$\epsilon_x(n_\sigma) = -\frac{3}{2} \left(\frac{3}{4\pi} \right)^{\frac{1}{3}} n_\sigma^{\frac{1}{3}}(\mathbf{r}). \quad (2.15)$$

And the correlation part can be calculated from homogenous electron gas using Monte-Carlo approach. Although LDA (LSDA) look very simple, they can sometimes give very good results, especially in predicting the crystal structure and mechanical properties of materials. But for the system where the charge density is very localized, these approximations can result in a large deviation. To reduce the deviation of LDA (LSDA), the generalized gradient approximations (GGA) were developed, in which the gradient of charge density was introduced. The xc energy of GGA is expressed as:

$$E_{xc}^{GGA} = \int n(\mathbf{r}) \epsilon_{xc}[n(\mathbf{r})] d\mathbf{r} + \int F_{xc}[n(\mathbf{r}), \nabla n(\mathbf{r})] d\mathbf{r}, \quad (2.16)$$

where the functional $F_{xc}[n(\mathbf{r}), \nabla n(\mathbf{r})]$ accounts for the contribution from the gradient of charge density. Because of this improvement, the GGA approach has a better performance in the description of energy calculation and is one of the most widely used approximations in DFT.

2.1.4 Spin-orbit interaction

The Schrödinger equation is the basic equation that describes a physic system in which the quantum effects are significate. However, since The Schrödinger equation does not consider the relativistic effect, it can make errors in certain cases. For example, in some heavy metals, where the valence electrons move fast around the nuclei and have the characteristic of spin, the relativistic effect should be taken into consideration. The equation describing relativistic particle is called the Dirac equation, given by:

$$\hat{H}_D \Psi = E \Psi \quad \hat{H}_D = c\boldsymbol{\alpha} \cdot \hat{\mathbf{p}} + \beta mc^2 + V, \quad (2.17)$$

where V is the potential the particle experienced, β and α are matrices:

$$\beta = \begin{bmatrix} I & 0 \\ 0 & -I \end{bmatrix} \quad \alpha^i = \begin{bmatrix} 0 & \sigma^i \\ \sigma^i & 0 \end{bmatrix}.$$

Let $\Psi = \begin{pmatrix} \psi_1 \\ \psi_2 \end{pmatrix}$ in compact notation, both ψ_1 and ψ_2 have two components. This yields:

$$(E' - V)\psi_1 - c\boldsymbol{\sigma} \cdot \mathbf{p}\psi_2 = 0 \quad \text{with } E' = E - mc^2. \quad (2.18)$$

Substituting ψ_2 by ψ_1 in Eqn. 2.17 and expanding the power series in $(mc)^{-2}$ to the first order in the non-relativistic limit, we obtain:

$$\left[\frac{p^2}{2m} + V - \frac{\mathbf{p}^4}{8m^3c^2} + \frac{\hbar}{4im^2c^2}(\nabla V \cdot \mathbf{p}) + \frac{\hbar}{4m^2c^2}(\nabla V \times \mathbf{p}) \cdot \boldsymbol{\sigma} \right] \psi_1 = E' \psi_1. \quad (2.19)$$

Here the condition $E' - V \approx \frac{p^2}{2m}$ in non-relativistic limit is applied. The first two terms constitute the simple non-spin non-relativistic Hamiltonian. The third term gives the first-order relativistic correction and can be neglected. The fourth term is a similar relativistic correction to the potential energy and doesn't have a simple classical analog. The fourth term gives a small contribution to the energy of states whose eigenfunctions are nonzero at singularities of V and can also be neglected [24]. Finally, we obtain the Schrödinger form of Dirac equation:

$$\left[\frac{p^2}{2m} + V + \frac{\hbar}{4m^2c^2}(\nabla V \times \mathbf{p}) \cdot \boldsymbol{\sigma} \right] \psi_1 = E_k \psi_1. \quad (2.20)$$

Comparing with the Schrödinger equation, an additional term which couples the momentum of the electron with its spin appears. This term is the result of spin-orbit interaction (SOI) and can be a key cause of some phenomena in quantum physics, like

the fine structure of atomic energy levels, magnetocrystalline anisotropy and the spin Hall effect.

2.2 Green's functions

2.2.1 Introduction of the method of Green's functions

There is a wide range of topics in solving the linear partial differential equations (PDEs) because of its frequent usages in modern science, such as sound, heat, electrostatics, electrodynamics, fluid dynamics, elasticity, or quantum mechanics. The method of Green's function is one of the most powerful methods for solving PDEs. Considering the equation to be solved:

$$\hat{L}_x u(x) = f(x), \quad (2.21)$$

we can define a Green's function which satisfies:

$$\hat{L}_x G(x, y) = \delta(x - y), \quad (2.22)$$

Here $\delta(x - y)$ is the Dirac delta function and \hat{L}_x is the linear differential operator acting on x . Combining the properties of delta function with Eqn.2.21 and Eqn.2.22, we obtain:

$$\begin{aligned} \hat{L}_x u(x) &= f(x) \\ &= \int \delta(x - y) f(y) dy \\ &= \int \hat{L}_x G(x, y) f(y) dy. \end{aligned} \quad (2.23)$$

Since \hat{L}_x is linear and acts on x , it can be taken out of the integral on the left side, yielding:

$$\hat{L}_x u(x) = \hat{L}_x \int G(x, y) f(y) dy. \quad (2.24)$$

Finally we get:

$$u(x) = \int G(x, y)f(y)dy + \phi(x). \quad (2.25)$$

Where $\phi(x)$ is an arbitrary function which satisfies $\hat{L}_x\phi(x) = 0$. It is defined by the boundary condition of the system of interest and can be eliminated by an appropriate choice of $G(x, y)$. Therefore, the method of Green's functions transfers the linear PDE to an integral as shown in Eqn.2.24. The problem now boils down to finding a Green's function which satisfies Eqn.2.22. Green's functions for some common PDEs are known already. Although sometimes obtaining an appropriate Green's function can be very difficult, it provides a theoretically exact result.

2.2.2 Green's functions for Schrödinger equation

After the brief introduction of the method of Green's functions, in this section, we will discuss the applications of Green's functions in quantum mechanics. Here we only concern the static single-particle Schrödinger equation which can be written as:

$$\hat{H}\psi = E\psi; \quad \hat{H} = \frac{\hat{p}^2}{2m} + V = -\frac{\hbar^2}{2m}\nabla^2 + V, \quad (2.26)$$

or equivalently,

$$[E - \hat{H}]\psi = 0. \quad (2.27)$$

Where \hat{H} is the Hamiltonian operator, E denotes the discrete eigenvalue of the system. The wavefunction of the Hamiltonian with eigenvalue E_n can be expanded to a complete

set of orthonormal eigenfunctions $\phi_n(\mathbf{r})$, given by:

$$\left\{ \begin{array}{l} \hat{H}\psi_n(\mathbf{r}) = E_n\psi_n(\mathbf{r}) \\ \psi_n(\mathbf{r}) = \sum_i \phi_i(\mathbf{r}) \\ \int \phi_n^*(\mathbf{r})\phi_m(\mathbf{r})d\mathbf{r} = \delta_{nm} \\ \sum_n \phi_n^*(\mathbf{r})\phi_n(\mathbf{r}') = \delta(\mathbf{r}, \mathbf{r}') \end{array} \right. . \quad (2.28)$$

Now we can define the Green's function in real space representation for the Schrödinger equation as:

$$[E - \hat{H}]G(\mathbf{r}, \mathbf{r}'; E) = \delta(\mathbf{r}, \mathbf{r}'). \quad (2.29)$$

If $E \neq E_n$, the Green's function $G(\mathbf{r}, \mathbf{r}'; E)$ can be calculated by:

$$G(\mathbf{r}, \mathbf{r}'; E) = \frac{\delta(\mathbf{r}, \mathbf{r}')}{E - \hat{H}} = \sum_n \frac{\phi_n^*(\mathbf{r})\phi_n(\mathbf{r}')}{E - E_n}. \quad (2.30)$$

Whereas, at $E = E_n$, the Green's function is infinite and corresponds to the discrete eigenvalue of H . In order to define the Green's function here, the limiting procedure with a positive infinitesimal ϵ can be applied. With this method, the retarded Green's function ($G^-(\mathbf{r}, \mathbf{r}'; E)$) and advanced Green's function ($G^+(\mathbf{r}, \mathbf{r}'; E)$) are introduced as:

$$\begin{aligned} G^\mp(\mathbf{r}, \mathbf{r}'; E) &= \lim_{\epsilon \rightarrow 0^+} G(\mathbf{r}, \mathbf{r}'; E \pm i\epsilon) \\ &= \frac{\delta(\mathbf{r}, \mathbf{r}')}{E \pm i\epsilon - \hat{H}} = \sum_n \frac{\phi_n^*(\mathbf{r})\phi_n(\mathbf{r}')}{E \pm i\epsilon - E_n}, \end{aligned} \quad (2.31)$$

or equivalently,

$$\begin{aligned} \hat{G}^\mp(z) &= \frac{1}{z - \hat{H}} \sum_n |n\rangle \langle n| = \sum_n \frac{|n\rangle \langle n|}{z - E_n}, \\ (z - \hat{H})\hat{G}^\mp(z) &= I \end{aligned} \quad (2.32)$$

under Dirac notation. Here $z = E \pm i\epsilon$, $|n\rangle$ and $\langle n|$ are the states corresponding to ϕ_n and ϕ_n^* , respectively. It is interesting and meaningful to discuss the physical meaning of Green's functions defined here. We start with the trace of the imaginary part of retarded Green's function in real-space representation:

$$\begin{aligned}
2\text{Tr}[\text{Im}G^-(\mathbf{r}, \mathbf{r}', E)] &= \text{Tr}[\text{Im}G^-(\mathbf{r}, \mathbf{r}'; z) - \text{Im}G^+(\mathbf{r}, \mathbf{r}'; z)] \\
&= \text{Im} \lim_{\epsilon \rightarrow 0^+} \sum_n \left[\frac{1}{E - E_n + i\epsilon} - \frac{1}{E - E_n - i\epsilon} \right] \\
&= \text{Im} \lim_{\epsilon \rightarrow 0^+} \sum_n \left[\frac{-2i\epsilon}{(E - E_n)^2 + \epsilon^2} \right] \\
&= -2\pi \sum_n \delta(E - E_n) = -2\pi D(E).
\end{aligned} \tag{2.33}$$

In the following parts, we will omit the superscript and the position variable of retarded Green's function $G^-(\mathbf{r}, \mathbf{r}'; z)$, if not otherwise specified. Therefore, the relation between retarded Green's function and local density of states (LDOS) is:

$$D(E) = -\frac{1}{\pi} \text{Tr}[\text{Im}G(E)]. \tag{2.34}$$

This equation can be generalized to the surface state calculations in the following sections.

2.2.3 Green's functions for surface states

In the above sections, we have theoretically introduced the approach of analyzing the condensed-matter by *ab-initio* calculations. In practical simulations, to perform these calculations, we always have to apply the periodic boundary conditions and choose a unit cell, which in fact represents a 3D (2D for slab or one-dimensional for wire) infinite system. In condensed-matter field, the surface state is one of the most important topics, based on the fact that all materials in nature are finite. The surface state exists because the surface of a materials changes the atoms of the surface from bulk to vacuum, which

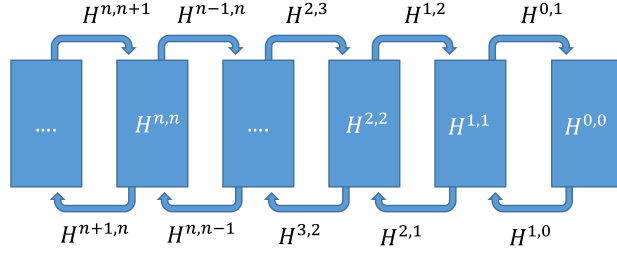


FIGURE 2.1: The schematic figure of a half-infinite surface. Each box represents a layer which consists of several unitcells. $H^{n-1,n}$, $H^{n,n-1}$ and $H^{n,n}$ are the matrix representation of the interactions between the layers of the superscripts, layer 0 is the terminal layer.

weakens the potential at the surface and produces new electronic states. In some systems, like the topological materials, the surface states have special characteristic and are always regarded as important evidence of topological structure.

The slab approach, which models a surface structure with several atomic layers, is the standard method for surface state calculations in first principle simulations. Whereas, in reality, a physical surface is a half-infinite system, interfacing with the vacuum. As a consequence, the electronic structure of surface atoms is altered by the quantum size effect if the slab is not thick enough. To overcome this drawback, the surface Green's function (SGF) has been proposed to calculate the surface states of the half-infinite system [25–29].

Within the nearest approximation, the matrix representation of Hamiltonian of the half-infinite surface is:

$$H = \begin{bmatrix} H^{0,0} & H^{0,1} & 0 & \dots & 0 & \dots \\ H^{1,0} & H^{1,1} & H^{1,2} & \dots & 0 & \dots \\ 0 & H^{2,1} & H^{2,2} & \ddots & 0 & \dots \\ \vdots & \vdots & \ddots & \ddots & H^{n-1,n} & \dots \\ 0 & 0 & 0 & H^{n,n-1} & H^{n,n} & \ddots \\ \vdots & \vdots & \vdots & \vdots & \ddots & \ddots \end{bmatrix}.$$

Where the superscripts represent the label of the layers as shown in Fig. 2.1, $H^{n-1,n}$, $H^{n,n-1}$ and $H^{n,n}$ are the matrix representation of the interactions between the labeled layers. By definition, $H^{0,0} = \epsilon^s$, $H^{i,i} = \epsilon_0$, $H^{0,1} = H^{n-1,n} = \alpha_0$, $H^{1,0} = H^{n,n-1} = \beta_0$. they can be calculated from the bulk Hamiltonian. Similarly, the Green's function can be written as:

$$G = \begin{bmatrix} G^{0,0} & G^{0,1} & G^{0,2} & \dots & G^{0,n} & \dots \\ G^{1,0} & G^{1,1} & G^{1,2} & \dots & G^{1,n} & \dots \\ G^{2,0} & G^{2,1} & G^{2,2} & \ddots & \vdots & \dots \\ \vdots & \vdots & \ddots & \ddots & G^{m-1,n} & \dots \\ G^{n,0} & G^{n,1} & \dots & G^{n,n-1} & G^{n,n} & \ddots \\ \vdots & \vdots & \vdots & \vdots & \ddots & \ddots \end{bmatrix}.$$

Based on the relation between the Green's function and LDOS as shown in Eqn. 2.34, to calculate the surface state, we only need to know the $G^{0,0}$ component. Using the first column of G which should satisfy the $(zI - H)G(E) = I$ equation, we have:

$$\begin{cases} (zI - H^{0,0})G^{0,0} - H^{0,1}G^{1,0} = I \\ -H^{n,n-1}G^{n-1,0} + (zI - H^{n,n})G^{n,0} - H^{n,n+1}G^{n+1,0} = 0 \end{cases}. \quad (2.35)$$

That is:

$$\begin{cases} (zI - \epsilon_0^s)G^{0,0} = I + \alpha_0 G^{1,0} \\ (zI - \epsilon_0)G^{n,0} = \beta_0 G^{n-1,0} + \alpha_0 G^{n+1,0}, \quad (n \geq 1) \end{cases}. \quad (2.36)$$

Then the Green's function components originated from the second nearest layers should satisfy:

$$\left\{ \begin{array}{l} (zI - \epsilon_1^s)G^{0,0} = I + \alpha_1 G^{2,0} \\ (zI - \epsilon_1)G^{n,0} = \beta_1 G^{n-2,0} + \alpha_1 G^{n+2,0}, \quad (n \geq 2) \\ \epsilon_1^s = \epsilon_0^s + \alpha_0 (zI - \epsilon_0)^{-1} \beta_0 \\ \epsilon_1 = \epsilon_0 + \alpha_0 (zI - \epsilon_0)^{-1} \beta_0 + \beta_0 (zI - \epsilon_0)^{-1} \alpha_0 \\ \alpha_1 = \alpha_0 (zI - \epsilon_0)^{-1} \alpha_0 \\ \beta_1 = \beta_0 (zI - \epsilon_0)^{-1} \beta_0. \end{array} \right. \quad (2.37)$$

Obviously, this process can be performed iteratively, after i th iteration, we can get:

$$\left\{ \begin{array}{l} (zI - \epsilon_i^s)G^{0,0} = I + \alpha_i G^{2^i,0} \\ (zI - \epsilon_i)G^{n,0} = \beta_i G^{n-2^i,0} + \alpha_i G^{n+2^i,0}, \quad (n \geq 2^i) \\ \epsilon_i^s = \epsilon_{i-1}^s + \alpha_{i-1} (zI - \epsilon_{i-1})^{-1} \beta_{i-1} \\ \epsilon_i = \epsilon_{i-1} + \alpha_{i-1} (zI - \epsilon_{i-1})^{-1} \beta_{i-1} + \beta_{i-1} (zI - \epsilon_{i-1})^{-1} \alpha_{i-1} \\ \alpha_i = \alpha_{i-1} (zI - \epsilon_{i-1})^{-1} \alpha_{i-1} \\ \beta_i = \beta_{i-1} (zI - \epsilon_{i-1})^{-1} \beta_{i-1}. \end{array} \right. \quad (2.38)$$

The parameters shown in Eqn. 2.38 can be calculated using the self-consistent approach. As they decay in the speed of square, one can expect that after limit numbers of iteration the α_i will converge to zero and the Green's function yields:

$$G^{0,0} = (zI - \epsilon_i^s)^{-1}.$$

Finally, surface states can be calculated using the Eqn. 2.34.

Chapter 3

Berry curvature

3.1 Basic concepts of Berry curvature

In the last section, we have introduced the method of calculating the ground states of bulk or half-infinite atomic system based on the stationary Schrödinger equation. Whereas, a real system is always in the excitation state and evolves with the changing of the environment, which makes it even more complicated. However, if the environment is slowly altered, which is equivalent to a stable H , the adiabatic theorem can be adapted in this situation. Adiabatic theorem tells us that at any instant a system will be in an eigenstate of the instantaneous H . If H goes back to its original form, the system will also return to its original state, except for a phase factor [30].

Let's consider a Hamiltonian $H(\mathbf{R})$ whose variables $\mathbf{R} = (R_1, R_2, R_3, \dots)$ are slowly changed in the parameter space, i.e.,

$$H = H(\mathbf{R}), \mathbf{R} = \mathbf{R}(t). \quad (3.1)$$

After $t = T$, the system traces along a closed path C and goes back to itself. In this process, the state $|\psi(t)\rangle$ of the system evolves according to the Schrödinger's equation,

$$H |\psi(t)\rangle = i\hbar \frac{\partial}{\partial t} |\psi(t)\rangle. \quad (3.2)$$

To construct the time-dependent wavefunction $|\psi(t)\rangle$, the instantaneous orthonormal basis $|n(\mathbf{R})\rangle$ from the eigenstates of $H(\mathbf{R})$ at each $\mathbf{R} = \mathbf{R}(t)$ are introduced. The basis satisfy:

$$H |n(\mathbf{R})\rangle = E_n(\mathbf{R}) |n(\mathbf{R})\rangle. \quad (3.3)$$

According to the adiabatic theorem, if the system is initially in one of the state $|n(\mathbf{R}(0))\rangle$, it will evolve with H and stay in the state of $|n(\mathbf{R}(t))\rangle$, apart from an additional phase,

$$|\psi(t)\rangle = \exp\left\{\frac{-i}{\hbar} \int_0^t dt' E_n(\mathbf{R}(t'))\right\} \exp(i\gamma_n(t)) |n(\mathbf{R}(t))\rangle, \quad (3.4)$$

where the first exponential is known as the dynamical phase factor. The $\gamma_n(t)$ in the second exponential is unrelated to the detailed path $\mathbf{R}(t)$ and is actually not single-valued, namely, $\gamma_n(T) \neq \gamma_n(0)$. Insert the time-dependent wavefunction into Eqn. 3.2, yielding,

$$\dot{\gamma}_n(t) |n(\mathbf{R}(t))\rangle = i |\dot{n}(\mathbf{R}(t))\rangle = i \nabla_{\mathbf{R}} |n(\mathbf{R}(t))\rangle \dot{\mathbf{R}}. \quad (3.5)$$

Multiply it from the left by $\langle \mathbf{R}(t) |$ and then integral it along the path C in parameter space, one obtains

$$\begin{aligned} \gamma_n(t) &= i \int_0^t \langle n(\mathbf{R}(t)) | \nabla_{\mathbf{R}} |n(\mathbf{R}(t))\rangle \dot{\mathbf{R}} dt \\ &= i \oint_C \langle n(\mathbf{R}) | \nabla_{\mathbf{R}} |n(\mathbf{R})\rangle d\mathbf{R} \\ &= \oint_C A_n(\mathbf{R}) d\mathbf{R}. \end{aligned} \quad (3.6)$$

Here, obviously, $A_n(\mathbf{R})$ is a vector function, which is single-valued at each position \mathbf{R} . It is called Berry connection or the Berry vector potential and can be easily proved to be gauge dependent[31]. But this is beyond the scope of this dissertation. Instead, we focus more on the curl of the Berry connection, which is actually more fundamental and is gauge invariant[31]. Since the path we choose is a closed loop, the Stokes's theorem here can be applied and the path integral can be transformed to a surface integral,

$$\gamma_n = \int \nabla_{\mathbf{R}} \times A_n(\mathbf{R}) d\mathbf{S}, \quad (3.7)$$

where \mathbf{S} is the surface expanded by the enclosed path. The integrand, namely the curl of the Berry connection, is defined as

$$\Omega_n(\mathbf{R}) = \nabla_{\mathbf{R}} \times A_n(\mathbf{R}). \quad (3.8)$$

It should be noticed that the Berry curvature intuitively resembles the magnetic field in parameter space, where the Berry connection is the analogue of vector potential that generates this magnetic field. As we will show later, the Berry curvature behaves like the virtual magnetic field in the reciprocal space, which is expanded by reciprocal vectors.

Direct evaluation of Berry curvature needs the differential of wavefunction $|n(\mathbf{R})\rangle$, and thus requires the wavefunction to be locally single-valued. This can be very complicated because the wavefunction is gauge dependent. To avoid this problem, we rewrite the Berry curvature in a linear-response form.

In order to derive the linear-response form of Berry curvature, we first apply the $\nabla_{\mathbf{R}}$ operation on both sides of Eqn. 3.3 and then left multiply them by $\langle m(\mathbf{R})|$. This yields

$$\langle m(\mathbf{R})| \nabla_{\mathbf{R}} |n(\mathbf{R})\rangle = \langle m(\mathbf{R})| \nabla_{\mathbf{R}} H |n(\mathbf{R})\rangle / (E_n - E_m), \quad m \neq n, \quad (3.9)$$

where E_m is the eigenvalue of $|m(\mathbf{R})\rangle$. Then we can insert the expression formula of $A_n(\mathbf{R})$ and the completeness condition $\sum_m |m\rangle \langle m| = I$ into Eqn. 3.8. With the abbreviated notation, we get,

$$\begin{aligned}
 \Omega_n(\mathbf{R}) &= i\nabla \times \langle n | \nabla | n \rangle = i\nabla \times \langle n | \nabla n \rangle \\
 &= i \langle \nabla n | \times | \nabla n \rangle = i \sum_{m \neq n} \langle \nabla n | m \rangle \times \langle m | \nabla n \rangle \\
 &= i \sum_{m \neq n} \frac{\langle n | \nabla H | m \rangle \times \langle m | \nabla H | n \rangle}{(E_n - E_m)^2}.
 \end{aligned} \tag{3.10}$$

It is clear that with this transformation, the differential on the wavefunction becomes the differential on the Hamiltonian, therefore it can be evaluated under any gauge choice. More specifically, if the parameters are in 3D real or reciprocal space and are expressed as $(\mathbf{R}_u, \mathbf{R}_v, \mathbf{R}_w)$, Eqn. 3.10 can be further simplified. In this parameter space, the ∇ operator on Hamiltonian can be simply written as $(\frac{\partial H}{\partial \mathbf{R}_u}, \frac{\partial H}{\partial \mathbf{R}_v}, \frac{\partial H}{\partial \mathbf{R}_w})$. Inserting it into Eqn. 3.10, we get the w component of Berry curvature

$$\Omega_{uv}^n(\mathbf{R}) = i \sum_{m \neq n} \frac{\langle n | \frac{\partial H}{\partial \mathbf{R}_u} | m \rangle \langle m | \frac{\partial H}{\partial \mathbf{R}_v} | n \rangle - (v \leftrightarrow u)}{(E_n - E_m)^2}, \tag{3.11}$$

where the $(v \leftrightarrow u)$ represents the complex conjugate of the first term in the numerator. Eqn. 3.11 is more practical and useful for the numerical calculations as we will show in the following parts.

3.2 Berry curvature correction to the semiclassical equations of motion

3.2.1 Bloch theorem in crystalline solids

In this section, we would like to introduce the influence of Berry curvature on electronic transports in crystalline solids. Because of the translation symmetry in crystalline solid, the eigenstate of each electrons can be written as a Bloch wave, which is also known as Bloch's theorem:

$$\psi_{n\mathbf{q}}(\mathbf{r}) = e^{i\mathbf{q}\cdot\mathbf{r}}u_{n\mathbf{q}}(\mathbf{r}), \quad (3.12)$$

where the \mathbf{r} is the position, $\psi(\mathbf{r})$ is the Bloch wave, \mathbf{q} is the crystal wave vector which is also known as the quantum number of the state, n is the band index, $u_{n\mathbf{q}}(\mathbf{r})$ is a periodic function with the same periodic as the crystal,

$$u_{n\mathbf{q}}(\mathbf{r}) = u_{n\mathbf{q}}(\mathbf{r} + \mathbf{G}). \quad (3.13)$$

Here \mathbf{G} is the unit vector of the crystal. Correspondingly, the Schrödinger equation in the basis of the periodic function can be obtained by inserting Eqn. 3.12 into Eqn. 2.26,

$$\begin{cases} H(\mathbf{q})u_{n\mathbf{q}}(\mathbf{r}) = E_{n\mathbf{q}}u_{n\mathbf{q}}(\mathbf{r}) \\ H(\mathbf{q}) = e^{-i\mathbf{q}\cdot\mathbf{r}}\left(\frac{\mathbf{P}^2}{2m} + V\right)e^{i\mathbf{q}\cdot\mathbf{r}} \end{cases} \quad (3.14)$$

On the one hand, with the commutation:

$$\begin{aligned} \left[\frac{\mathbf{P}^2}{2m}, e^{i\mathbf{q}\cdot\mathbf{r}}\right] &= \frac{\hbar\mathbf{q}\cdot\mathbf{P}}{m}e^{i\mathbf{q}\cdot\mathbf{r}} \\ &= e^{i\mathbf{q}\cdot\mathbf{r}}\frac{\hbar^2\mathbf{q}^2}{2m} + e^{i\mathbf{q}\cdot\mathbf{r}}\frac{2\hbar\mathbf{q}\cdot\mathbf{P}}{2m}. \end{aligned} \quad (3.15)$$

Then the Hamiltonian $H(\mathbf{q})$ can be transformed to

$$H(\mathbf{q}) = \frac{(\mathbf{p} + \hbar\mathbf{q})^2}{2m} + V. \quad (3.16)$$

On the other hand, with Eqn. 3.14 one can easily get $u_{n\mathbf{q}+\mathbf{K}} = e^{-i\mathbf{K}\cdot\mathbf{r}}u_{n\mathbf{q}}(\mathbf{r})$. Because of the periodic condition of $u_{n\mathbf{q}+\mathbf{K}}$, the wavefunction has to be a periodic function of \mathbf{q} ,

$$\psi_{n\mathbf{q}}(\mathbf{r}) = \psi_{n\mathbf{q}+\mathbf{K}}(\mathbf{r}), \quad e^{i\mathbf{K}\cdot\mathbf{G}} = 1. \quad (3.17)$$

If we define \mathbf{q} as the basis of a parameter space, the period of \mathbf{K} allows us to transfer the space from the extended zone scheme to the reduced zone scheme, which is actually the first Brillouin Zone (BZ).

3.2.2 Intrinsic electronic transports and Berry curvature correction

The dynamic of Bloch electrons in the electric field is one of the most fundamental problems in condensed-matter physics. In semiclassical theory, the electric field is regarded as a perturbation and does not appear in the electronic velocity,

$$\dot{\mathbf{r}} = \frac{\partial E_n(\mathbf{q})}{\hbar\mathbf{q}}. \quad (3.18)$$

However, this is true only if the external electric field is sufficiently weak. A better approach of understanding the influence of the electric field is to add the electric field in the Hamiltonian and then solve the Schrödinger equation. According to electrodynamics, the electric field can enter the Hamiltonian either through a time-independent electrostatic potential $\phi(r)$ or through a uniform time-dependent vector potential $\mathbf{A}(t)$. The former looks simple because time is not involved, but it will break the translation symmetry of crystal and makes the Bloch's theorem invalid. Therefore, the latter

method is used, using the Peierls substitution, the Hamiltonian is written as

$$H(t) = \frac{[\hat{\mathbf{p}} + e\mathbf{A}(t)]^2}{2m} + V(\mathbf{r}).$$

Following the same way as obtaining $H(\mathbf{q})$ from H , the \mathbf{q} -space representation of Hamiltonian can be calculated as

$$H(\mathbf{q}, t) = \frac{[\hat{\mathbf{p}} + e\mathbf{A}(t) + \hbar\mathbf{q}]^2}{2m} + V(\mathbf{r}). \quad (3.19)$$

As mentioned in the last section, if the electric field varies relatively slow and the adiabatic approximation is available, the wave function can be expanded in terms of the instantaneous normalized eigenfunctions $u_{n\mathbf{q}}(r, t)$. With the first-order approximation and the abbreviated notation, the wave function is given by[5, 32]:

$$|\tilde{u}_n\rangle = |u_n\rangle - i\hbar \sum_{m \neq n} \frac{|u_m\rangle \langle u_m | \partial u_n / \partial t \rangle}{E_n - E_m}. \quad (3.20)$$

In quantum mechanics, the velocity operator is simply the commutation of the position operator with the Hamiltonian. In \mathbf{q} -space representation, this yields

$$\begin{aligned} \hat{v}(\mathbf{q}) &= \dot{r} = \frac{i}{\hbar} [H(\mathbf{q}, t), r] \\ &= \frac{i}{\hbar} \left[\frac{[\hat{\mathbf{p}} + e\mathbf{A}(t) + \hbar\mathbf{q}]^2}{2m} + V(\mathbf{r}), r \right] \\ &= \frac{e\mathbf{A}(t) + \hbar\mathbf{q} + \hat{\mathbf{p}}}{m} = \frac{\partial H(\mathbf{q}, t)}{\partial(\hbar\mathbf{q})}. \end{aligned} \quad (3.21)$$

Therefore, the average velocity is

$$\begin{aligned}
v_n(\mathbf{q}) &= \langle \tilde{u}_n | \hat{v}(\mathbf{q}) | \tilde{u}_n \rangle \\
&\approx \langle u_n | \frac{\partial H(\mathbf{q}, t)}{\partial(\hbar\mathbf{q})} | u_n \rangle - i \left[\sum_{m \neq n} \frac{\langle u_n | \frac{\partial H(\mathbf{q}, t)}{\partial \mathbf{q}} | u_m \rangle \langle u_m | \frac{\partial u_n}{\partial t} \rangle}{E_n - E_m} - c.c. \right] \\
&= \frac{\partial E_n}{\hbar \partial \mathbf{q}} - i \left[\sum_{m \neq n} \frac{\langle u_n | \frac{\partial H(\mathbf{q}, t)}{\partial \mathbf{q}} | u_m \rangle \langle u_m | \frac{\partial H(\mathbf{q}, t)}{\partial t} | u_n \rangle}{(E_n - E_m)^2} - c.c. \right].
\end{aligned} \tag{3.22}$$

Here, *c.c.* means complex conjugate, and the second-order series are omitted. The first term of the velocity formula is the contribution of the band dispersion, similar to that in the semiclassical theory. Besides that, an additional term appears, which is the berry curvature $\mathbf{\Omega}_{\mathbf{q}t}$. In addition, according to Eqn. 3.19, we have

$$\frac{\partial H(\mathbf{q}, t)}{\partial t} = \frac{\partial H(\mathbf{q}, t)}{\partial(\hbar\mathbf{q})} \frac{\partial(e\mathbf{A}(t))}{\partial t} = -\frac{e}{\hbar} \frac{\partial H(\mathbf{q}, t)}{\partial \mathbf{q}} \cdot \mathbf{E}, \tag{3.23}$$

which indicate that $\mathbf{\Omega}_{\mathbf{q}t} = -\frac{e}{\hbar} \mathbf{\Omega}_{\mathbf{q}\mathbf{q}} \cdot \mathbf{E}$. It is important to note here that, although $\mathbf{\Omega}_{\mathbf{q}\mathbf{q}}$ has the form of second-order tensor, all the diagonal elements are 0 and only three independent elements exist. Therefore, the dot product can be simply transferred to the cross product of a vector and the electric field. Take the component $v_n^\alpha(\mathbf{q})$ as an example, we get

$$v_n^\alpha(\mathbf{q}) = \frac{\partial E_n}{\hbar \partial \mathbf{q}_\alpha} + \frac{e}{\hbar} (\Omega_{n,\alpha\beta}(\mathbf{q}) E_\beta - \Omega_{n,\gamma\alpha}(\mathbf{q}) E_\gamma), \tag{3.24}$$

where,

$$\Omega_{n,\alpha\beta}(\mathbf{q}) = 2i \sum_{m \neq n} \frac{\langle u_n | \frac{\partial H}{\partial q_\alpha} | u_m \rangle \langle u_m | \frac{\partial H}{\partial q_\beta} | u_n \rangle}{(E_n - E_m)^2}. \tag{3.25}$$

If we define the gauge-invariant crystal momentum $\mathbf{k} = \mathbf{q} + \frac{e}{\hbar} \mathbf{A}(t)$, the conclusion can be directly generalized to \mathbf{k} , considering that $\partial/\partial \mathbf{q} = \partial/\partial \mathbf{k}$. Finally, we get the Berry

curvature corrected motion equation of the electron:

$$v_n(\mathbf{k}) = \frac{\partial E_n(\mathbf{k})}{\hbar \partial \mathbf{k}} + \frac{e}{\hbar} \mathbf{E} \times \boldsymbol{\Omega}_n(\mathbf{k}). \quad (3.26)$$

It is clear that the second term is always transverse to the electric field, which leads to a Hall current. The Berry curvature language, which was originally proposed by Karplus and Luttinger in 1954 [33], provides a nice explanation of the anomalous Hall effect (AHE) in condensed matter.

3.2.3 Anomalous Hall effect and spin Hall effect

Now we discuss the intrinsic electric conductivity which originates from the electronic structure of the material. Considering the distribution function of all the electronic states, the current density is

$$\begin{aligned} \mathbf{J} &= \frac{1}{V} \sum_n \int (-e) v_n(\mathbf{k}) f_n(E) d\mathbf{k} = -\frac{1}{(2\pi)^d} \sum_n \int_{BZ} e v_n(\mathbf{k}) f_n(E) d\mathbf{k} \\ &= -\frac{1}{(2\pi)^d} \left[\frac{e}{\hbar} \sum_n \int_{\Omega} f_n(E) \frac{\partial E_n(\mathbf{k})}{\partial \mathbf{k}} d\mathbf{k} + \mathbf{E} \times \frac{e^2}{\hbar} \sum_n \int_{BZ} \boldsymbol{\Omega}_n(\mathbf{k}) f_n(E) d\mathbf{k} \right]. \end{aligned} \quad (3.27)$$

Here the $f_n(E)$ is the Fermi-Dirac distribution function of the n -th band, d is the dimension of the crystal, and BZ is the first Brillouin zone. Clearly, the first term originates from the group velocity of all the electrons under electric field and corresponds to the longitudinal electric conductivity. While the second term is the anomalous Hall conductivity (AHC) for 3D materials and is perpendicular to the external electric field. Using $\mathbf{J} = \sigma \mathbf{E}$ and rewriting the cross product into a dot product of the AHC tensor

and \mathbf{E} , each element of the AHC can be written as

$$\begin{aligned}\sigma_{\alpha\beta} &= -\frac{e^2}{\hbar} \sum_{m \neq n} \int_{BZ} \Omega_{n,\alpha\beta}(\mathbf{k}) \frac{d\mathbf{k}}{(2\pi)^3} \\ &= -2e^2 \hbar i \sum_{m \neq n} \int_{BZ} \left[\frac{\langle u_n | \hat{v}_\alpha | u_m \rangle \langle u_m | \hat{v}_\beta | u_n \rangle}{(E_n - E_m)^2} \right] \frac{d\mathbf{k}}{(2\pi)^3}.\end{aligned}\quad (3.28)$$

Here $\hat{v}_\alpha = \frac{\partial H}{\hbar \partial k_\alpha}$ is the α element of the velocity operator. The formula of AHC above can be understood in the way of linear response approach, which says the $\sigma_{\alpha\beta}$ is the response of electrons' charge current in α direction if the external field aligns in β direction. Similarly, we can derive the spin Hall conductivity (SHC), which is the response of electrons' spin current (angular momentum) along α direction when the external field is in β direction. Replacing the operator $-e\hat{v}_\alpha$ in Eqn. 3.28 by the spin current operator $\hat{J}_\alpha^\gamma = \frac{1}{2} \{ \frac{\partial H}{\hbar \partial k_\alpha}, \hat{s}_\gamma \} = \frac{1}{2} \{ \hat{v}_\alpha, \hat{s}_\gamma \}$, where \hat{s}_γ is the γ component of the spin operator, the SHC has the form of

$$\sigma_{\alpha\beta}^\gamma = 2e\hbar i \sum_{m \neq n} \int_{BZ} \left[\frac{\langle u_n | \hat{J}_\alpha^\gamma | u_m \rangle \langle u_m | \hat{v}_\beta | u_n \rangle}{(E_n - E_m)^2} \right] \frac{d\mathbf{k}}{(2\pi)^3}.\quad (3.29)$$

From the computational point of view, the AHC is a second-order tensor, while the SHC is a three-order tensor with three degrees of freedom: spin, electron's movement and the electric field. Although the integrant in Eqn. 3.29 has a similar format, it is actually not the Berry curvature. In order to distinguish them, the former is referred as the spin Berry curvature ($\Omega_n^s(\mathbf{k})$) in this thesis.

3.3 Symmetry analysis of Berry curvature

As the Berry curvature and spin Berry curvature are directly originated from the band structure, they are fully compatible with the symmetry of the Hamiltonian. Therefore, the symmetrical analysis can help us understand the properties of the (spin) Berry

curvature and the shape of AHC (SHC). In this section, we mainly focus on time-reversal, inversion and mirror-reflection symmetries because they play important roles in topological materials.

The analysis of Berry curvature could be performed from either the velocity formula as shown in Eqn. 3.26, or the linear response format of Berry curvature as shown in Eqn. 3.25. For the first method, since the symmetry of \mathbf{k} , $v_n(\mathbf{k})$ and \mathbf{E} were already known, we can derive the symmetry of Berry curvature from them.

If the system has time-reversal symmetry \hat{T} , \mathbf{E} maintains its sign under \hat{T} operation, and $\mathbf{k} = -\mathbf{k}$, $v_n(\mathbf{k}) = -v_n(-\mathbf{k})$, $E_n(\mathbf{k}) = E_n(-\mathbf{k})$. Then we get

$$\Omega_n(\mathbf{k}) = -\Omega_n(-\mathbf{k}). \quad (3.30)$$

If the system has inversion symmetry \hat{P} , \mathbf{E} also changes its sign under \hat{P} operation. Thus we have

$$\Omega_n(\mathbf{k}) = \Omega_n(-\mathbf{k}). \quad (3.31)$$

The mirror-reflection symmetry \hat{m} is quite special because it has a different effect on different components of a vector. For \mathbf{k} , \mathbf{E} and $v_n(\mathbf{k})$, the \hat{m} will change the signs of the components perpendicular to the mirror and maintain the signs of the components parallel with it. As a consequence, the Berry curvature components which perpendicular to the mirror will maintain its sign, and the component which parallels with the mirror will change its sign. The effect of these three symmetries on Berry curvature are collected and shown in Fig. 3.1. As we can see here, apart from the similar effect as the magnetic field, the Berry curvature is also a pseudovector and has the same symmetry as the magnetic field.

To analysis the symmetry of the spin Berry curvature, we should start from the Eqn. 3.25, which is actually more general. For a system preserving time-reversal symmetry \hat{T} , we

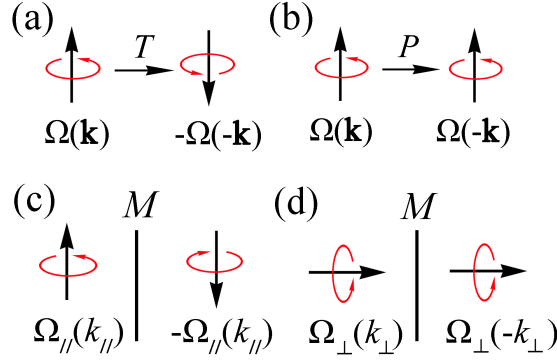


FIGURE 3.1: Berry curvature under time-reversal, inversion and mirror symmetries. The red and black arrows indicate Berry connection and Berry curvature, respectively.

have

$$\begin{aligned} \langle u_n | \hat{v} | u_m \rangle &= \langle u_n | \hat{T}^{-1} \hat{v} \hat{T} | u_m \rangle = \langle \hat{K} u_n | \hat{v} | \hat{K} u_m \rangle = -\langle u_n | \hat{v} | u_m \rangle^*, \\ \langle u_n | \{ \hat{v}, \hat{s} \} | u_m \rangle &= \langle u_n | (\hat{K} \sigma_y)^{-1} \{ \hat{v}, \hat{s} \} \hat{K} \sigma_y | u_m \rangle = \langle u_n | \{ \hat{v}, \hat{s} \} | u_m \rangle^*, \end{aligned} \quad (3.32)$$

where \hat{K} is the complex conjugation. As shown here, $\Omega_n(\mathbf{k})$ is odd while $\Omega_n^s(\mathbf{k})$ is even under \hat{T} operation. Since the intrinsic AHC is the integration of $\Omega_n(\mathbf{k})$ in the whole BZ, it should be zero because $\Omega_n(\mathbf{k})$ and $\Omega_n(-\mathbf{k})$ will cancel with each other if the system has time-reversal symmetry. On the other hand, if the system has inversion symmetry, which states

$$\begin{aligned} \langle u_n | \hat{v} | u_m \rangle &= \langle u_n | \hat{P}^{-1} \hat{v} \hat{P} | u_m \rangle = \langle u_n | \hat{v} | u_m \rangle, \\ \langle u_n | \{ \hat{v}, \hat{s} \} | u_m \rangle &= \langle u_n | \hat{P}^{-1} \{ \hat{v}, \hat{s} \} \hat{P} | u_m \rangle = \langle u_n | \{ \hat{v}, \hat{s} \} | u_m \rangle, \end{aligned} \quad (3.33)$$

both $\Omega_n(\mathbf{k})$ and $\Omega_n^s(\mathbf{k})$ is even respect to \mathbf{k} . Therefore, the system is able to have non-zero AHC and SHC.

Chapter 4

Quasiparticles in condensed materials

4.1 Weyl fermions

4.1.1 Introduction

As is known to us, the Schrödinger equation is one of the most important equations in condensed matter physics. It is used to describe the states of non-relativistic electrons and atoms in the microscopic system. On the other hand, in particle physics, where the relativistic effects can not be neglected, this equation is not appropriate anymore. Instead, we use the equation which is proposed by Dirac in 1928 [34] and has the covariant form of

$$(i\gamma^u \partial_u - m)\psi = 0. \quad (4.1)$$

Here m and ψ are the mass and the wave function of the particle, respectively. γ^u represents four 4×4 Gamma matrices and satisfies the Dirac algebra:

$$\{\gamma^u, \gamma^v\} = \gamma^u \gamma^v + \gamma^v \gamma^u = 2\eta^{uv} I, \quad (4.2)$$

where η^{uv} is the component of the Minkowski metric and equals to δ_{uv} when $u = 0$ and $-\delta_{uv}$ when $u = (1, 2, 3)$. I is the 4×4 identity matrix. There are different ways of choosing Gamma matrices. In Weyl representation, they can be represented using 2×2 identity and Pauli matrices:

$$\gamma^0 = \begin{bmatrix} 0 & I \\ I & 0 \end{bmatrix}, \quad \gamma^i = \begin{bmatrix} 0 & \sigma^i \\ -\sigma^i & 0 \end{bmatrix}.$$

Therefore, the Dirac equation actually consists of four coupled partial differential equations and is not easy to calculate. When Dirac first wrote his paper, no doubt he had the electron in mind, because he entitled his article “The Quantum Theory of the Electron”. And we know, the electron has mass and charge. Shortly after Dirac’s paper was published in 1928, Weyl noticed that for massless fermions $m = 0$, the Dirac equation can be simplified as [35]

$$\gamma^u \partial_u \psi = 0 \tag{4.3}$$

or

$$\begin{pmatrix} 0 & i\hbar\partial_t - \mathbf{p} \cdot \boldsymbol{\sigma} \\ i\hbar\partial_t - \mathbf{p} \cdot \boldsymbol{\sigma} & 0 \end{pmatrix} \begin{pmatrix} \psi_A \\ \psi_B \end{pmatrix} = 0$$

without any field. The equation is decoupled and effectively equal to two Weyl equations which can be written in Schrödinger form:

$$\mathcal{H}^\pm \psi = i\hbar \frac{\partial}{\partial t} \psi, \quad \mathcal{H}^\pm = \pm \hbar \mathbf{k} \cdot \boldsymbol{\sigma}. \tag{4.4}$$

The particles which satisfy the Weyl equations are called Weyl fermions. In Fig.4.1 We have shown the energy dispersion and the spin polarization of the free Weyl fermions. From it one can easily get the conclusion:

- 1) The Energy dispersion over wave vector (\mathbf{k}) is linear in every direction, the spin

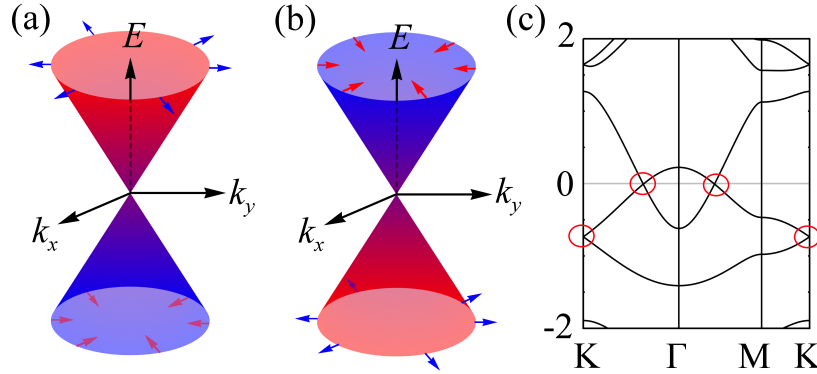


FIGURE 4.1: Energy dispersions of Weyl equations with the positive sign (a) and negative sign (b) in $k_x - k_y$ plane. The red and blue arrows indicate the direction of the spin directions. (c) The band structure of Hg_3As_2 [36]

and momentum of the particle are locked together and tend to align in parallel or anti-parallel.

2) Since the Hamiltonian has two branches, both of them should be satisfied, indicating that the Weyl fermions should exist in pairs. Actually, the signs in front of the Hamiltonian correspond to two different possible chirality.

For a long time, the neutrino was regarded as a type of Weyl fermions. However, it was found later that neutrino has a very tiny mass. Although the mass can always be neglected, it is not exactly Weyl fermion. Actually, until now we still couldn't find Weyl fermions in nature. But it is interesting that in some solid materials, this kind of Hamiltonian can be found somewhere in the reciprocal space, as shown in the red circle enclosed parts in Fig4.1c. In this case, these materials can be ideal platforms for studying Weyl fermions.

The idea of finding Weyl fermions in solid materials was first proposed by Xiangang Wan's group in 2011 [17]. They theoretically investigated pyrochlore iridates (like $\text{Y}_2\text{Ir}_2\text{O}_7$) and showed the existence of novel phases because of electron correlations and strong spin-orbit interactions. These novel phases give rise to interesting surface states

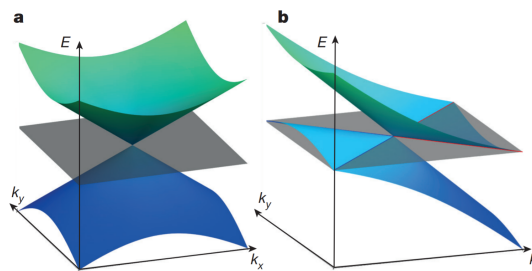


FIGURE 4.2: Energy dispersions of two types of Weyl points. (a) Type-I Weyl point with point-like Fermi surface. (b) Type-II Weyl point with hourglass shape Fermi surface. These grey planes correspond to the Fermi level. The figures are obtained from [43]

which are discontinuous in momentum space and connect to the so called Weyl points. The Weyl point is, to some extent, a type of Weyl fermions since it satisfies the Weyl equations. Wan’s group named these surface states “Fermi arcs” and materials which host Weyl points “Weyl semimetals” (WSMs). After that, more materials like TaAs, TaP, NbAs, NbP [37] are reported to be Weyl semimetals and then experimentally discovered [38–42].

The Weyl points were originally thought to exhibit point-like Fermi surfaces in all directions, as observed in the aforementioned materials. In 2015, Alexey et al. proposed another type of Weyl points around which the band dispersion is strongly tilted along certain directions. In order to distinguish, they named the new type of Weyl points as Type-II Weyl points and the original ones as type-I Weyl points. Because of the difference in band dispersion, a novel Fermi surface, in which the electron and hole pockets are connected at a single point (the Weyl points), can be observed in type-II WSMs as shown in Fig 4.2 (b) [43]. Alexey et al. suggested that the WTe_2 can be a host of type-II Weyl points. Shortly after that, MoTe_2 , the analogue of WTe_2 , attracted more interests and was experimentally verified [44–48]. Topologically, the type-I and type-II Weyl points are quite similar, both have ± 1 topological charges and Fermi arcs. However, since the Fermi surfaces of type-II WSMs are anisotropic, their physical properties can be strong anisotropic and different from those of type-I WSMs.

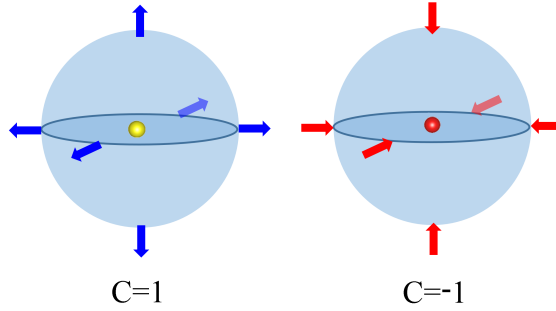


FIGURE 4.3: Topological charges of Weyl points. The arrows indicate the direction of Berry curvature. The yellow and red balls represent the positive and negative Weyl points respectively.

4.1.2 Topological charge

It is known that for a gapped topological system, like the Chern insulator, Z_2 topological insulator or topological crystalline insulator, an invariant can be defined using Berry phase or Berry curvature in momentum space [49]. Interestingly, though the Weyl semimetal/metal is a gapless system, a similar topological number can be defined. As the Weyl point has linear dispersion along all the directions, we can always find a closed 2D surface which encloses the Weyl point but is gapped everywhere in the momentum space as shown in Fig.4.3. By integrating the Berry curvature flux of occupied bands on the surface, we will always get either 1 or -1, corresponding to the case of Berry curvature pointing toward to or back to the Weyl point, respectively.

Actually, the sign of the topological number is determined by the sign of the Hamiltonian in Weyl equation 4.4 and indicates the chirality of Weyl point. It is analogous to the “electronic charge” and can be viewed as the charge of Weyl point in momentum space, where the Berry curvature plays the role of “electric field”. Therefore, the Weyl point is either the drain or the source of Berry curvature and can be viewed as a “magnetic monopole” in momentum space [17, 50, 51], as shown in Fig.4.4. On the one hand, the topological charge requires that the Weyl points should exist in pairs to maintain the total charge of the system to be zero. On the other hand, because of the topological charge and chirality, the only way to annihilate Weyl points is to move the opposite

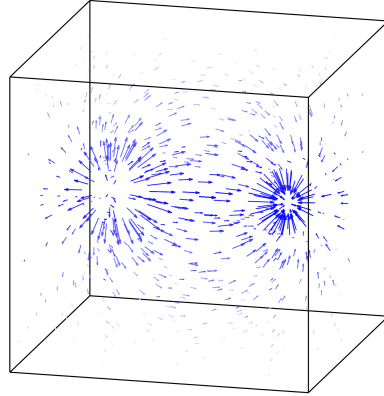


FIGURE 4.4: Berry curvature distribution near two opposite Weyl points. The Weyl point behaviors like a “magnetic monopole” and the Berry curvature plays the role of magnetic field.

Weyl points to the same point in BZ. Since this Weyls can sit far away from each other in the BZ, the annihilation requires large changes of Hamiltonian parameters, and thus WSMs are stable.

4.1.3 Symmetry of Weyl fermions

In condensed-matter, if both time reversal T and spatial inversion symmetry P exist, the spin up and spin down states will degenerate at every point in reciprocal space. Under time reversal symmetry, both the wave vector and spin change their signs, the eigenvalue satisfies:

$$E(\mathbf{k}, \uparrow) = E(-\mathbf{k}, \downarrow).$$

While for spatial inversion symmetry, only the wave vector changes its sign:

$$E(\mathbf{k}, \uparrow) = E(-\mathbf{k}, \uparrow); \quad E(\mathbf{k}, \downarrow) = E(-\mathbf{k}, \downarrow).$$

Combining together, we have:

$$E(\mathbf{k}, \uparrow) = E(\mathbf{k}, \downarrow).$$

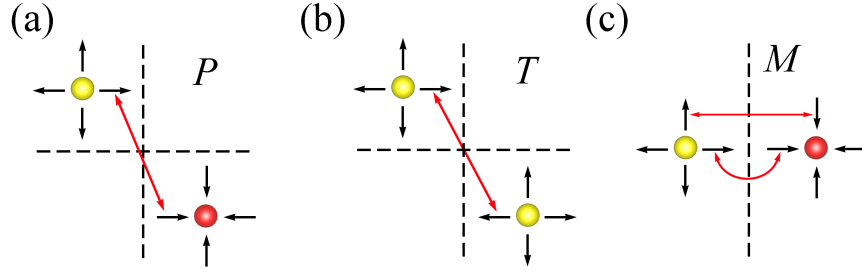


FIGURE 4.5: Weyl fermions under inversion (a), time-reversal (b) and mirror-reflection symmetries (c). The yellow and red balls represent the positive and negative Weyl points, respectively. The black arrows indicate the direction of Berry curvature. Inversion and mirror reflection symmetry change the chirality of Weyl points, but time-reversal symmetry doesn't change the chirality.

The degeneracy of spin up and spin down introduces another topological state: Dirac semimetal/metal, in which the linear dispersion relation around a gapless point also holds, but each gapless point is four-fold degenerate in 3D momentum space. Therefore, to obtain Weyl fermion, either the time reversal T or spatial inversion symmetry P should be broken.

Generally speaking, there is no symmetrical requirement for the formation of Weyl points. But the symmetry analysis is still quite necessary and helpful in understanding the chirality and distribution of Weyl points in reciprocal space. Fig.4.5 shows the chirality of Weyl points under time-reversal, inversion and mirror-reflection symmetry. Since the Berry curvature is a pseudovector, similar with spin and magnetic field, it will change direction under time-reversal symmetry and keep the same under inversion symmetry, as indicated by the red and black arrows in Fig.4.5(a) and (b). While under mirror reflection symmetry, the signs of Berry curvature components parallel with the mirror plane will change and the components perpendicular to the mirror plane will maintain, as shown in Fig.4.5(c).

Following these rules, one can easily find that the chirality of two Weyl points should be opposite if they are connected by inversion symmetry and should be identical if they are connected by time-reversal symmetry. As the Weyl points with opposite chirality should

exist in pairs, the total number of Weyl points should be the multiple of 2. Moreover, for a system without inversion symmetry, if time reversal symmetry exist, the total number of Weyl points should be the multiple of 4. This is obvious because there must be two negative Weyl points somewhere in the reciprocal space if we have two positive ones related by the time-reversal symmetry.

4.1.4 Fermi arcs

The existence of Fermi arcs on the surface is another significant consequence of Weyl points inside the 3D bulk materials. For the topologically trivial phase, once a surface is cut, closed (or extended to infinite) surface states appear because of dangling bonds and the dramatic potential changing of terminal atoms. However, for a WSM, besides these trivial states, some unclosed surface states, which are called Fermi arcs, connecting the surface projection of opposite Weyl points can be found on the surface as shown in Fig.4.6(c). It can be understood in the following way:

For a WSM, we can consider a small cylinder enclosing a Weyl point which locates at $\mathbf{k}_0 = (k_x^0, k_y^0, k_z^0)$ in the 3D reciprocal space. To simplified the analysis, the longitudinal axis of the cylinder is set to along k_z direction. In this case, the cylinder can be defined by two periodic parameters: $(\mathbf{k}_\lambda, k_z)$, where $\mathbf{k}_\lambda = [k_x^0 + k_R * \cos(\theta), k_y^0 + k_R * \sin(\theta)]$ is the radial wave vector with a period of 2π in k_x, k_y plane as shown in Fig.4.6(a). The Chern number of this 2D band structure of the cylinder is given by the Berry curvature integration through all the cylinder plane:

$$C = \frac{1}{2\pi} \int_S \Omega dk_z d\mathbf{k}_\lambda.$$

According to the Stokes' theorem, this integration equals to the total “topological charge” carried by the Weyl points enclosed inside. Therefore, this 2D subsystem is a quantum Hall insulator with Chern number equals to 1 (or -1) if only one Weyl point

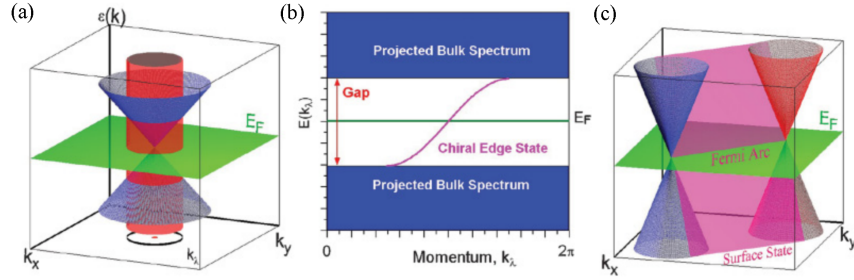


FIGURE 4.6: Origin of Fermi arcs in the WSM. (a) The bulk band dispersion of a two-bands model which hosts a Weyl point. A cylinder defined by (\mathbf{k}_\perp, k_z) and enclosing the Weyl point is also drawn. (b) The projected band dispersion along \mathbf{k}_\perp when a surface perpendicular to k_z direction is cut. A chiral edge state appears due to the nonzero Chern number of the cylinder. The chiral edge state intersects with the Fermi level at a crossing point. (c) The Fermi arc appears by connecting the crossing points of different cylinder radius. The arc terminates at another opposite Weyl. Figures are obtained from [17].

is enclosed. Once a surface perpendicular to k_z direction is cut, the cylinder will be projected to a circle surrounding the projection of the Weyl point, and a chiral edge state will appear as shown in Fig4.6(b). This chiral state intersects with the Fermi energy at a point. Then by varying the radius (k_R) of this cylinder, a list of points will be obtained until the opposite Weyl fermion is enclosed, which results in the cancellation of the Chern number and the disappearance of the chiral edge state. Connecting all these points, an arc beginning on a Weyl point of one chirality and terminating on a Weyl point of the opposite chirality will appear as shown in Fig4.6(c)[17, 50, 52]. Since no specific direction is needed during the deduction, the conclusion can be generalized to all the crystal surfaces. The topological Fermi arcs have been experimentally observed by ARPES in the TaAs, TaP, NbAs and NbP family [38–42].

4.2 Dirac fermions

4.2.1 Dirac fermions in three-dimensional materials

As mentioned in the last section, in 3D materials, the presence of both inversion and time reversal symmetries excludes the possibility of a two-fold degenerate Weyl node. Because the topological charge of Weyl fermions is even under time-reversal and odd under inversion symmetry, requiring the existence of two opposite but energetically degenerate Weyls at the same crystal momentum. Once two opposite Weyls meet in momentum space, their topological charge will cancel with each other and a gap can be opened by any perturbation, like the SOC, impurity and temperature fluctuation.

Nevertheless, these two compensating Weyl fermions can be stabilized by additional crystallographic space group symmetries [15, 53, 54], this produces a composite point singularity hosting a fourfold degeneracy which is called Dirac point. The Dirac points are direct analogues of Dirac electrons in high-energy theories and can be described by the Dirac equation when they locate close to the Fermi level. The materials that host Dirac points are called Dirac semimetals/Metals (DSMs). DSMs are of fundamental interest because they can be driven into various topologically distinct phase by simply breaking certain symmetries, and thus are perfect platforms for studying the topological phase transition. Besides that, although the topological charge of a Dirac point is zero, the DSM phase is topologically nontrivial in the sense that it can also have exotic surface states on the surfaces [14, 15, 55–58].

The existence of 3D DSMs was predicted, based on the first-principles calculations and effective model analysis, in β -cristobalite BiO_2 [54] and A_3Bi ($\text{A}=\text{Na},\text{K},\text{Rb}$) systems [15] in the year 2012. Afterwards, the electronic structures of Na_3Bi [14, 55, 59] and Cd_3As_2 [56, 60–62] are measured by angular-resolve photoemission spectroscopy (ARPES), and Dirac points with linear dispersions along all momentum directions are observed.

Generally, the DSM can be classified into two classes according to the position and numbers of Dirac points [63, 64]. Dirac points in the DSM of the first class are created via band inversion or accidental band crossings. These Dirac points locate away from the time-reversal invariant momentum (TRIM) points of the high order rotation axes (C_3 , C_4 , C_6) and the total number should be even. While for the second class DSM, it has an odd number of Dirac points at the TRIM points of the rotation axes where the band crossings are ensured by the lattice symmetry. Moreover, DSMs of these two classes are topologically different. For the first one, we can always find a non-zero topological invariant in either the $k_z=0$ or $k_z=\pi$ plane, where k_z direction is the direction of the high order axis. This will introduce 2D surface Dirac cones when a surface is cut parallel to the k_z axis. Therefore the first type of DSM is also called topological DSM. While for the second one, the system does not have this topological invariant and thus could not find the 2D surface Dirac cones.

Both the Na_3Bi and Cd_3As_2 , which are protected by C_6 and C_4 symmetries, respectively, belong to the first class DSM. And the β -cristobalite BiO_2 , which has three symmetry-related Dirac points located at TRIM X points [$\mathbf{k}=(0.5, 0, 0)$], belongs to the second class. It is important to note that, though topologically different, in both cases, the 3D DSM phases are stable and exhibit many exotic transport properties, such as large magnetoresistance (MR) [65, 66], negative MR [67, 68], high mobility [65, 69], and chiral anomaly [70, 71]. In addition, for the topological DSM, an additional quantum anomaly effect [72] exists because of the non-zero topological invariant.

In addition, similar with the type-II Weyl point, the Dirac point may also tilt strongly in energy-momentum space, as predicted in MA_3 ($M=\text{V}, \text{Nb}, \text{Ta}$; $A=\text{Al}, \text{Ga}, \text{In}$) [73] and PtSe_2 [74]. This type of Dirac point is named as type-II Dirac point. Shortly after the prediction, the APRES experiments that successfully observed the tilted energy dispersion and conic surface states in PtSe_2 were reported [75, 76]. The type-II Dirac semimetal phase is interesting not only because each type-II Dirac can be split into four type-II Weyl nodes via symmetry breaking, but also because it is Lorentz-violating and

has Landau level spectrum which is distinct from the type-I Dirac or Weyl semimetal. Thus different transport properties can be expected in this type of DSM.

4.2.2 Surface states of Dirac semimetals

It seems somewhat natural to observe Fermi arcs in DSMs, i.e. the “double Fermi arcs”, in the sense that a Dirac point can be understood as two opposite but energetically degenerate Weyls, each of them gives rise to a Fermi arc, as shown in Fig. 4.7. However, in contrast with the Fermi arcs in WSMs, in which the surface states are topologically protected and robust because of the non-zero topological charges of Weyls, the Dirac points in DSMs have zero topological charges. Thus a key question is whether the double Fermi arcs on the DSMs surface robust and topologically protected?

Several works have been focused on this issue [57, 58, 63]. It was claimed by Yang [63] that, the number of Fermi arcs on the surface of the DSM is determined by the 2D topological invariant on the $k_z = 0$ plane irrespective of the energy dispersion around the 3D Dirac points. Shortly after that, Potter [58] showed that, the Fermi arcs of DSMs are perturbatively stable to the symmetry-broken potential of the surface, which is the case for Na_3Bi and Ca_3As_2 , unless the surface potential is sufficiently strong [58]. While Kargarian [57] gave a different answer, based on a simple four-bands model calculation and rigorous K-theory analysis, he verified that the double Fermi arcs are not topologically protected and can be continuously deformed into a closed Fermi contour without any symmetry breaking or bulk phase transition.

Shown in Fig. 4.7 are the (100) surface states of a model of topological DSM, which has two Dirac points along k_z direction. Without any perturbation, the double Fermi arcs extending from one Dirac node to the other can be observed as shown in Fig. 4.7(b). But once a perturbation is added, even if it maintains the symmetry of the DSM, the double Fermi arcs are destroyed as shown in Fig. 4.7 (c-f). Whereas, for the topological DSM, the topological invariant at $k_z=0$ is non-zero, making the $k_z=0$ plane a 2D topological insulator and producing a chiral edge state at $k_z=0$ when (100) surface is

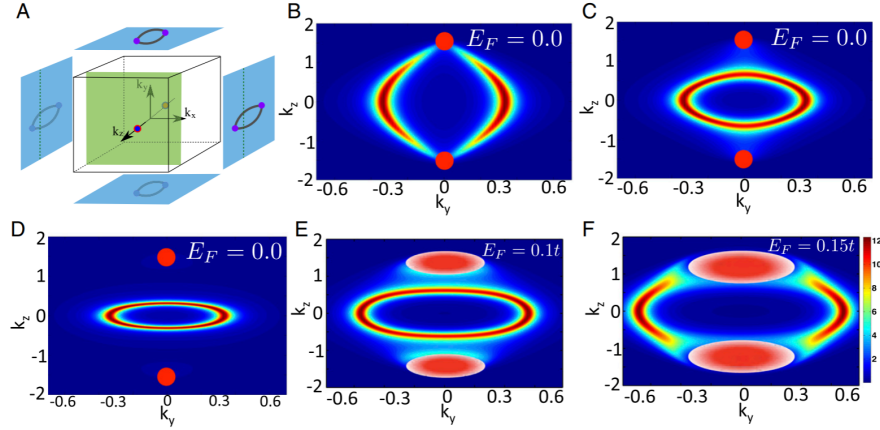


FIGURE 4.7: Surface states on the surface of topological DSM which originates from band inversion or accidental band crossings. (a) Schematic k -space picture of a DSM which has two Dirac points on the k_z axis. Shown as the light blue squares are the surface BZ, which host projected bulk Dirac points and double Fermi arcs. The green square is a 2D BZ slice perpendicular to k_z . (b) Double Fermi arcs of the DSM (100) surface without perturbation (c,d) Continuous deformation of double Fermi arcs under a symmetry-allowed mass term. The double Fermi arcs are deformed but not removed. The surface states at $k_z=0$ correspond to the chiral edge states because of the non-zero topological invariant and are not removable as shown in all the panels. (e,f) The electron-doped surface state with the same strength of perturbation as (d). The red dots are the projected bulk Dirac points, and the red blobs in (e) and (f) are the projection of bulk state. Adapted from Kargarian et. al. [57]

cut. Therefore, the surface states of topological DSM won't disappear, but continuously evolve in reciprocal space.

4.3 Triple point fermions

In previous sections, we have discussed two types of quasiparticles which are analogous of elementary particles of the quantum field theory: Weyl and Dirac Fermions. While in condensed-matter systems, where the quasiparticles are less constrained by Poincaré symmetry, more types of exotic fermionic excitations can be expected [53, 77–81]. In this section, we will focus on a new type of quasiparticle in condensed matter, which has

a three-fold degenerate band crossing in k -space and has no analogue to the standard model in particle physics [82].

4.3.1 Triple point fermions in three-dimensional materials

In a recent work, Bradlyn et al. [77] have reported several new types of free fermionic excitations in condensed-matter, which can be classified according to their degeneracies at and along high-symmetry points, lines and surfaces. These new fermions are stabilized by non-symmorphic space group symmetries and include three-, six-, or eight-fold degenerate band crossings. Among them, the three-fold degenerate band crossing, which is generally named as triple point fermion (TPF), has attracted much attention [77, 79, 81, 83–86]. The TPF is of fundamental interest, not only because it can be viewed as a fermionic spin-1 generalization of an ordinary Weyl fermion, but also because it lies between Dirac and Weyl fermions. The former property could give rise to some novel phenomena, and the latter makes the TPF an ideal intermediate species to study the phase transition between Dirac and Weyl fermions.

Bradlyn et al. verified, via symmetry analysis and *ab-initio* calculations, that the materials from space group 199, 214 and 220 can host TPFs and proposed three candidates of TPF metals/semimetals (TPFMs): $\text{Pd}_3\text{Bi}_2\text{S}_2$, $\text{Ag}_3\text{Se}_2\text{Au}$ and Ba_4Bi_3 . Nearly the same time Zhu et al. [84] reported the existence of TPFs in trigonal or hexagonal system, which are protected by symmorphic symmetry. A bunch of materials are predicted to be TPFMs, and are generally classified into two types according to the winding numbers of the nodal lines connecting the TPFs: The ones whose winding numbers are zero, like ZrTe family of compounds, and the ones which have non-zero winding numbers, like the CuPt-ordered $\text{InAs}_{0.5}\text{Sb}_{0.5}$ and strained HgTe. These were later theoretically confirmed by Chang et al. [79] and directly observed in MoP by Lv et al. using photoemission and ARPES measurements [80]. Moreover, Lv et al. also observed pairs of Weyl points in the bulk electronic structure that coexist with the TPFs. This is reasonable since both WSMs and TPTMs require that either the time-reversal or inversion symmetry

should be broken, thus making the TPFM an ideal platform for studying the interplay of different types of fermions.

As we will show later, in spite of different types, the TPFs are also topologically protected and can be characterized by the topological invariant. The TPFs are quite similar with Weyl points in WSMs, apart from that they are conceptually spin-1 quasiparticles. Some properties of the WSM can be generalized directly to the TPFM, like the chiral anomaly, Fermi arcs, high mobility and so on [79–81, 84, 85]. Whereas, further investigations are still required, such as the experimental observation of surface states and other novel properties in TPTMs.

4.3.2 Topological invariants and surface states

To explicitly reveal the topological invariants in TPFs we should first classify the TPFs according to the degeneracy of the bands near them. For the first class, which we named as TPF1 here, the bands are singly degenerate along all the directions away from the TPF as shown in Fig. 4.8 (b). This reminds us the definition of the topological charge of a Weyl point, in which a closed 2D manifold which is gaped everywhere is selected to enclose the Weyl point. By integrating the Berry curvature flux crossing the 2D manifold, an integer which respects to the topological charge of the particle will be obtained.

This approach can be generalized to TPF1. The only difference is that a TPF1 consists of three bands rather than two for a Weyl. It was shown that only two of these three bands are nontrivial and contribute Berry flux of $+2$ and -2 , respectively [77]. The third trivial band, which lies between the two non-trivial bands, has zero Berry flux. This allows the dispersion of the three bands near the degeneracy point to be linear as shown in Fig 4.8 (b). In this case, the TPF1 is a monopole with the topological charge of 2 and acts as a drain or source of Berry curvature in reciprocal space, similar to that of Weyl. Due to the topological charge of 2, each TPF of a TPFM will give rise to two

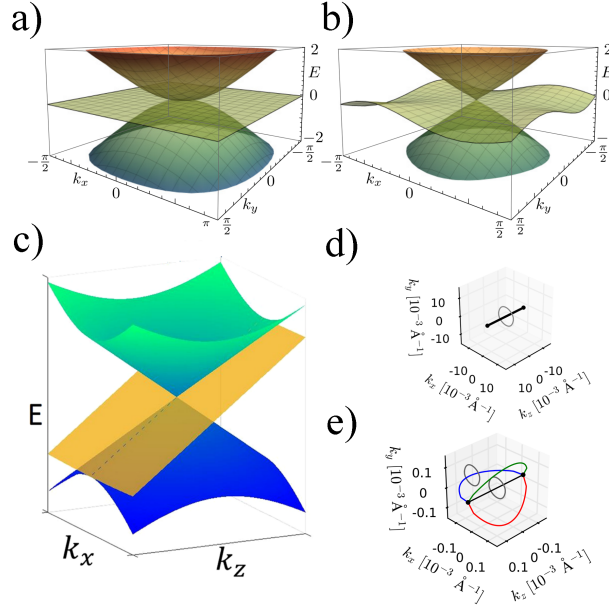


FIGURE 4.8: Energy dispersions and topological charges of TPFs. (a) Quadratic energy dispersion of double-Weyl node (b) Triple point whose bands are non-degenerate away from the gapless point. The upmost and lowest bands are non-trivial bands and are separated by the trivial band in between. (c) Triple points connected by nodal lines along high symmetry lines (d) or in high symmetry surfaces (e). The topological charges for (a) and (b) are ± 2 , while for (c) the similar topological invariant couldn't be defined. The topological invariant of (c) can be defined by winding number, which is 0 for (d) and ± 1 for (e). The figures are adapted from [78, 79, 84].

fermi arcs. This is distinguished from the Dirac point where the double Fermi arcs are not topologically protected.

Interestingly, apart from the TPF1 as mentioned before, there is another type of monopole quasiparticle which has topological charge of 2. It is called double-Weyl node (DWN) as shown in Fig. 4.8 (a). Comparing with TPF1, the bands around a DWN exhibit quadratic dispersion behavior [53, 78]. The DWN also needs the protection from point group symmetry and gives rise to two Fermi arcs. But this is beyond the scope of this dissertation.

For the second class of TPF, which is named as TPF2 here, two of the three bands

are degenerate and form several nodal lines either along the high symmetry lines or in the mirror planes. Each nodal line connects two TPF2 as shown in Fig. 4.8 (d) and (e). Thus it is impossible to find a closed 2D manifold enclosing a TPF2 but gapped everywhere. The definition of topological charge for Weyl and TPF1 is not applicable for TPF2. Instead, the one dimensional (1D) topological invariant of a nodal line [87–89], namely the Z_2 number [90], can be applied to characterize the topology of the TPF2 [39, 79]. For each nodal line of the TPF2, we choose a closed loop l , along which the Hamiltonian is gapped, to enclose the nodal line. The Z_2 number ζ is simply the Berry phase on the closed loop :

$$\zeta = \frac{1}{\pi} \sum_n \oint_l \mathbf{A}_n(\mathbf{k}) \cdot d\mathbf{k} \text{ mod } 2.$$

Where $\mathbf{A}_n(\mathbf{k})$ is the Berry connection of the occupied bands. The Berry phase accumulated by valence bands is quantized to be either 0 or π , corresponding to Z_2 number of either 0 or 1. Therefore, the TPF2 can be further classified to type TPF2a for $\zeta = 0$ and type TPF2b for $\zeta = 1$ as shown in Fig. 4.8 (d) and Fig. 4.8 (e), respectively.

According to the group theory, to form a TPF, the little group at the TPF point should contain both one- and two- dimensional double group representations. These symmetry requirements can be satisfied by the C_{3v} symmetry, which is the case for TPF1 and TPF2b. While for TPF2a, apart from the C_{3v} symmetry, an additional symmetry, which is the product of the mirror plane σ_h orthogonal to the C_3 axis and time-reversal symmetry, is necessary. In this case, although the Z_2 number of TPF2a is zero, a mirror Chern number $C_{m=\pm i}$ of σ_h [91, 92] can be defined in the way:

$$C_{m=\pm i} = \frac{1}{2\pi} \sum_n \int_{\mathbf{S}} \mathbf{B}_n(\mathbf{k}) \cdot d\mathbf{S}(\mathbf{k}) \text{ mod } 2.$$

Where the $\mathbf{B}_n(k)$ is the berry curvature of the occupied bands, \mathbf{S} is the mirror plane. It has been proved that TPF2a has non-zero mirror Chern number $C_{m=\pm i}$. In a consequence, all types of TPFs are topologically non-trivial and are able to find related

topological surface states.

Chapter 5

Selected results

5.1 Introduction

In this chapter, selected publications are presented, which provide the main results of the cumulative thesis. The investigated topics roughly follow the evolution of the degeneracy of the quasiparticles, beginning with the two-fold degenerate Weyl points, then three-fold degenerate Triple points, and finally the four-fold degenerate Dirac points. The degeneracies of these quasiparticles are determined by the symmetry of the systems of interest. With either time-reversal or inversion symmetry broken, Weyl points are able to exist. They can derive to Triple points with high order rotation axis or to Dirac points with the presence of both time-reversal and inversion symmetries.

5.2 Paper I: Topological Weyl semimetals in the chiral antiferromagnetic materials Mn_3Ge and Mn_3Sn

This work, which was done in collaboration with the group of Binghai Yan and Claudia Felser from the Max-Planck Institute for Chemical Physics of Solids, was motivated by

the discovery of large anomalous Hall effect (AHE) in the non-collinear antiferromagnet Mn_3Ir [93]. It was shown that the large AHE arises from the non-zero net Berry curvature in the first BZ because of the magnetic structure. This reminds us of the possibility of finding Weyl points in those triangular magnetic ordered materials. Because the Weyl points are closely related to the Berry curvature and the time-reversal symmetry has been broken by the non-collinear anti-ferromagnetic structure.

Our deduction was verified by the *ab-initio* calculations. Multiple pairs of Weyl points were observed in Mn_3Ge and Mn_3Sn , most of which are type-II. Among them, some are connected by visible fermi arcs, while others are mixed with the bulk states. The positions and topological charges of the Weyl points are in accordance with the symmetry of the magnetic lattice. Moreover, based on the Wannier functions, the Berry curvature around the Weyl points is calculated, demonstrating strong anisotropic but monopole-like distribution. By integrating the Berry curvature in the first BZ, we also showed that both Mn_3Ge and Mn_3Sn exhibit large AHE.



PAPER

Topological Weyl semimetals in the chiral antiferromagnetic materials Mn_3Ge and Mn_3Sn

OPEN ACCESS

RECEIVED

10 August 2016

REVISED

15 November 2016

ACCEPTED FOR PUBLICATION

19 December 2016

PUBLISHED

20 January 2017

Hao Yang^{1,2}, Yan Sun¹, Yang Zhang^{1,3}, Wu-Jun Shi^{1,4}, Stuart S P Parkin² and Binghai Yan^{1,5}¹ Max Planck Institute for Chemical Physics of Solids, D-01187 Dresden, Germany² Max Planck Institute of Microstructure Physics, Weinberg 2, D-06120 Halle, Germany³ Leibniz Institute for Solid State and Materials Research, D-01069 Dresden, Germany⁴ School of Physical Science and Technology, ShanghaiTech University, Shanghai 200031, People's Republic of China⁵ Max Planck Institute for the Physics of Complex Systems, D-01187 Dresden, GermanyE-mail: yan@cpfs.mpg.de

Original content from this work may be used under the terms of the [Creative Commons Attribution 3.0 licence](https://creativecommons.org/licenses/by/4.0/).

Any further distribution of this work must maintain attribution to the author(s) and the title of the work, journal citation and DOI.

**Keywords:** Weyl semimetal, antiferromagnetism, anomalous Hall effect, surface states, Fermi arcs**Abstract**

Recent experiments revealed that Mn_3Sn and Mn_3Ge exhibit a strong anomalous Hall effect at room temperature, provoking us to explore their electronic structures for topological properties. By *ab initio* band structure calculations, we have observed the existence of multiple Weyl points in the bulk and corresponding Fermi arcs on the surface, predicting antiferromagnetic Weyl semimetals in Mn_3Ge and Mn_3Sn . Here the chiral antiferromagnetism in the Kagome-type lattice structure is essential to determine the positions and numbers of Weyl points. Our work further reveals a new guiding principle to search for magnetic Weyl semimetals among materials that exhibit a strong anomalous Hall effect.

1. Introduction

Recent discovery of Weyl semimetals (WSMs) [1–3] in realistic materials has stimulated tremendous research interest in topological semimetals, such as WSMs, Dirac semimetals, and nodal line semimetals [4–9], as a new frontier of condensed matter physics after the discovery of topological insulators [10, 11]. The WSMs are of particular interest not only because of their exotic Fermi-arc-type surface states but also because of their appealing bulk chiral magneto-transport properties, such as the chiral anomaly effect [12–14], nonlocal transport [15, 16], large magnetoresistance, and high mobility [17]. Currently discovered WSM materials can be classified into two groups. One group breaks crystal inversion symmetry but preserves time-reversal symmetry (e.g., TaAs-family transition-metal pnictides [18, 19] and WTe_2 - and $MoTe_2$ -family transition-metal dichalcogenides [20–26]). The other group breaks time-reversal symmetry in ferromagnets with possible tilted moments (e.g., magnetic Heusler $GdPtBi$ [27, 28] and $YbMnBi_2$ [29]). An antiferromagnetic (AFM) WSM compound has yet to be found, although $Y_2Ir_2O_7$ with a noncoplanar AFM structure was theoretically predicted to be a WSM candidate [5].

In a WSM, the conduction and valence bands cross each other linearly through nodes called Weyl points. Between a pair of Weyl points with opposite chiralities (sink or source of the Berry curvature) [4], the emerging Berry flux can lead to the anomalous Hall effect (AHE) [30], as observed in $GdPtBi$ [27, 28], and an intrinsic spin Hall effect (SHE), as predicted in TaAs-type materials [31], for systems without and with time-reversal symmetry, respectively. Herein, we raise a simple recipe to search for WSM candidates among materials that host strong AHE or SHE.

Recently, Mn_3X (where $X = Sn, Ge, \text{ and } Ir$), which exhibit noncollinear antiferromagnetic (AFM) phases at room temperature, have been found to show large AHE [32–35] and SHE [36], provoking our interest to investigate their band structures for possible WSMs. In this work, we report the existence of Weyl fermions for Mn_3Ge and Mn_3Sn compounds and the resultant Fermi arcs on the surface by *ab initio* calculations, awaiting experimental verifications. Dozens of Weyl points exist near the Fermi energy in their band structure, and these can be well understood with the assistance of lattice symmetry.

2. Methods

The electronic ground states of Mn₃Ge and Mn₃Sn were calculated by using density-functional theory (DFT) within the Perdew–Burke–Ernzerhof-type generalized-gradient approximation (GGA) [37] using the Vienna *ab initio* simulation package (VASP) [38]. The 3d⁶4s¹, 4s²4p², and 5s²5p² electrons were considered as valance electrons for Mn, Ge, and Sn atoms, respectively. The primitive cell with experimental crystal parameters $a = b = 5.352$ and $c = 4.312$ Å for Mn₃Ge and $a = b = 5.67$ and $c = 4.53$ Å for Mn₃Sn were adopted. Spin-orbit coupling (SOC) was included in all calculations.

To identify the Weyl points with the monopole feature, we calculated the Berry curvature distribution in momentum space. The Berry curvature was calculated based on a tight-binding Hamiltonian based on localized Wannier functions [39] projected from the DFT Bloch wave functions. Chosen were atomic-orbital-like Wannier functions, which include Mn-sp_d and Ge-sp/Sn-p orbitals, so that the tight-binding Hamiltonian is consistent with the symmetry of *ab initio* calculations. From such a Hamiltonian, the Berry curvature can be calculated using the Kubo-formula approach [40]

$$\Omega_n^\gamma(\vec{k}) = 2i\hbar^2 \sum_{m \neq n} \frac{\langle u_n(\vec{k}) | \hat{v}_\alpha | u_m(\vec{k}) \rangle \langle u_m(\vec{k}) | \hat{v}_\beta | u_n(\vec{k}) \rangle}{(E_n(\vec{k}) - E_m(\vec{k}))^2}, \quad (1)$$

where $\Omega_n^\gamma(\vec{k})$ is the Berry curvature in momentum space for a given band n , $\hat{v}_{\alpha(\beta,\gamma)} = \frac{1}{\hbar} \frac{\partial \hat{H}}{\partial k_{\alpha(\beta,\gamma)}}$ is the velocity operator with $\alpha, \beta, \gamma = x, y, z$, and $|u_n(\vec{k})\rangle$ and $E_n(\vec{k})$ are the eigenvector and eigenvalue of the Hamiltonian $\hat{H}(\vec{k})$, respectively. The summation of $\Omega_n^\gamma(\vec{k})$ over all valance bands gives the Berry curvature vector Ω ($\Omega^x, \Omega^y, \Omega^z$).

In addition, the surface states that demonstrate the Fermi arcs were calculated on a semi-infinite surface, where the momentum-resolved local density of states (LDOS) on the surface layer was evaluated based on the Green's function method. We note that the current surface band structure corresponds to the bottom surface of a half-infinite system.

3. Results and discussion

3.1. Symmetry analysis of the AFM structure

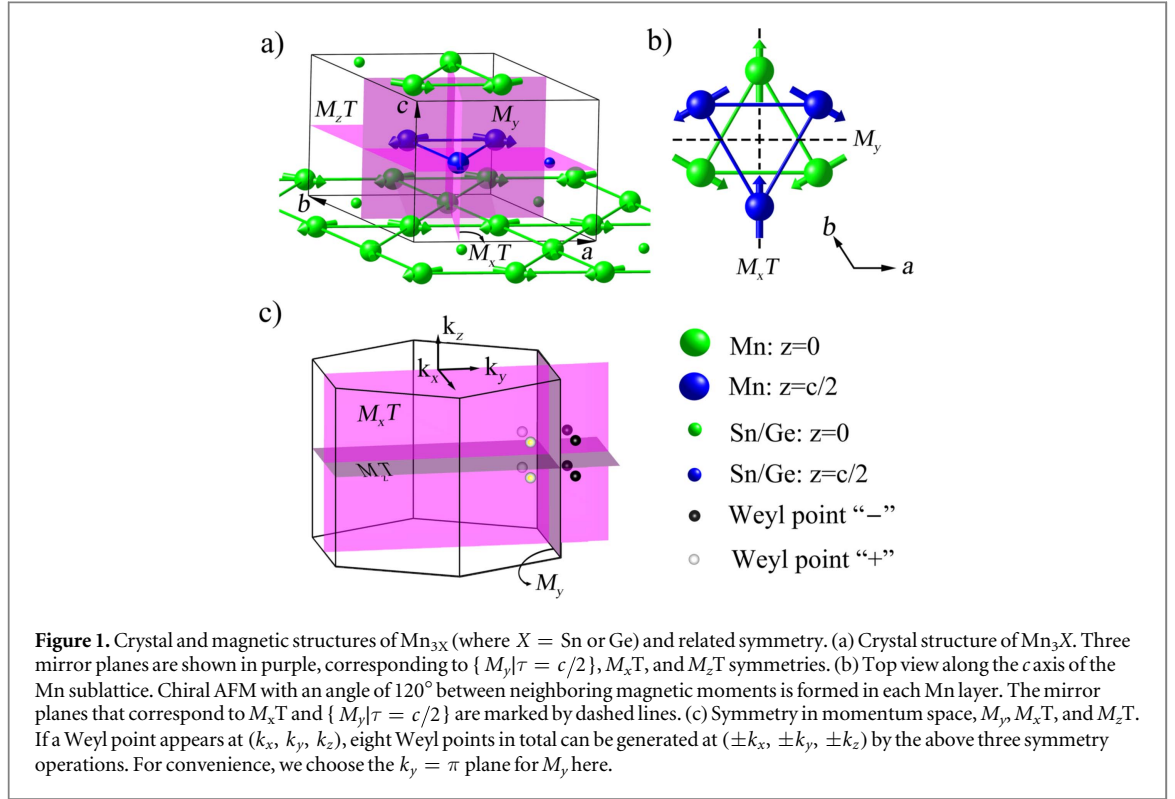
Mn₃Ge and Mn₃Sn share the same layered hexagonal lattice (space group $P6_3/mmc$, No. 194). Inside a layer, Mn atoms form a Kagome-type lattice with mixed triangles and hexagons and Ge/Sn atoms are located at the centers of these hexagons. Each Mn atom carries a magnetic moment of 3.2 μ B in Mn₃Sn and 2.7 μ B in Mn₃Ge. As revealed in a previous study [41], the ground magnetic state is a noncollinear AFM state, where Mn moments align inside the *ab* plane and form 120° angles with neighboring moment vectors, as shown in figure 1(b). Along the *c* axis, stacking two layers leads to the primitive unit cell. Given the magnetic lattice, these two layers can be transformed into each other by inversion symmetry or with a mirror reflection (M_y) adding a half-lattice ($c/2$) translation, i.e., a nonsymmorphic symmetry $\{M_y | \tau = c/2\}$. In addition, two other mirror reflections (M_x and M_z) adding time reversal (T), $M_x T$ and $M_z T$, exist.

In momentum space, we can utilize three important symmetries, $M_x T$, $M_z T$, and M_y , to understand the electronic structure and locate the Weyl points. Suppose a Weyl point with chirality χ (+ or −) exists at a generic position \mathbf{k} (k_x, k_y, k_z). Mirror reflection reverses χ while time reversal does not and both of them act on \mathbf{k} . Further, mirror reflection M_γ preserves the Berry curvature Ω^γ while time reversal reserves it. The transformation is as follows:

$$\begin{aligned} M_x T : (k_x, k_y, k_z) &\rightarrow (k_x, -k_y, -k_z); \chi \rightarrow -\chi; \Omega^x \rightarrow -\Omega^x \\ M_z T : (k_x, k_y, k_z) &\rightarrow (-k_x, -k_y, k_z); \chi \rightarrow -\chi; \Omega^z \rightarrow -\Omega^z \\ M_y : (k_x, k_y, k_z) &\rightarrow (k_x, -k_y, k_z); \chi \rightarrow -\chi; \Omega^y \rightarrow +\Omega^y. \end{aligned} \quad (2)$$

Each of the above three operations doubles the number of Weyl points. Thus, eight nonequivalent Weyl points can be generated at $(\pm k_x, +k_y, \pm k_z)$ with chirality χ and $(\pm k_x, -k_y, \pm k_z)$ with chirality $-\chi$ (see figure 1(c)). We note that the $k_x = 0/\pi$ or $k_z = 0/\pi$ plane can host Weyl points. However, the $k_y = 0/\pi$ plane cannot host Weyl points, because M_y simply reverses the chirality and annihilates the Weyl point with its mirror image if it exists.

In addition, the symmetry of the 120° AFM state is slightly broken in the materials, owing to the existence of a tiny net moment (~ 0.003 μ B per unit cell) [41–43]. Such weak symmetry breaking seems to induce negligible effects in the transport measurement. However, it gives rise to a perturbation of the band structure, for example, shifting slightly the mirror image of a Weyl point from its position expected, as we will see in the surface states of Mn₃Ge.



3.2. The anomalous Hall effect

The intrinsic anomalous Hall conductivity σ_γ ($\gamma = x, y, z$) can be calculated by integrating the Berry curvature Ω^γ over the whole Brillouin zone [40, 44]

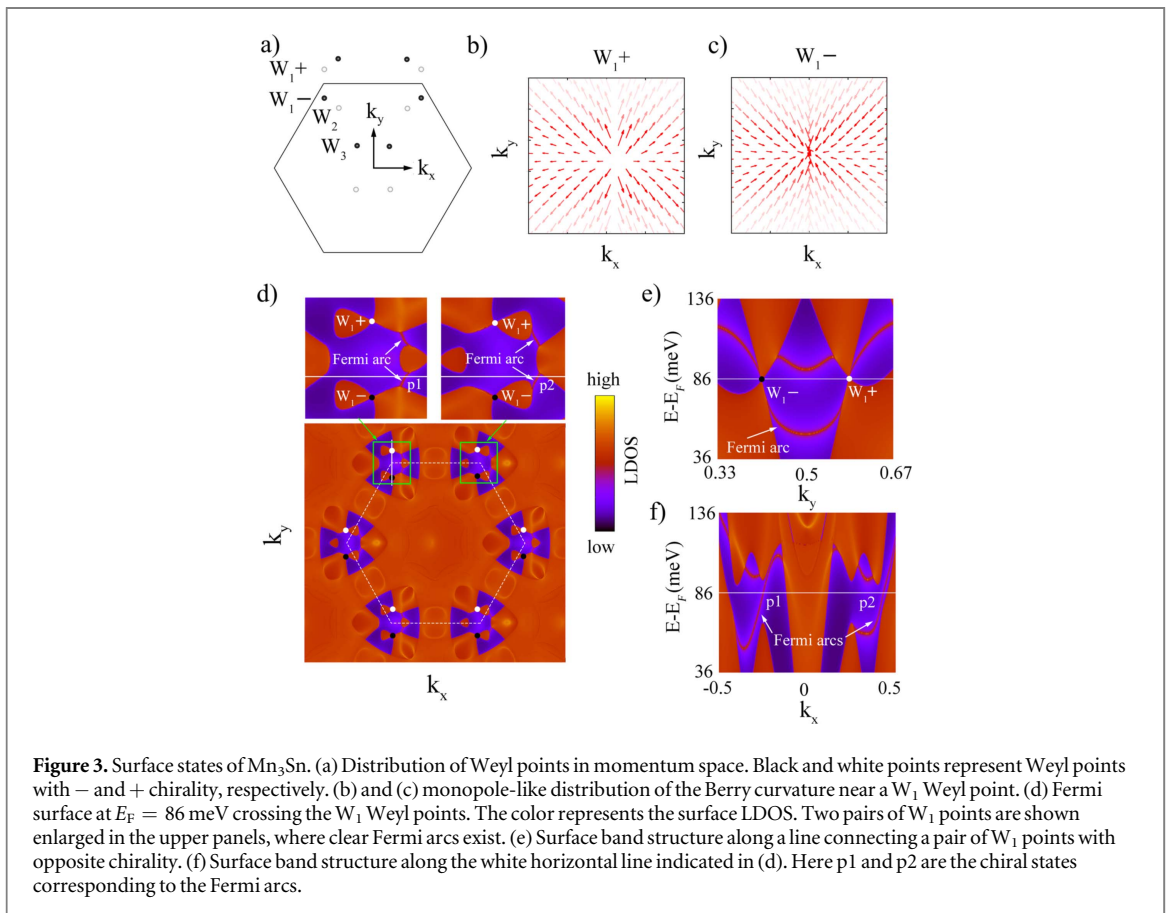
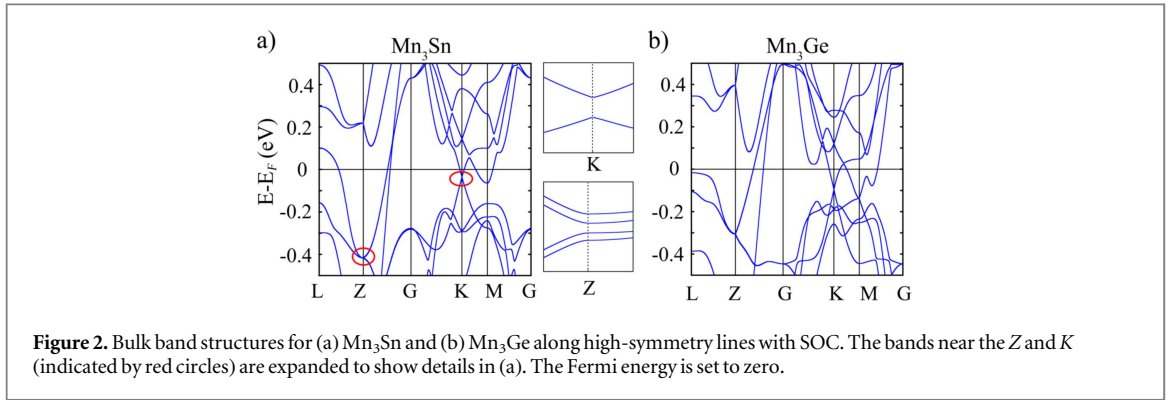
$$\sigma^\gamma = -\frac{e^2}{\hbar} \int_{BZ} \frac{d^3\vec{k}}{(2\pi)^3} f_n(\vec{k}) \Omega^\gamma(\vec{k}). \quad (3)$$

According to equation (2), Ω^x and Ω^z are odd with respect to M_xT and M_yT , respectively. Thus, corresponding σ^x and σ^z are zero. Since Ω^y is even with respect to the M_y mirror plane, corresponding σ^y is nonzero. This is also consistent with the distribution of Weyl points in the k -space. As shown in figure 1(c), only ‘+’ Weyl points appear on one side of the M_y plane and only ‘-’ Weyl points locate on the other side of M_y plane. Then there are net Berry flux (starting from ‘+’ to ‘-’ Weyl points) Ω^y crossing the M_y plane, resulting in the nonzero anomalous Hall conductivity σ^y . In contrast, an equal number of ‘+’ and ‘-’ Weyl points appear on each side of M_x (M_z) planes. Consequently, the net Berry flux of Ω^x (Ω^z) should be zero, giving rise to vanishing σ^x (σ^z). According to recent numerical calculations [36], $\sigma^y = 330(133) S^{-1} cm^{-1}$ for Mn_3Ge (Mn_3Sn).

In the measurement of AHE, an external magnetic field is usually applied to uniform different magnetic domains. Further, for Mn_3Ge and Mn_3Sn , the triangular spins can be rotated inside the xy plane even by a very weak magnetic field due to the residual magnetic moment [43]. The rotation of an arbitrary angle can break the M_y and M_xT symmetry, showing nonzero σ^y and σ^x . However, σ^z is still zero due to the M_zT symmetry. As observed for both compounds in experiment [34, 35], $\sigma^{x,y}$ are indeed very large and σ^z is negligible. The in-plane anomalous Hall conductivity is about $500(100) S^{-1} cm^{-1}$ for Mn_3Ge (Mn_3Sn) at low temperature, which are in the same order of magnitude as the calculations [36].

3.3. Weyl points in the bulk band structure

The bulk band structures are shown along high-symmetry lines in figure 2 for Mn_3Ge and Mn_3Sn . It is not surprising that the two materials exhibit similar band dispersions. At first glance, one can find two seemingly band degenerate points at Z and K points, which are below the Fermi energy. Because of M_zT and the nonsymmorphic symmetry $\{M_y|\tau = c/2\}$, the bands are supposed to be quadruply degenerate at the Brillouin zone boundary Z , forming a Dirac point protected by the nonsymmorphic space group [45–47]. Given the slight mirror symmetry breaking by the residual net magnetic moment, this Dirac point is gapped at Z (as shown in the enlarged panel) and splits into four Weyl points, which are very close to each other in k space. A tiny gap also appears at the K point. Nearby, two additional Weyl points appear, too. Since the Weyl point separations are too small near both Z and K points, these Weyl points may generate little observable consequence in experiments such as those for studying Fermi arcs. Therefore, we will not focus on them in the following investigation.



Mn_3Sn and Mn_3Ge are actually metallic, as seen from the band structures. However, we retain the terminology of Weyl semimetal for simplicity and consistency. The valence and conduction bands cross each many times near the Fermi energy, generating multiple pairs of Weyl points. We first investigate the Sn compound. Supposing that the total valence electron number is N_v , we search for the crossing points between the N_v^{th} and $(N_v + 1)^{\text{th}}$ bands.

As shown in figure 3(a), there are six pairs of Weyl points in the first Brillouin zone; these can be classified into three groups according to their positions, noted as W_1 , W_2 , and W_3 . These Weyl points lie in the M_z plane (with W_2 points being only slightly off this plane owing to the residual-moment-induced symmetry breaking) and slightly above the Fermi energy. Therefore, there are four copies for each of them according to the symmetry analysis in equation (2). Their representative coordinates and energies are listed in table 1 and also indicated in figure 3(a). A Weyl point (e.g., W_1 in figures 3(b) and (c)) acts as a source or sink of the Berry curvature Ω , clearly showing the monopole feature with a definite chirality.

In contrast to Mn_3Sn , Mn_3Ge displays many more Weyl points. As shown in figure 4(a) and listed in table 2, there are nine groups of Weyl points. Here $W_{1,2,7,9}$ lie in the M_z plane with W_9 on the k_y axis, W_4 appears in the M_x plane, and the others are in generic positions. Therefore, there are four copies of $W_{1,2,7,4}$, two copies of W_9 , and eight copies of other Weyl points. Although there are many other Weyl points in higher energies owing to

Table 1. Positions and energies of Weyl points in first Brillouin zone for Mn_3Sn . The positions (k_x, k_y, k_z) are in units of π . Energies are relative to the Fermi energy E_F . Each type of Weyl point has four copies whose coordinates can be generated from the symmetry as $(\pm k_x, \pm k_y, k_z = 0)$.

Weyl point	k_x	k_y	k_z	Chirality	Energy (meV)
W_1	-0.325	0.405	0.000	-	86
W_2	-0.230	0.356	0.003	+	158
W_3	-0.107	0.133	0.000	-	493

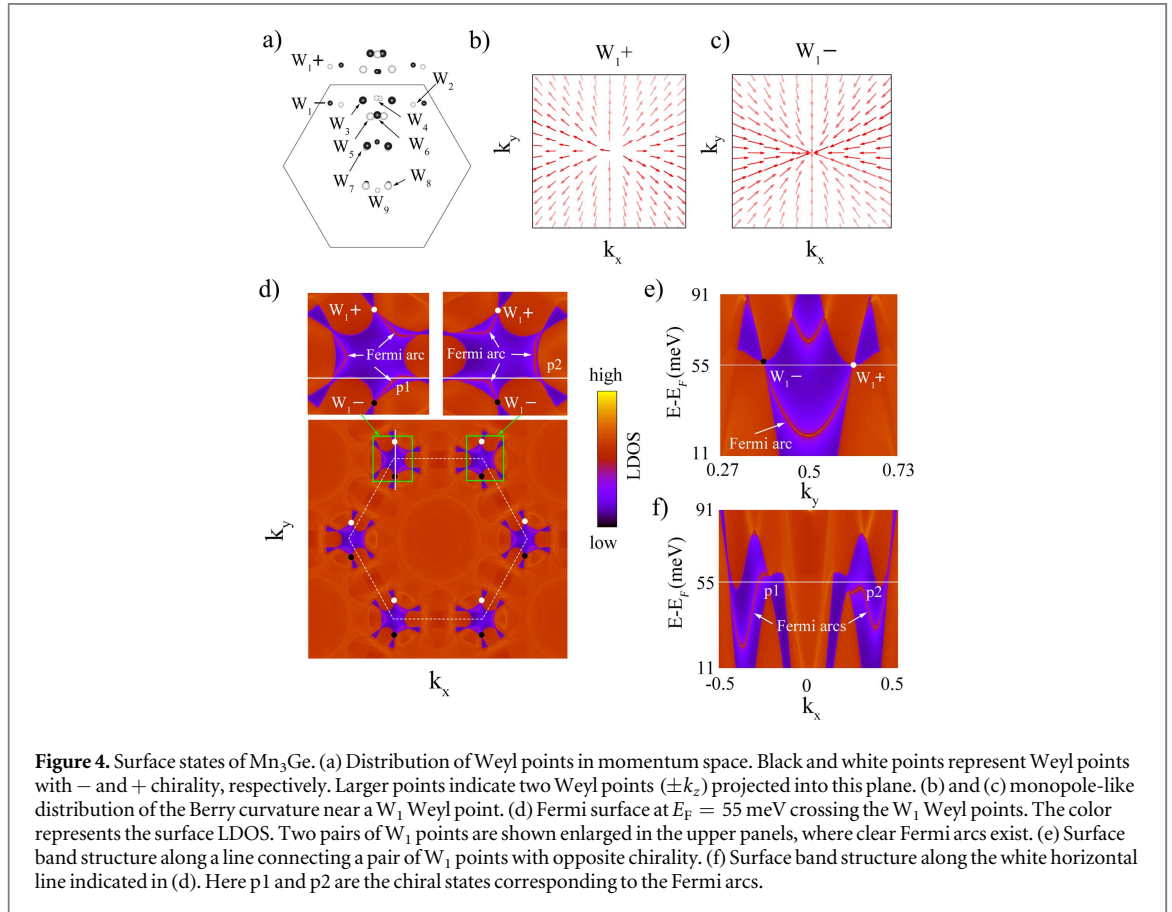


Figure 4. Surface states of Mn_3Ge . (a) Distribution of Weyl points in momentum space. Black and white points represent Weyl points with - and + chirality, respectively. Larger points indicate two Weyl points $(\pm k_z)$ projected into this plane. (b) and (c) monopole-like distribution of the Berry curvature near a W_1 Weyl point. (d) Fermi surface at $E_F = 55$ meV crossing the W_1 Weyl points. The color represents the surface LDOS. Two pairs of W_1 points are shown enlarged in the upper panels, where clear Fermi arcs exist. (e) Surface LDOS. (f) Surface band structure along a line connecting a pair of W_1 points with opposite chirality. Here p1 and p2 are the chiral states corresponding to the Fermi arcs.

Table 2. Positions and energies of Weyl points in the first Brillouin zone for Mn_3Ge . The positions (k_x, k_y, k_z) are in units of π . Energies are relative to the Fermi energy E_F . Each of $W_{1,2,7}$ has four copies whose coordinates can be generated from the symmetry as $(\pm k_x, \pm k_y, k_z = 0)$. W_4 has four copies at $(k_x \approx 0, \pm k_y, \pm k_z)$ and W_9 has two copies at $(k_x \approx 0, \pm k_y, k_z = 0)$. Each of the other Weyl points has four copies whose coordinates can be generated from the symmetry as $(\pm k_x, \pm k_y, \pm k_z)$.

Weyl point	k_x	k_y	k_z	Chirality	Energy (meV)
W_1	-0.333	0.388	-0.000	-	57
W_2	0.255	0.378	-0.000	+	111
W_3	-0.101	0.405	0.097	-	48
W_4	-0.004	0.419	0.131	+	8
W_5	-0.048	0.306	0.164	+	77
W_6	0.002	0.314	0.171	-	59
W_7	-0.081	0.109	0.000	+	479
W_8	0.069	-0.128	0.117	+	330
W_9	0.004	-0.149	-0.000	+	470

different band crossings, we mainly focus on the current Weyl points that are close to the Fermi energy. The monopole-like distribution of the Berry curvature near these Weyl points is verified; see W_1 in figure 4 as an example. Without including SOC, we observed a nodal-ring-like band crossing in the band structures of both Mn_3Sn and Mn_3Ge . SOC gaps the nodal rings but leaves isolating band-touching points, i.e., Weyl points. Since Mn_3Sn exhibits stronger SOC than Mn_3Ge , many Weyl points with opposite chirality may annihilate each other by being pushed by the strong SOC in Mn_3Sn . This might be why Mn_3Sn exhibits fewer Weyl points than Mn_3Ge .

3.4. Fermi arcs on the surface

The existence of Fermi arcs on the surface is one of the most significant consequences of Weyl points inside the three-dimensional (3D) bulk. We first investigate the surface states of Mn_3Sn that have a simple bulk band structure with fewer Weyl points. When projecting $W_{2,3}$ Weyl points to the (001) surface, they overlap with other bulk bands that overwhelm the surface states. Luckily, W_1 Weyl points are visible on the Fermi surface. When the Fermi energy crosses them, W_1 Weyl points appear as the touching points of neighboring hole and electron pockets. Therefore, they are typical type-II Weyl points [20, 48]. Indeed, their energy dispersions demonstrate strongly tilted Weyl cones.

The Fermi surface of the surface band structure is shown in figure 3(d) for the Sn compound. In each corner of the surface Brillouin zone, a pair of W_1 Weyl points exists with opposite chirality. Connecting such a pair of Weyl points, a long Fermi arc appears in both the Fermi surface (figure 3(d) and the band structure (figure 3(e)). Although the projection of bulk bands exhibit pseudo-symmetry of a hexagonal lattice, the surface Fermi arcs do not. It is clear that the Fermi arcs originating from two neighboring Weyl pairs (see figure 3(d)) do not exhibit M_x reflection, because the chirality of Weyl points apparently violates M_x symmetry. For a generic k_x-k_z plane between each pair of W_1 Weyl points, the net Berry flux points in the $-k_y$ direction. As a consequence, the Fermi velocities of both Fermi arcs point in the $+k_x$ direction on the bottom surface (see figure 3(f)). These two right movers coincide with the nonzero net Berry flux, i.e., Chern number = 2.

For Mn_3Ge , we also focus on the W_1 -type Weyl points at the corners of the hexagonal Brillouin zone. In contrast to Mn_3Sn , Mn_3Ge exhibits a more complicated Fermi surface. Fermi arcs exist to connect a pair of W_1 -type Weyl points with opposite chirality, but they are divided into three pieces as shown in figure 4(d). In the band structures (see figures 4(e) and (f)), these three pieces are indeed connected together as a single surface state. Crossing a line between two pairs of W_1 points, one can find two right movers in the band structure, which are indicated as p1 and p2 in figure 4(f). The existence of two chiral surface bands is consistent with a nontrivial Chern number between these two pairs of Weyl points.

4. Summary

In summary, we have discovered the Weyl semimetal state in the chiral AFM compounds Mn_3Sn and Mn_3Ge by *ab initio* band structure calculations. Multiple Weyl points were observed in the bulk band structures, most of which are type II. The positions and chirality of Weyl points are in accordance with the symmetry of the magnetic lattice. For both compounds, Fermi arcs were found on the surface, each of which connects a pair of Weyl points with opposite chirality, calling for further experimental investigations such as angle-resolved photoemission spectroscopy. The discovery of Weyl points verifies the large anomalous Hall conductivity observed recently in titled compounds. Our work further reveals a guiding principle to search for Weyl semimetals among materials that exhibit a strong anomalous Hall effect.

Acknowledgments

We thank Claudia Felser, Jürgen Kübler and Ajaya K Nayak for helpful discussions. We acknowledge the Max Planck Computing and Data Facility (MPCDF) and Shanghai Supercomputer Center for computational resources and the German Research Foundation (DFG) SFB-1143 for financial support.

References

- [1] Lv B Q *et al* 2015 *Phys. Rev. X* **5** 031013
- [2] Xu S-Y *et al* 2015 *Science* **349** 613
- [3] Yang L X *et al* 2015 *Nat. Phys.* **11** 728
- [4] Volovik G E 2003 *The Universe in a Helium Droplet* (Oxford: Clarendon)
- [5] Wan X G, Turner A M, Vishwanath A and Savrasov S Y 2011 *Phys. Rev. B* **83** 205101
- [6] Balents L 2011 *Physics* **4** 36
- [7] Burkov A A, Hook M D and Balents L 2011 *Phys. Rev. B* **84** 235126

- [8] Hosur P and Qi X L 2013 *C. R. Phys.* **14** 857
- [9] Vafeek O and Vishwanath A 2014 *Annu. Rev. Condens. Matter Phys.* **5** 83
- [10] Qi X-L and Zhang S-C 2011 *Rev. Mod. Phys.* **83** 1057
- [11] Hasan M Z and Kane C L 2010 *Rev. Mod. Phys.* **82** 3045
- [12] Xiong J, Kushwaha S K, Liang T, Krizan J W, Hirschberger M, Wang W, Cava R J and Ong N P 2015 *Science* **350** 413
- [13] Huang X et al 2015 *Phys. Rev. X* **5** 031023
- [14] Arnold F et al 2016 *Nat. Commun.* **7** 11615
- [15] Parameswaran S, Grover T, Abanin D, Pesin D and Vishwanath A 2014 *Phys. Rev. X* **4** 031035
- [16] Baum Y, Berg E, Parameswaran S A and Stern A 2015 *Phys. Rev. X* **5** 041046
- [17] Shekhar C et al 2015 *Nat. Phys.* **11** 645
- [18] Weng H, Fang C, Fang Z, Bernevig B A and Dai X 2015 *Phys. Rev. X* **5** 011029
- [19] Huang S-M et al 2015 *Nat. Commun.* **6** 8373
- [20] Soluyanov A A, Gresch D, Wang Z, Wu Q, Troyer M, Dai X and Bernevig B A 2015 *Nature* **527** 495
- [21] Sun Y, Wu S C, Ali M N, Felser C and Yan B 2015 *Phys. Rev. B* **92** 161107R
- [22] Wang Z, Gresch D, Soluyanov A A, Xie W, Kushwaha S, Dai X, Troyer M, Cava R J and Bernevig B A 2016 *Phys. Rev. Lett.* **117** 056805
- [23] Koepf K, Kasinathan D, Efremov D V, Khim S, Borisenko S, Büchner B and van den Brink J 2016 *Phys. Rev. B* **93** 201101
- [24] Deng K et al 2016 *Nat. Phys.* **12** 1105-10
- [25] Jiang J et al 2016 arXiv:1604.00139
- [26] Tamai A et al 2016 *Phys. Rev. X* **6** 031021
- [27] Hirschberger M, Kushwaha S, Wang Z, Gibson Q, Liang S, Belvin C A, Bernevig B A, Cava R J and Ong N P 2016 *Nat. Mater.* **15** 1161
- [28] Shekhar C, Nayak A K, Singh S and Kumar N 2016 arXiv:1604.01641
- [29] Borisenko S, Evtushinsky D, Gibson Q, Yaresko A, Kim T, Ali M N, Buechner B, Hoesch M and Cava R J 2015 arXiv:1507.04847
- [30] Burkov A A 2014 *Phys. Rev. Lett.* **113** 187202
- [31] Sun Y, Zhang Y, Felser C and Yan B 2016 *Phys. Rev. Lett.* **117** 146403
- [32] Kübler J and Felser C 2014 *Europhys. Lett.* **108** 67001
- [33] Chen H, Niu Q and MacDonald A H 2014 *Phys. Rev. Lett.* **112** 017205
- [34] Nakatsuji S, Kiyohara N and Higo T 2015 *Nature* **527** 212
- [35] Nayak A K et al 2016 *Sci. Adv.* **2** e1501870
- [36] Zhang W, Han W, Yang S H, Sun Y, Zhang Y, Yan B and Parkin S 2016 *Sci. Adv.* **2** e1600759
- [37] Perdew J P, Burke K and Ernzerhof M 1996 *Phys. Rev. Lett.* **77** 3865
- [38] Kresse G and Furthmüller J 1996 *Comput. Mater. Sci.* **6** 15
- [39] Mostofi A A, Yates J R, Lee Y-S, Souza I, Vanderbilt D and Marzari N 2008 *Comput. Phys. Commun.* **178** 685
- [40] Xiao D, Chang M-C and Niu Q 2010 *Rev. Mod. Phys.* **82** 1959
- [41] Zhang D, Yan B, Wu S-C, Kübler J, Kreiner G, Parkin S S and Felser C 2013 *J. Phys.: Condens. Matter* **25** 206006
- [42] Nagamiya T, Tomiyoshi S and Yamaguchi Y 1982 *Solid State Commun.* **42** 385
- [43] Tomiyoshi S and Yamaguchi Y 1982 *J. Phys. Soc. Japan* **51** 2478
- [44] Nagaosa N, Sinova J, Onoda S, MacDonald A H and Ong N P 2010 *Rev. Mod. Phys.* **82** 1539
- [45] Young S M, Zaheer S, Teo J C Y, Kane C L, Mele E J and Rappe A M 2012 *Phys. Rev. Lett.* **108** 140405
- [46] Schoop L M, Ali M N, Straßer C, Topp A, Varykhalov A, Marchenko D, Duppl V, Parkin S S P, Lotsch B V and Ast C R 2000 *Nat. Commun.* **7** 11696
- [47] Tang P, Zhou Q, Xu G and Zhang S-C 2016 *Nat. Phys.* **12** 1100-4
- [48] Yong X, Fan Z and Chuanwei Z 2015 *Phys. Rev. Lett.* **115** 265304

5.3 Paper II: Strong anisotropic anomalous Hall effect and spin Hall effect in the chiral antiferromagnetic compounds Mn_3X (X= Ge, Sn, Ga, Ir, Rh, and Pt)

This publication, shortly after the discovery of Weyl points in the chiral antiferromagnetic ordered materials, systematically studied their intrinsic AHE and SHE. Apart from the aforementioned hexagonal materials, the cubic structure materials are also calculated, including Mn_3Ir , Mn_3Pt and Mn_3Rh . We found that all the studied materials show strong anisotropic anomalous Hall conductivity (AHC) and spin Hall conductivity (SHC). This suggests the possibility of optimization AHC or SHC by choosing appropriate crystal planes and by applying field along certain directions.

Moreover, our results also indicate that the SHC and AHC are functions of Fermi level, which can be tuned by electron or hole doping. This provides another approach of experimental obtaining higher SHC and AHC. One interesting result we didn't mention in the paper is the relation between the Weyl points and AHC. It is natural to think that the AHC is dominated by the number of Weyl points in a material. However, in our calculations, we found that the Berry curvature which dominates the main part of AHC is not from the Weyl points but from the regions which have tiny band gaps. We think this is partly because Weyl points are singularities of Berry curvature which will be averaged by integration. Another reason might be that the Berry curvature from the opposite Weyl points will cancel with each other. Because of these properties, the intrinsic AHC and SHC are sensitive to the detailed band structure. The way of tuning band structure can be an effective method of tuning the intrinsic AHC and SHC.

Strong anisotropic anomalous Hall effect and spin Hall effect in the chiral antiferromagnetic compounds Mn_3X ($X = Ge, Sn, Ga, Ir, Rh, \text{ and } Pt$)

Yang Zhang,^{1,2} Yan Sun,¹ Hao Yang,^{1,3} Jakub Železný,¹ Stuart P. P. Parkin,³ Claudia Felser,¹ and Binghai Yan^{1,4,*}

¹Max Planck Institute for Chemical Physics of Solids, 01187 Dresden, Germany

²Leibniz Institute for Solid State and Materials Research, 01069 Dresden, Germany

³Max Planck Institute of Microstructure Physics, Weinberg 2, 06120 Halle, Germany

⁴Max Planck Institute for the Physics of Complex Systems, 01187 Dresden, Germany

(Received 13 October 2016; published 15 February 2017)

We have carried out a comprehensive study of the intrinsic anomalous Hall effect and spin Hall effect of several chiral antiferromagnetic compounds Mn_3X ($X = Ge, Sn, Ga, Ir, Rh$ and Pt) by *ab initio* band structure and Berry phase calculations. These studies reveal large and anisotropic values of both the intrinsic anomalous Hall effect and spin Hall effect. The Mn_3X materials exhibit a noncollinear antiferromagnetic order which, to avoid geometrical frustration, forms planes of Mn moments that are arranged in a Kagome-type lattice. With respect to these Kagome planes, we find that both the anomalous Hall conductivity (AHC) and the spin Hall conductivity (SHC) are quite anisotropic for any of these materials. Based on our calculations, we propose how to maximize AHC and SHC for different materials. The band structures and corresponding electron filling, that we show are essential to determine the AHC and SHC, are compared for these different compounds. We point out that Mn_3Ga shows a large SHC of about $600 (\hbar/e)(\Omega \text{ cm})^{-1}$. Our work provides insights into the realization of strong anomalous Hall effects and spin Hall effects in chiral antiferromagnetic materials.

DOI: [10.1103/PhysRevB.95.075128](https://doi.org/10.1103/PhysRevB.95.075128)

I. INTRODUCTION

The anomalous Hall effect (AHE) [1] and spin Hall effect (SHE) [2] are very important members of the family of Hall effects. The AHE is characterized by a transverse voltage generated by a longitudinal charge current usually in a ferromagnetic (FM) metal. The AHE can be generalized to the case of the SHE in nonmagnetic materials in which Mott scattering [3] leads to the deflection of spin-up and -down charge carriers in opposite directions, owing to spin-orbit coupling (SOC), as illustrated in Fig. 1. Thus, a longitudinal charge current can generate opposite spin accumulations along opposing edges in the transverse direction to the current. On the contrary, a spin current can also induce a transverse voltage drop, in an effect called the inverse SHE. Both the AHE and SHE are of particular interest for spintronic applications [4–6], and references therein] in which spin currents can be used to manipulate magnetic moments, for example, switching the state of magnetization of magnetic nanoelements, or for inducing the very efficient motion of domain walls [7,8]. Thus, the SHE has recently attracted much attention by both experimentalists and theorists, and there has been widespread efforts to search for candidate materials that exhibit strong AHE or SHE.

The AHE and SHE originate from the electronic and magnetic structures of materials and have both extrinsic and intrinsic origins. Extrinsic contributions depend sensitively on impurity scattering while intrinsic effects are derived from properties of the band structure. It is the intrinsic AHE and SHE that are the subject of this paper. For the AHE of an ordinary collinear ferromagnet, it has been established that the Berry curvature, a quantity closely determined by the band structure, acts as a fictitious magnetic field in momentum space, that

is derived from the magnetization and SOC, and affects the charge motion in the same way as a real magnetic field [9]. In a collinear AFM, it is not surprising that the AHE vanishes due to the spin-up and -down conduction electron symmetry, or rather the existence of a symmetry by combining a time-reversal symmetry operation and a lattice translation. In a chiral ferromagnet where magnetic moments are tilted in a lattice, it was recently found that the aforementioned fictitious magnetic field can also be generated by the scalar spin chirality [10,11], $S_i(S_j \times S_k)$ ($S_{i,j,k}$ denote three noncoplanar spins), which does not necessarily involve SOC. When an electron makes a loop trajectory in a chiral FM lattice, the electron acquires a real-space Berry phase due to double exchange interactions with the chiral lattice spins. The corresponding AHE has been referred to as a so-called real-space topological Hall effect in the literature (e.g., Ref. [12]). In a chiral AFM in which the magnetic moments are coplanar, the topological Hall effect disappears because of the zero spin chirality. However, an AHE can still exist due to a nonzero Berry curvature induced by the SOC [13]. Indeed, a strong AHE was recently observed in the chiral AFM compounds Mn_3Sn and Mn_3Ge [13–16]. In principle, the SHE exists generically in systems with strong SOC. It has been studied in nonmagnetic [17–20] as well as antiferromagnetic [20–24] metals. Very recently, a strong SHE was experimentally discovered in another chiral AFM compound Mn_3Ir [25]. Therefore, chiral AFM materials are appealing candidates for finding significant AHE and SHE. They have also stimulated the search for Weyl points in the same family of materials [26] and exotic magneto-optical Kerr effect [27].

In this work, we have performed a comprehensive study of the intrinsic AHE and SHE of the compounds Mn_3X ($X = Ge, Sn, Ga, Ir, Rh, \text{ and } Pt$), using *ab initio* Berry phase calculations. These compounds exhibit a chiral AFM order well above room temperature (see Table I). This paper is organized as follows. We first introduce the *ab initio* method and the linear-response method that we have used to compute the AHE and SHE in

*yan@cpfs.mpg.de

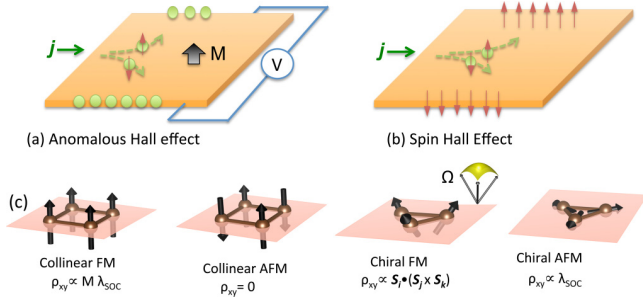


FIG. 1. Schematic illustrations of (a) the anomalous Hall effect and (b) the spin Hall effect from the viewpoint of spin-dependent Mott scattering. (c) The anomalous Hall effect in collinear FM, collinear AFM, chiral FM, and chiral AFM systems. ρ_{xy} , M , λ_{SOC} , and $S_j(S_j \times S_k)$ represent the anomalous Hall resistivity, magnetization, strength of SOC, and the scalar spin chirality, respectively.

Sec. II. We then discuss the relationship of the symmetry of the crystal lattice and magnetic lattice to the SHC and AHC in Sec. III. In Sec. IV, we discuss the results of our calculations with the assistance of symmetry analysis, where the Mn_3X compounds are classified into two groups according to their crystal and magnetic structures. Finally, we summarize our results in Sec. V.

II. METHODS

The anomalous Hall conductivity (AHC) and spin Hall conductivity (SHC) characterize the AHE and SHE, respectively. In addition, the spin lifetime and related spin manipulation methods are important ingredients for the SHE device applications, but these aspects are beyond the scope of the current study. The AHC and SHC have been calculated using the Berry phase that we have determined from *ab initio* band structures. Density-functional theory (DFT) calculations were performed for the Mn_3X bulk crystals with the Vienna *ab-initio* simulation package (VASP) [28] within the generalized gradient approximation (GGA) [29]. The SOC was included in our calculations. The material-specific Hamiltonians were established by projecting the DFT Bloch wave functions onto maximally localized Wannier functions (MLWFs) [30]. Based on these tight-binding Hamiltonians, that include realistic material parameters, we have calculated the intrinsic AHC and SHC by using the Kubo formula approach within the

TABLE I. Crystal structure, magnetic structure, and AFM ordering temperature (T_N) for Mn_3X compounds.

	T_N (K)	Crystal space group	Magnetic space group
Mn_3Ga^a	470	$P6_3/mmc$, no. 194	$R\bar{3}m'$
Mn_3Ge^b	365		
Mn_3Sn^c	420		
Mn_3Rh^d	853 ± 10	$Pm\bar{3}m$, no. 221	$Am'm'm2$
Mn_3Ir^e	960 ± 10		
Mn_3Pt^f	473 ± 10		

^aRef. [37]; ^bRef. [45]; ^cRef. [46]; ^dRef. [44]; ^eRef. [43]; ^fRefs. [42,44].

linear response [1,2,9,31]. The AHC ($\sigma_{\alpha\beta}$) is obtained from

$$\sigma_{\alpha\beta} = -\frac{e^2}{\hbar} \sum_n \int_{\text{BZ}} \frac{d^3\vec{k}}{(2\pi)^3} f_n(\vec{k}) \Omega_n(\vec{k}),$$

$$\Omega_n(\vec{k}) = 2i\hbar^2 \sum_{m \neq n} \frac{\langle u_n(\vec{k}) | \hat{v}_\alpha | u_m(\vec{k}) \rangle \langle u_m(\vec{k}) | \hat{v}_\beta | u_n(\vec{k}) \rangle}{(E_n(\vec{k}) - E_m(\vec{k}))^2}, \quad (1)$$

where $\hat{v}_{\alpha(\beta,\gamma)} = \frac{i}{\hbar} [\hat{H}, \hat{r}_{\alpha(\beta,\gamma)}]$ is the velocity operator with $\alpha, \beta, \gamma = x, y, z$; \hat{r}_α is the position operator. $f_n(\vec{k})$ is the Fermi-Dirac distribution. $|u_n(\vec{k})\rangle$ and $E_n(\vec{k})$ are the eigenvector and eigenvalue of the Hamiltonian $\hat{H}(\vec{k})$, respectively. $\Omega_n(\vec{k})$ is the Berry curvature in momentum space, and the corresponding AHC $\sigma_{\alpha\beta}$ can be evaluated by summing the Berry curvature over the Brillouin zone (BZ) for all the occupied bands. Here $\sigma_{\alpha\beta}$ corresponds to a 3×3 matrix and indicates a transverse Hall current j_α generated by a longitudinal electric field E_β , which satisfies $J_\alpha = \sigma_{\alpha\beta} E_\beta$. For the evaluation of the velocity operator we assume for simplicity that the position operator is diagonal in the Wannier basis, as is commonly done in tight-binding calculations.

The intrinsic SHC can be obtained by replacing the velocity operator with the spin current operator $\hat{J}_\alpha^\gamma = \frac{1}{2} \{ \hat{v}_\alpha, \hat{s}_\gamma \}$, where \hat{s}_γ is the spin operator. The SHC then has the form of

$$\sigma_{\alpha\beta}^\gamma = \frac{e}{\hbar} \sum_n \int_{\text{BZ}} \frac{d^3\vec{k}}{(2\pi)^3} f_n(\vec{k}) \Omega_{n,\alpha\beta}^\gamma(\vec{k}),$$

$$\Omega_{n,\alpha\beta}^\gamma(\vec{k}) = 2i\hbar^2 \sum_{m \neq n} \frac{\langle u_n(\vec{k}) | \hat{J}_\alpha^\gamma | u_m(\vec{k}) \rangle \langle u_m(\vec{k}) | \hat{v}_\beta | u_n(\vec{k}) \rangle}{(E_n(\vec{k}) - E_m(\vec{k}))^2}. \quad (2)$$

$\Omega_{n,\alpha\beta}^\gamma(\vec{k})$ is referred to as the spin Berry curvature in the following, in order to distinguish it from the Berry curvature $\bar{\Omega}_n(\vec{k})$. The SHC ($\sigma_{\alpha\beta}^\gamma$; $\alpha, \beta, \gamma = x, y, z$) is a third-order tensor ($3 \times 3 \times 3$) and represents the spin current $J s_\alpha^\gamma$ generated by an electric field \vec{E} via $J s_\alpha^\gamma = \sigma_{\alpha\beta}^\gamma E_\beta$, where $J s_\alpha^\gamma$ flows along the α direction with the spin polarization along the γ direction and E_β is the β component of the electric field \vec{E} .

For the integrals of Eqs. (1) and (2), the BZ was sampled by k grids from $50 \times 50 \times 50$ to $200 \times 200 \times 200$. Satisfactory convergence was achieved for a k grid of size $150 \times 150 \times 150$. Increasing the grid size to $200 \times 200 \times 200$ varied the SHC and AHC by no more than 5%. Note that the unit of SHC differs from that of the AHC by $\frac{\hbar}{2e}$, where $\hbar/2$ is the spin angular momentum and e is the electron charge. Thus, the unit of SHC is $(\hbar/e)(\Omega \text{ cm})^{-1}$.

Since AHC and SHC are determined directly by the band structure, they are fully compatible with the symmetry of the Hamiltonian. Therefore, we can use symmetry analysis to simplify the shape of the AHC and SHC tensor matrices, by forcing certain matrix elements to be zero and constraining some to be the same. Here, we obtain the shape of the intrinsic response tensor from the linear-response-symmetry code [32,33], which analyzes the symmetry operations of the corresponding crystal and magnetic space groups [34] and then

TABLE II. Shape of the AHC and SHC tensors obtained from symmetry analysis and numerical calculations for Mn_3X ($X = \text{Ga}, \text{Ge}, \text{and Sn}$). The calculated SHC tensor elements are set to zero when they are smaller than $12 (\hbar/e)(\Omega \text{ cm})^{-1}$. The coordinates used here are x along [100], y along [120], and z along [001], as presented in Figs. 1(a) and 1(b). The AHC is given in units of $(\Omega \text{ cm})^{-1}$ and the SHC in units of $(\hbar/e)(\Omega \text{ cm})^{-1}$.

	AHC			SHC			
	σ			$\underline{\sigma}^x$	$\underline{\sigma}^y$	$\underline{\sigma}^z$	
symmetry-imposed tensor shape	$\begin{pmatrix} 0 & 0 & -\sigma_{zx} \\ 0 & 0 & 0 \\ \sigma_{zx} & 0 & 0 \end{pmatrix}$	$\begin{pmatrix} 0 & 0 & 0 \\ 0 & 0 & \sigma_{yz}^x \\ 0 & \sigma_{zy}^x & 0 \end{pmatrix}$	$\begin{pmatrix} 0 & 0 & \sigma_{xz}^y \\ 0 & 0 & 0 \\ \sigma_{zx}^y & 0 & 0 \end{pmatrix}$	$\begin{pmatrix} 0 & \sigma_{xy}^z & 0 \\ \sigma_{yx}^z & 0 & 0 \\ 0 & 0 & 0 \end{pmatrix}$			
Mn_3Ga	$\begin{pmatrix} 0 & 0 & -81 \\ 0 & 0 & 0 \\ 81 & 0 & 0 \end{pmatrix}$	$\begin{pmatrix} 0 & 0 & 0 \\ 0 & 0 & -14 \\ 0 & 12 & 0 \end{pmatrix}$	$\begin{pmatrix} 0 & 0 & 15 \\ 0 & 0 & 0 \\ -7 & 0 & 0 \end{pmatrix}$	$\begin{pmatrix} 0 & -597 & 0 \\ 626 & 0 & 0 \\ 0 & 0 & 0 \end{pmatrix}$			
Mn_3Ge	$\begin{pmatrix} 0 & 0 & 330 \\ 0 & 0 & 0 \\ -330 & 0 & 0 \end{pmatrix}$	$\begin{pmatrix} 0 & 0 & 0 \\ 0 & 0 & -21 \\ 0 & 18 & 0 \end{pmatrix}$	$\begin{pmatrix} 0 & 0 & 21 \\ 0 & 0 & 0 \\ -18 & 0 & 0 \end{pmatrix}$	$\begin{pmatrix} 0 & 112 & 0 \\ -115 & 0 & 0 \\ 0 & 0 & 0 \end{pmatrix}$			
Mn_3Sn	$\begin{pmatrix} 0 & 0 & 133 \\ 0 & 0 & 0 \\ -133 & 0 & 0 \end{pmatrix}$	$\begin{pmatrix} 0 & 0 & 0 \\ 0 & 0 & -36 \\ 0 & 96 & 0 \end{pmatrix}$	$\begin{pmatrix} 0 & 0 & 36 \\ 0 & 0 & 0 \\ -96 & 0 & 0 \end{pmatrix}$	$\begin{pmatrix} 0 & 64 & 0 \\ -68 & 0 & 0 \\ 0 & 0 & 0 \end{pmatrix}$			

determines the tensor shape by solving the linear equations. We note that a similar study [35] also recently considered how the shape of the tensor response varied according to the magnetic Laue group. The shape of the AHC and SHC tensors is shown in Table II. These are very helpful in checking the validity and numerical convergence of our calculations by comparing the symmetry of the calculated matrices and the ideal symmetry-imposed matrices. Furthermore, the tensor shape surely relies on the coordinate system that is specified in the next section. The AHC and SHC tensors can be expressed in different coordinate systems, which are physically equivalent, and can be transformed into each other according to specific rotation matrices [36].

III. CRYSTALLOGRAPHIC AND MAGNETIC STRUCTURES

The compounds considered here can be classified into two groups according to their crystallographic structure. Mn_3Ga , Mn_3Ge , and Mn_3Sn display a hexagonal lattice with the space group $P6_3/mmc$ (No. 194). The primitive unit cell includes two Mn_3X planes that are stacked along the c axis according to “-AB-AB-”. Each structure contains a plane of Mn atoms that constitute a Kagome-type lattice with Ga, Ge, or Sn lying at the center of a hexagon formed from the Mn atoms. In the Kagome plane due to magnetogeometrical frustration, the Mn magnetic moments exhibit a noncollinear AFM order, where the neighboring moments are aligned at a 120° angle [37–39]. The energetically favored AFM configuration was revealed, as illustrated in Fig. 2(a), in earlier DFT calculations [40]. The magnetic ordering temperatures are above 365 K for all these three compounds, as shown in Table I. Additionally, Mn_3Ga and Mn_3Ge can also crystallize into a tetragonal phase with a ferrimagnetic structure [37,38,41], which is not considered in this work.

Mn_3Rh , Mn_3Ir , and Mn_3Pt crystallize in a face-centered cubic (FCC) lattice (space group $Pm\bar{3}m$, No. 221) with Ir (Rh, Pt) and Mn located at the corner and face-center sites,

respectively, as shown in Fig. 2(b). Within the (111) plane, the Mn sublattice also forms a Kagome lattice. In contrast to that of Mn_3Ge , the Kagome planes stack in an “-ABC-ABC-” sequence. The noncollinear AFM structure has also been observed by neutron diffraction measurements [42–44]. Distinct from Mn_3Ge , here the magnetic moments all point towards or away from the center of the Mn triangles. The AFM order also persists to well above room temperature (see Table I).

IV. RESULTS AND DISCUSSIONS

A. Anomalous Hall effect in Mn_3Ga , Mn_3Ge , and Mn_3Sn

The AHC $\sigma_{\alpha\beta}$ can be understood by a consideration of the symmetry of the magnetic structure. As indicated in Fig. 1(a) there is a mirror plane \hat{M}_y that is parallel to the zx plane. By combining a mirror reflection about this plane and a translation operation along the c direction $\hat{t} = (0,0,c/2)$, the system is imaged back onto itself with the same crystallographic and magnetic structures. Therefore, the magnetic structure in Mn_3Ga , Mn_3Ge , and Mn_3Sn is symmetric with respect to the $\{\hat{M}_y|\hat{t}\}$ symmetry operator. The mirror operation \hat{M}_y changes the signs of $\Omega_{yz}(\vec{k})$ and $\Omega_{xy}(\vec{k})$, but preserves $\Omega_{zx}(\vec{k})$, since $\Omega_{\alpha\beta}(\vec{k})$ is a pseudovector, just like the spin. Accordingly, σ_{yz} and σ_{xy} that are parallel to the mirror plane are transformed to $-\sigma_{yz}$ and $-\sigma_{xy}$, with respect to the \hat{M}_y reflection (the translation operation does not affect the Berry curvature). Thus, from symmetry considerations, σ_{yz} and σ_{xy} must be zero, and only σ_{zx} can be nonzero. We therefore propose that the preferred experimental setup for maximizing AHC is to confine the electric field within the zx plane, for example, by setting the electric current along z and detecting the transverse voltage along x .

Our calculations are fully consistent with the above symmetry analysis, as shown in Table II, where only σ_{zx} ($\sigma_{xz} = -\sigma_{zx}$) is nonzero. The AHC of Mn_3Ge is as large as $330 (\Omega \text{ cm})^{-1}$. Although Mn_3Sn has a stronger SOC than Mn_3Ge , its AHC

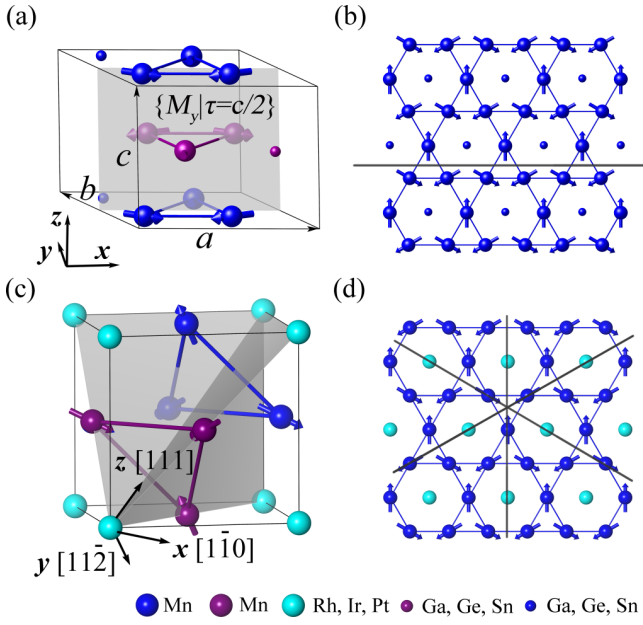


FIG. 2. Crystal lattice and magnetic structure for Mn_3X ($X = Ga, Ge, Sn, Rh, Ir, \text{ and } Pt$). (a) Mn_3X ($X = Ga, Ge, \text{ and } Sn$) display a hexagon lattice with Mn forming a Kagome sublattice stacking along the c axis. The gray plane indicates the M_y mirror plane of the symmetry operation $\{M_y|\tau=c/2\}$. The crystallographic a and c axes align with the x and z directions, respectively, with the b axis lying inside the xy plane. (b) Top view of the Mn Kagome-type lattice showing triangular and hexagonal arrangements of the Mn moments. Arrows represent the Mn magnetic moments, presenting a noncollinear AFM configuration. The mirror plane position is indicated by a black line. (c) The crystal structure of Mn_3X ($X = Rh, Ir, \text{ and } Pt$) has an FCC lattice. Three mirror planes are shown in gray. Here a mirror reflection combined with a time-reversal symmetry operation preserves the magnetic lattice. (d) The Mn sublattice also forms a Kagome-type configuration in Mn_3X ($X = Rh, Ir, \text{ and } Pt$), thereby forming a noncollinear AFM phase, but which is slightly different from the Mn_3Ge family. The projections of three mirror planes are indicated by black lines. To match the hexagonal lattice conveniently, the Kagome plane is set as the xy plane and the plane normal as the z axis. Here x is along the crystallographic $[1\bar{1}0]$, y along $[11\bar{2}]$, and z along $[111]$.

is less than half that of Mn_3Ge . Mn_3Ga exhibits the smallest AHC and, moreover, the AHC has the opposite sign to those of the Ge and Sn compounds. This is fully consistent with recent experiments on the Ge and Sn compounds [15,16], where the in-plane AHC (σ_{xy}) is negligible compared to the out-of-plane AHC (σ_{zx} and σ_{yz}), and Mn_3Sn displays a smaller AHC in magnitude than Mn_3Ge . We note that σ_{zx} and σ_{yz} may be both nonzero if a different coordinate axis is chosen or the chiral moments are rotated by an external magnetic field.

Since the intrinsic AHE originates from the electronic band structure, we analyzed the band structure in detail to understand the differences among these three compounds. Their calculated band structures are shown in Fig. 3. Since the valence electrons for Ga and Ge (Sn) are $4s^24p^1$ and $4s^24p^2$ ($5s^25p^2$), respectively, the band structure of Mn_3Ga looks very similar to that of Mn_3Ge (Mn_3Sn). The Fermi level is shifted up by 0.34 eV (equivalent to adding one electron).

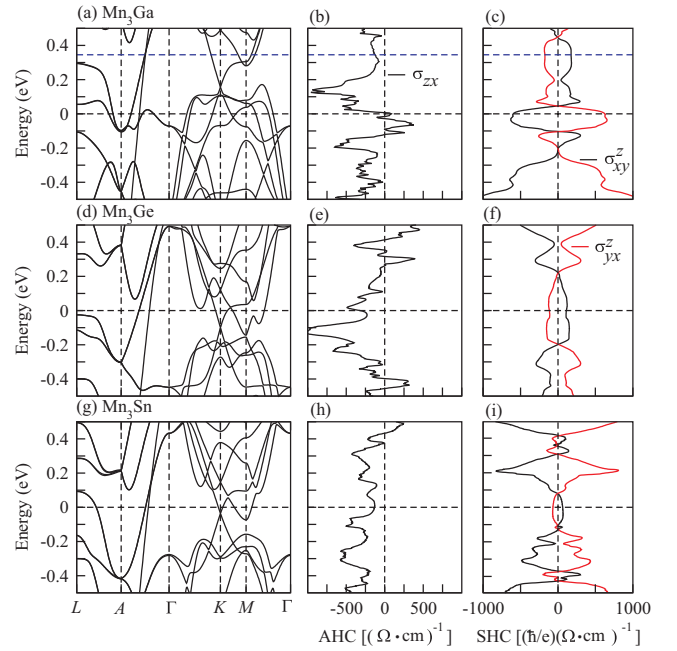


FIG. 3. Electronic band structure for (a) Mn_3Ga , (d) Mn_3Ge , and (g) Mn_3Sn . Energy dependent AHC σ_{zx} for (b) Mn_3Ga , (e) Mn_3Ge , and (h) Mn_3Sn . Energy dependent SHC tensor elements of σ_{yx}^z and σ_{zx}^z for (c) Mn_3Ga , (f) Mn_3Ge , and (i) Mn_3Sn . Mn_3Ga would have the same number of valence electrons as does Mn_3Ge and Mn_3Sn if the Fermi level is shifted up to the blue dashed line in (a)–(c).

Correspondingly, the shapes of the energy-dependent AHC curves for Mn_3Ga and Mn_3Ge (Mn_3Sn) are also very similar. The value of σ_{zx} in Mn_3Ga changes sign from negative to positive after tuning up the Fermi level.

Atomic Ge and Sn have similar valence electron configurations while Sn has a larger atomic radius and stronger SOC compared to Ge. Although the consequent changes in the band structures are subtle (see Fig. 3), the effect on the resultant AHC can be significant. To better understand the AHE in Mn_3Ge and Mn_3Sn , we considered the distributions of the Berry curvature in the reciprocal space. We have projected the Berry curvature components of Ω_{zx} onto the k_3 - k_1 (k_z - k_x) plane by integrating them along k_2 , where $k_{1,2,3}$ are the reciprocal lattice vectors, and k_3 and k_1 are aligned with the k_z and k_x axes, respectively. The projected Berry curvatures of Mn_3Ge and Mn_3Sn with the Fermi level lying at the charge neutral point are shown in Figs. 4(a) and 4(b), respectively. One can easily identify the origin of the significant differences of the Berry curvature between Mn_3Ge and Mn_3Sn . The large AHC mainly arises from the positive *hot spots* located around (0.127, 0.428) (the coordinates are in units of the reciprocal lattice vectors k_1 and k_2) and its three partners in the k_3 - k_1 plane, while these four hot spots are not seen in Mn_3Sn . Taking the hotspot at (0.127, 0.428) as an example, we have checked the band structure and corresponding Berry curvature evolution with k_2 varying from 0 to 1. From the band structure of Mn_3Ge in Fig. 4(c) we can see that the Fermi level crosses two small gaps around $k_2 = 0$ and 0.5. According to Eq. (1), the entanglement between occupied and unoccupied states must be very strong around these two points and contributes to a large

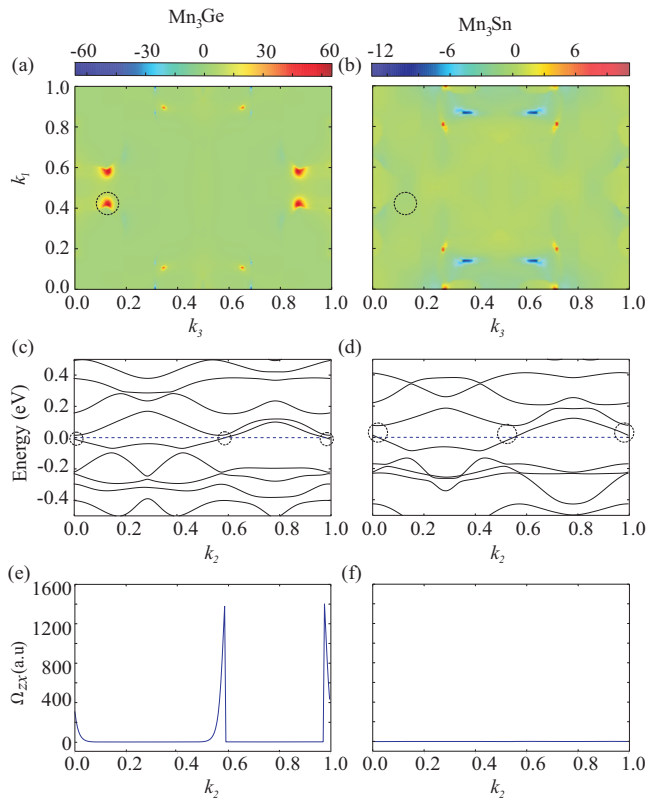


FIG. 4. (a),(b) Berry curvature projected onto the k_3 - k_1 plane for Mn_3Ge and Mn_3Sn , respectively. The Berry curvature in Mn_3Ge is dominated by the four areas that are highlighted in yellow in (a). (c) Energy dispersion of Mn_3Ge along k_2 with (k_3, k_1) fixed at the Berry curvature dominated point $(0.127, 0.428)$, identified as the black dashed circle marked in (a). The band gaps are very small near $k_2 = 0.5$ and 1 , which are noted by the small black dashed circles. (d) Band structure of Mn_3Sn for the same reciprocal space cut as in (c). The band gaps are much larger in Mn_3Sn , as denoted by the larger black dashed circles. (e) The evolution of the Berry curvature Ω^y of Mn_3Ge corresponding to the band structure given in (c). The small band gaps around $k_2 = 0.5$ and 1 make larger contributions to the Berry curvature. (f) The magnitude of Berry curvature along the same path in Mn_3Sn is negligibly small compared to that in Mn_3Ge .

Berry curvature, as indicated by the two peaks in Fig. 4(e). This is fully consistent with previous calculations on Mn_3Ge [16]. Mn_3Sn has a similar band structure along the same k path, as can be seen by comparing Figs. 4(c) and 4(d), whereas the band gaps around $k_2 = 0$ and 0.5 are much larger compared to that in Mn_3Ge . Consequently, the two Berry curvature peaks disappear in Mn_3Sn , as shown in Fig. 4(f). Thus, a tiny change in band structure can result in significant changes in the Berry curvature and AHC in this class of compounds.

B. Spin Hall effect in Mn_3Ga , Mn_3Ge , and Mn_3Sn

By adding the spin degree of freedom, the SHC becomes a third-order tensor. Similar to the AHC, some SHC tensor elements will be exactly zero or will be identical based on the corresponding lattice and magnetic symmetries. The magnetic space group for Mn_3X ($X = \text{Ga}, \text{Ge}, \text{and Sn}$) is identified to be $R\bar{3}m'$, and the corresponding Laue group is $m'm'm'$ [34]. The

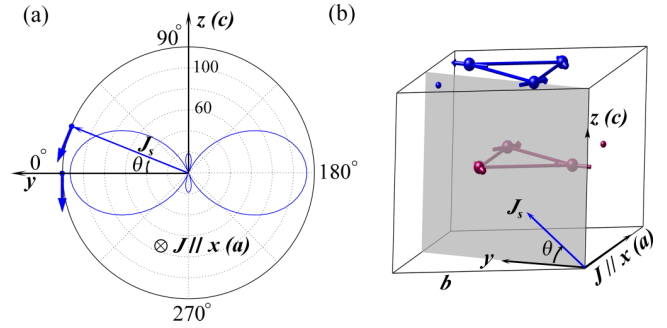


FIG. 5. (a) Angle-dependent spin current J_s arising from a charge current J along the x axis (the crystallographic a lattice vector) in Mn_3Ge . J_s rotates inside the yz plane. The largest spin Hall conductivity is when J_s is along the y axis ($\theta = 0^\circ$). The blue arrows represent the spin polarization directions of J_s . (b) Schematic of J_s and J with respect to the lattice orientation.

calculated shape of the intrinsic SHC tensor and corresponding numerical results are presented in Table II. Furthermore, the SHC of Mn_3X ($X = \text{Ga}, \text{Ge}$ and Sn) is strongly anisotropic with dominant components of σ_{xy}^z and σ_{yx}^z . These results will provide helpful information for the experimental detection of the SHE. To illustrate the anisotropy of the SHC, we show the angle-dependent SHC for Mn_3Ge in Fig. 5. When the charge current J is fixed along the x axis (a direction) and by considering the spin current J_s perpendicular to J and rotating it, the corresponding magnitude of SHC is maximal for $J_s \parallel y$ while being zero for $J_s \parallel z$. Therefore, to observe large SHC, one should set the charge current and spin current inside the Kagome (xy) plane, for example with the electron current set along x and by measuring the transverse spin current along y with its spin polarization along z . Therefore, we stress that for optimizing the efficiency of devices that rely on SHE and AHE, the direction of the charge current and the resulting spin current will depend on the respective compound.

As shown in Table II, the largest SHCs σ_{xy}^z and σ_{yx}^z are of the order of $120 (\hbar/e)(\Omega \text{ cm})^{-1}$ in magnitude for Mn_3Ge . With the relatively small electrical conductivity [about $3300 (\Omega \text{ cm})^{-1}$], we would have a spin Hall angle up to 3%. Also the σ_{yx}^z elements in Mn_3Ga is around $600 (\hbar/e)(\Omega \text{ cm})^{-1}$. Additionally, it is not surprising that σ_{xy}^z and σ_{yx}^z are not equal in magnitude, for the x and y directions are not equivalent in a Kagome structure.

Since the SHC is strongly related to the location of the Fermi level, the SHC varies quickly as the Fermi energy is shifted, especially for the metallic band structures shown in Fig. 3. The energy-dependent SHC of the most prominent tensor elements σ_{xy}^z and σ_{yx}^z for the three compounds are shown in Figs. 3(e), 3(f), and 3(i). Owing to the similar crystal lattice constant and the same magnetic order, the shapes of the SHC curves are very similar, if we ignore the fact that Ga has one electron less than either Ge or Sn. For Mn_3Ga , the SHC exhibits a minimum at the Fermi level, the charge neutral point, and increases quickly if the Fermi level moves up or down. Hence an even larger SHC is expected for Mn_3Ga with small electron or hole doping. One can see that the SHC remains relatively stable with respect to varying the Fermi level in the energy window of ± 0.1 eV for Mn_3Ge and Mn_3Sn . This indicates that the SHC in the Ge and Sn compounds is robust.

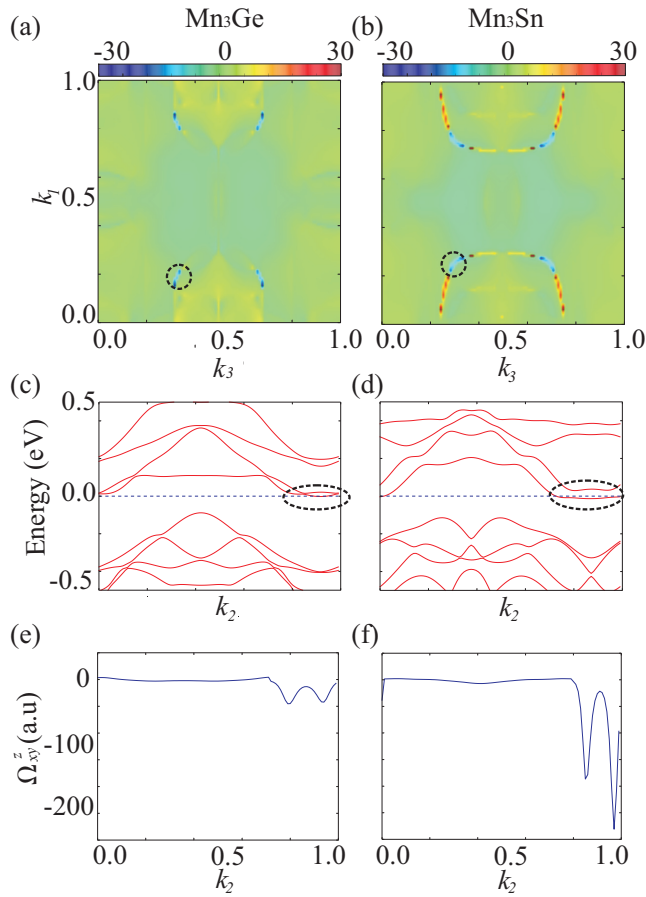


FIG. 6. (a),(b) Spin Berry curvature projected onto the k_3 - k_1 plane for Mn₃Ge and Mn₃Sn, respectively. The two compounds have similar distributions of the projected spin Berry curvature. (c),(d) Band structures of Mn₃Ge and Mn₃Sn, respectively, along k_2 . The coordinates of k_3 and k_1 are fixed at (0.31, 0.15) and (0.29, 0.24) for Mn₃Ge and Mn₃Sn, respectively, as noted by the black dashed circles in (a) and (b). Small band gaps exist around the $k_2 = 1$ point for both Mn₃Ge and Mn₃Sn, as marked by the black dashed circles. (e),(f) Corresponding spin Berry curvature evolutions along k_2 for Mn₃Ge and Mn₃Sn, respectively. The large spin Berry curvature mainly originates from the small band gaps in the band structures.

Since the spin Berry curvature is distinct from the Berry curvature, the SHC and AHC can have dominant contributions from different electronic bands. Although Mn₃Ge and Mn₃Sn display very different AHCs in magnitude, their SHCs are very close. Therefore, we expect a similar spin Berry curvature distribution in k space for both compounds. Taking the components of Ω_{xy}^z as an example, we compare the spin Berry curvature distributions for Mn₃Ge and Mn₃Sn with the Fermi energy lying at the charge neutral point. Similar to the above analysis for the AHE, we also project the spin Berry curvature onto the k_3 - k_1 plane by integrating Ω_{xy}^z along k_2 . As shown in Fig. 6, Mn₃Ge and Mn₃Sn display similar features in their respective spin Berry curvature distributions. The shapes of the dominant areas are very similar in both compounds, with just a little shift within the k_3 - k_1 plane. The dominant contribution forms thick arcs with a transition point between positive and negative amplitudes, where the integrated spin Berry curvature

transfers from positive to negative. Since the size of the positive dominant area is much larger than that of the negative part, the integral of the spin Berry curvature in the whole BZ gives a positive SHC σ_{xy}^z , as is listed in Table II.

The above positive-negative spin Berry curvature distribution is reminiscent of the similar feature of the SHE around the Weyl point, where positive and negative spin Berry curvature appear with the Weyl point as the transition point [26]. In fact Weyl points also exist in Mn₃Ge and Mn₃Sn, however, the spin Berry curvature transition point in Fig. 6 does not exactly overlap with the Weyl point. A careful inspection of the band dispersions along k_2 through these hot spots reveals tiny band gaps that contribute to the peaks of the spin Berry curvature, as shown in Figs. 6(e) and 6(f). Therefore, the intrinsic SHC mainly arises from the small band gaps lying very close to the Fermi level.

C. Anomalous Hall effect and spin Hall effect in Mn₃Rh, Mn₃Ir, and Mn₃Pt

In the cubic lattice of Mn₃Rh, Mn₃Ir, and Mn₃Pt, there are three mirror planes that intersect the crystallographic [111] axis and which are related to each other by a threefold rotation. The mirror reflection \hat{M} preserves the lattice symmetry but reverses all spins in the Kagome plane. Since time-reversal symmetry \hat{T} can also reverse spins, the combined symmetry of time-reversal and mirror symmetry, $\hat{T}\hat{M}$ is the symmetry of the system. $\hat{T}\hat{M}$ forces the out-of-mirror-plane AHC components to be zero, since the out-of-plane Berry curvature is odd with respect to \hat{T} but even with respect to \hat{M} . Given the existence of the three mirror planes, the only nonzero AHC component is along the co-axis of these three planes, i.e. the [111] axis. For the convenience of the symmetry analysis, we used coordinates with z along the [111] direction and x, y within the Kagome plane (see Fig. 1).

Our numerical calculations are again consistent with the symmetry analysis. The AHC for Mn₃Ir can reach $\sigma_{xy} = 312(\Omega \text{ cm})^{-1}$ with the electric field lying in the (111) plane, as presented in Table III, which agrees with previous calculations [13]. Compared to Mn₃Ir, Mn₃Rh exhibits similar AHC in magnitude while Mn₃Pt shows a much smaller AHC. Mn₃Rh and Mn₃Ir show very similar trends in the Fermi-energy-dependent AHC, as shown in Figs. 7(b) and 7(e). The peak values appear around 50 meV above the charge neutral point for both Mn₃Rh and Mn₃Ir. Therefore, in order to get strong AHE, one simply needs weak electron doping, and the AHC in the (111) plane can then reach 450 and 500 $(\Omega \text{ cm})^{-1}$ for Mn₃Rh and Mn₃Ir, respectively. Compared to Rh and Ir, Pt has one more valence electron. Hence the Mn₃Pt can be viewed as a strongly doped version of Mn₃Ir, which shifts the Fermi level a little further beyond the peak values, leading to a small AHC of $98(\Omega \text{ cm})^{-1}$, as shown in Fig. 7(h).

The magnetic space group for Rh, Ir, and Pt compounds is $Am'm'm2$, from which we can obtain the symmetry of the SHC tensor. As shown in Table III, there are only four independent nonzero elements. Our numerical calculations fit the symmetry-imposed tensor shape very well, as shown in Table III. The largest SHC tensor elements are σ_{yz}^x ($\sigma_{xz}^y = \sigma_{yz}^x$) and σ_{xy}^y ($\sigma_{xy}^y = \sigma_{yx}^y = -\sigma_{xx}^x = \sigma_{yy}^y$) for Mn₃Rh and Mn₃Ir. Therefore, the optimal experimental arrangement for large

TABLE IV. Summary of the optimal experimental arrangements to realize large AHE and SHE. The xy plane refers to the Kagome AFM plane and the z direction is perpendicular to this plane. For AHE, the preferred plane to set the current and detect the Hall voltage is specified. For SHE, the charge current J and spin current J_s directions, which are supposed to be orthogonal, are indicated.

	AHE	SHE
Mn ₃ Ga	xz plane	xy plane
Mn ₃ Ge		
Mn ₃ Sn		
Mn ₃ Rh	xy plane	J_s inside the xy plane
Mn ₃ Ir		
Mn ₃ Pt		

V. SUMMARY

In summary, we have studied the intrinsic AHE and SHE in the noncollinear AFM compounds Mn₃X ($X = \text{Ge, Sn, Ga, Rh, Ir, and Pt}$) by *ab initio* calculations. Large AHC and large SHC are found for these materials, which are also

highly anisotropic and in agreement with recent experimental measurements. Such an anisotropy is closely related to the symmetry of the AFM Kagome lattice, which can be helpful in rationalizing the numerical results. Based on our calculations, we have proposed the optimal experimental setups to maximize the AHE and SHE for different systems, as shown in Table IV. Although the SOC magnitude increases from Rh, to Ir, and to Pt, the magnitude of the corresponding AHC and SHC do not follow the same trend. This is also true for the Ga, Ge, and Sn compounds. This indicates that the electron filling and the detailed band structures are essential in determining the magnitude of the AHE and SHE. We point out that the largest SHC attains a value of around $600 (\hbar/e)(\Omega \text{ cm})^{-1}$ in Mn₃Ga. Our work provides insights in the interpretation and realization of a strong AHE and SHE in chiral AFM materials.

ACKNOWLEDGMENTS

We thank Jario Sinova, Jereon van den Brink, and Carsten Timm for helpful discussions. C.F. acknowledges the funding support by ERC (Advanced Grant No. 291472 “Idea Heusler”). Y.Z. and B.Y. acknowledge the German Research Foundation (DFG) SFB 1143.

-
- [1] N. Nagaosa, J. Sinova, S. Onoda, A. H. MacDonald, and N. P. Ong, *Rev. Mod. Phys.* **82**, 1539 (2010).
- [2] J. Sinova, S. O. Valenzuela, J. Wunderlich, C. H. Back, and T. Jungwirth, *Rev. Mod. Phys.* **87**, 1213 (2015).
- [3] M. Dyakonov and V. Perel, *Phys. Lett. A* **35**, 459 (1971).
- [4] T. Jungwirth, J. Wunderlich, and K. Olejník, *Nat. Mater.* **11**, 382 (2012).
- [5] S. Maekawa, S. O. Valenzuela, E. Saitoh, and T. Kimura, *Spin Current* (Oxford University Press, Oxford, 2012), Vol. 17.
- [6] A. Hoffmann, *IEEE Trans. Magn.* **49**, 5172 (2013).
- [7] S. Parkin and S.-H. Yang, *Nat. Nanotechnol.* **10**, 195 (2015).
- [8] S.-H. Yang, K.-S. Ryu, and S. Parkin, *Nat. Nanotechnol.* **10**, 221 (2015).
- [9] D. Xiao, M.-C. Chang, and Q. Niu, *Rev. Mod. Phys.* **82**, 1959 (2010).
- [10] K. Ohgushi, S. Murakami, and N. Nagaosa, *Phys. Rev. B* **62**, R6065(R) (2000).
- [11] Y. Taguchi, Y. Oohara, H. Yoshizawa, N. Nagaosa, and Y. Tokura, *Science* **291**, 2573 (2001).
- [12] A. Neubauer, C. Pfleiderer, B. Binz, A. Rosch, R. Ritz, P. G. Niklowitz, and P. Böni, *Phys. Rev. Lett.* **102**, 186602 (2009).
- [13] H. Chen, Q. Niu, and A. H. MacDonald, *Phys. Rev. Lett.* **112**, 017205 (2014).
- [14] J. Kübler and C. Felser, *Europhys. Lett.* **108**, 67001 (2014).
- [15] S. Nakatsuji, N. Kiyohara, and T. Higo, *Nature (London)* **527**, 212 (2015).
- [16] A. K. Nayak, J. E. Fischer, Y. Sun, B. Yan, J. Karel, A. C. Komarek, C. Shekhar, N. Kumar, W. Schnelle, J. Kuebler, C. Felser, and S. S. P. Parkin, *Sci. Adv.* **2**, e1501870 (2016).
- [17] G. Y. Guo, S. Murakami, T.-W. Chen, and N. Nagaosa, *Phys. Rev. Lett.* **100**, 096401 (2008).
- [18] T. Tanaka, H. Kontani, M. Naito, T. Naito, D. S. Hirashima, K. Yamada, and J. Inoue, *Phys. Rev. B* **77**, 165117 (2008).
- [19] F. Freimuth, S. Blügel, and Y. Mokrousov, *Phys. Rev. Lett.* **105**, 246602 (2010).
- [20] B. Zimmermann, K. Chadova, D. Kodderitzsch, S. Blügel, H. Ebert, D. V. Fedorov, N. H. Long, P. Mavropoulos, I. Mertig, Y. Mokrousov, and M. Gradhand, *Phys. Rev. B* **90**, 220403 (2014).
- [21] S. Fukami, C. Zhang, S. DuttaGupta, A. Kurenkov, and H. Ohno, *Nat. Mater.* **15**, 535 (2016).
- [22] Y.-W. Oh, S.-h. C. Baek, Y. M. Kim, H. Y. Lee, K.-D. Lee, C.-G. Yang, E.-S. Park, K.-S. Lee, K.-W. Kim, G. Go *et al.*, *Nat. Nanotechnol.* **11**, 878 (2016).
- [23] V. Tshitoyan, C. Ciccarelli, A. P. Mihai, M. Ali, A. C. Irvine, T. A. Moore, T. Jungwirth, and A. J. Ferguson, *Phys. Rev. B* **92**, 214406 (2015).
- [24] W. Zhang, M. B. Jungfleisch, W. Jiang, J. E. Pearson, A. Hoffmann, F. Freimuth, and Y. Mokrousov, *Phys. Rev. Lett.* **113**, 196602 (2014).
- [25] W. Zhang, W. Han, S. H. Yang, Y. Sun, Y. Zhang, B. Yan, and S. Parkin, *Sci. Adv.* **2**, e1600759 (2016).
- [26] H. Yang, Y. Sun, Y. Zhang, W.-J. Shi, S. S. P. Parkin, and B. Yan, *New J. Phys.* **19**, 015008 (2017).
- [27] W. Feng, G.-Y. Guo, J. Zhou, Y. Yao, and Q. Niu, *Phys. Rev. B* **92**, 144426 (2015).
- [28] G. Kresse and J. Furthmüller, *Phys. Rev. B* **54**, 11169 (1996).
- [29] J. P. Perdew, K. Burke, and M. Ernzerhof, *Phys. Rev. Lett.* **77**, 3865 (1996).
- [30] A. A. Mostofi, J. R. Yates, Y.-S. Lee, I. Souza, D. Vanderbilt, and N. Marzari, *Comput. Phys. Commun.* **178**, 685 (2008).
- [31] M. Gradhand, D. Fedorov, F. Pientka, P. Zahn, I. Mertig, and B. L. Györfy, *J. Phys.: Condens. Matter* **24**, 213202 (2012).
- [32] J. Železný, H. Gao, A. Manchon, F. Freimuth, Y. Mokrousov, J. Zemen, J. Mašek, J. Sinova, and T. Jungwirth, *Phys. Rev. B* **95**, 014403 (2017).

- [33] <https://bitbucket.org/zeleznyj/linear-response-symmetry>.
- [34] ISOTROPY Software Suite, iso.byu.edu.
- [35] M. Seemann, D. Ködderitzsch, S. Wimmer, and H. Ebert, *Phys. Rev. B* **92**, 155138 (2015).
- [36] W. H. Kleiner, *Phys. Rev.* **142**, 318 (1966).
- [37] E. Krén and G. Kádár, *Solid State Commun.* **8**, 1653 (1970).
- [38] G. Kádár and E. Krén, *Int. J. Magn.* **1**, 143 (1971).
- [39] T. Ohoyama, K. Yasukōchi, and K. Kanematsu, *J. Phys. Soc. Jpn.* **16**, 352 (1961).
- [40] D. Zhang, B. Yan, S.-C. Wu, J. Kübler, G. Kreiner, S. S. Parkin, and C. Felser, *J. Phys.: Condens. Matter* **25**, 206006 (2013).
- [41] B. Balke, G. H. Fecher, J. Winterlik, and C. Felser, *Appl. Phys. Lett.* **90**, 152504 (2007).
- [42] E. Krén, G. Kádár, L. Pál, J. Sólyom, P. Szabó, and T. Tarnóczy, *Phys. Rev.* **171**, 574 (1968).
- [43] I. Tomeno, H. N. Fuke, H. Iwasaki, M. Sahashi, and Y. Tsunoda, *J. Appl. Phys.* **86**, 3853 (1999).
- [44] E. Krén, G. Kádár, L. Pál, J. Sólyom, and P. Szabó, *Phys. Lett.* **20**, 331 (1966).
- [45] N. Yamada, H. Sakai, H. Mori, and T. Ohoyama, *Physica B+C* **149**, 311 (1988).
- [46] J. Sticht, K. Höck, and J. Kübler, *J. Phys.: Condens. Matter* **1**, 8155 (1989).

5.4 Paper III: Prediction of triple point fermions in simple half-Heusler topological insulators

This work was motivated by the discovery of triple point topological metals in the hexagonal materials by Zhu [84] and Bradlyn [77]. When we analyzed the ARPES measurements of the cubic half-Heusler compound GdPtBi, we noticed several surface states near its Fermi level featured like Fermi arcs. It was reported that the AFM ordered GdPtBi has a tiny gap and is a topological insulator [94, 95] under the Neel temperature (around 9K)[96, 97]. However, at room temperature GdPtBi is paramagnetic and metallic. Those special surface states are not ordinary but indicate the existence of a metallic topological phase. By analyzing the crystal symmetry, we proposed that GdPtBi could host the triple points Fermions (TPFs). This was soon verified by our *ab-initio* and Kane–Model calculations. Apart from this material, we have searched more than thirty kinds of Half-Heusler compounds and found six of them to be the candidates holding the TPFs as shown in TABLE I in **Paper III**.

Comparing with the hexagonal WC-type material, which has only one C_{3v} rotation axis to hold the TPFs, the half-Heusler compound has four C_{3v} rotation axes. Moreover, the natural cleavable surface in the hexagonal structure material is usually a facet that is perpendicular to the C_{3v} axis. This results in the projection of all the TPFs to the Γ point of the 2-dimensional BZ and makes it unable to observe Fermi arcs. Shortly after our work, Lv [80] reported that they observed the TPFs in MoP, but unable to find topological surface states both in the (001) and (100) surfaces. They speculated that the surface states in (100) surface are disrupted by the rather disordered surface atoms. This problem can be overcome here because three of the four C_{3v} axes in the half-Heusler compound will project linearly on the cleavable surface and separate the TPFs. Thus the half-Heusler compound can be a better platform to study the surface states of TPFs.

Prediction of Triple Point Fermions in Simple Half-Heusler Topological Insulators

Hao Yang,¹ Jiabin Yu,² Stuart S. P. Parkin,¹ Claudia Felser,³ Chao-Xing Liu,² and Binghai Yan^{4,*}

¹Max Planck Institute of Microstructure Physics, Weinberg 2, 06120 Halle, Germany

²Department of Physics, Pennsylvania State University, University Park, Pennsylvania 16802, USA

³Max Planck Institute for Chemical Physics of Solids, 01187 Dresden, Germany

⁴Department of Condensed Matter Physics, Weizmann Institute of Science, Rehovot 7610001, Israel

(Received 30 May 2017; published 28 September 2017)

We predict the existence of triple point fermions in the band structure of several half-Heusler topological insulators by *ab initio* calculations and the Kane model. We find that many half-Heusler compounds exhibit multiple triple points along four independent C_3 axes, through which the doubly degenerate conduction bands and the nondegenerate valence band cross each other linearly nearby the Fermi energy. When projected from the bulk to the (111) surface, most of these triple points are located far away from the surface $\bar{\Gamma}$ point, as distinct from previously reported triple point fermion candidates. These isolated triple points give rise to Fermi arcs on the surface, that can be readily detected by photoemission spectroscopy or scanning tunneling spectroscopy.

DOI: 10.1103/PhysRevLett.119.136401

The discovery of topological insulators (TIs) [1,2] has generated much interest in the search for other novel topological states in condensed matter physics and materials science. As quasiparticle analogs of elementary particles of the standard model, Dirac fermions [3–6] and Weyl fermions [7–14] have recently been found in several materials (see reviews Refs. [15,16]). More recently, several exotic types of fermions, which do not have elementary particle counterparts, have been theoretically predicted as quasiparticle excitations near certain band crossing points that are protected by specific space-group symmetries [17,18]. In particular, triple point (TP) fermions have been predicted in many materials with triply degenerate band crossing points [19–25]. These predictions have stimulated intensive experimental studies to search for their signatures, for example, using angle-resolved photoemission spectroscopy (ARPES) [26] and transport properties [27].

TJs can be viewed as an intermediate phase between fourfold degenerate Dirac points and twofold degenerate Weyl points. They also give rise to Fermi arcs when projected onto certain specific crystal facets. However, the detection of TP-induced Fermi arcs remains challenging from the material point of view. A pair of TJs are protected by the C_{3v} symmetry group (generated by a C_3 rotation and a σ_v mirror operation) in certain compounds [19–24], for example, tensile-strained mercury telluride (HgTe) [19], molybdenum phosphide (MoP) [20], and antiferromagnetic (AFM) half-Heusler compounds (e.g., GdPtBi) [24]. Even presuming that samples can be grown, the natural cleavable surface is usually the facet that is perpendicular to the C_{3v} axis. Consequently, two TJs at the unique C_{3v} axis are projected to the same $\bar{\Gamma}$ point of the surface Brillouin zone (BZ), resulting in the disappearance of Fermi arcs, as shown in a recent ARPES measurement on MoP [26]. Therefore, TP materials with easily measurable Fermi arcs are still required for the final experimental verification of TP fermions.

In this work, we predict the existence of multiple TJs in several half-Heusler compounds in which the detection of Fermi arcs by ARPES and other surface sensitive techniques such as scanning tunneling spectroscopy should be straightforward. The face-centered-cubic lattice of half-Heusler compounds has four equivalent C_{3v} axes (e.g., the [111] axis) and, thus, can host four (or multiples of four) pairs of TJs. When projected onto the (111) surface, an easily cleavable plane [28,29], TJs at the [111] axes merge into the surface $\bar{\Gamma}$ point while the other three (or a multiple of three) pairs of TJs appear away from $\bar{\Gamma}$, leading to Fermi arcs that link these individual TJs on the surface. Combining *ab initio* band structure calculations and the $k \cdot p$ Kane model, we predict several TP candidate half-Heusler materials, including, for example, YPtBi, LuPtBi, and GdPtBi (the paramagnetic phase). The TJs and resultant extended Fermi arcs are revealed in our calculations, and await experimental proof.

Ternary half-Heusler compounds have been extensively studied in the search for TJs [28–34] and Weyl semimetals [35–38]. The band structure of Heusler TJs has been identified as being topologically identical to HgTe [39]. For example, the conduction and valence bands touch each other at the Γ point, where the wave functions are comprised mainly of p orbitals and are, therefore, named Γ_8 bands, as shown in Fig. 1(a). The fourfold degeneracy at the Γ point is protected by time-reversal symmetry (TRS) and T_d group symmetry. The s -type Γ_6 bands located below Γ_8 , thus give rise to an inverted band structure. Along each C_{3v} axis (e.g., the [111] direction), Γ_8 bands split into one doubly degenerate band (labeled as Λ_6 according to the C_{3v} symmetry) and two nondegenerate bands (labeled as $\Lambda_{4,5}$) due to the absence of inversion symmetry in the T_d group. The Λ_6 bands cross the $\Lambda_{4,5}$ bands since Λ_6 and $\Lambda_{4,5}$ bands disperse oppositely for large k [see Fig. 1(a)]. As already pointed out in Ref. [19], TJs exist at the crossing point

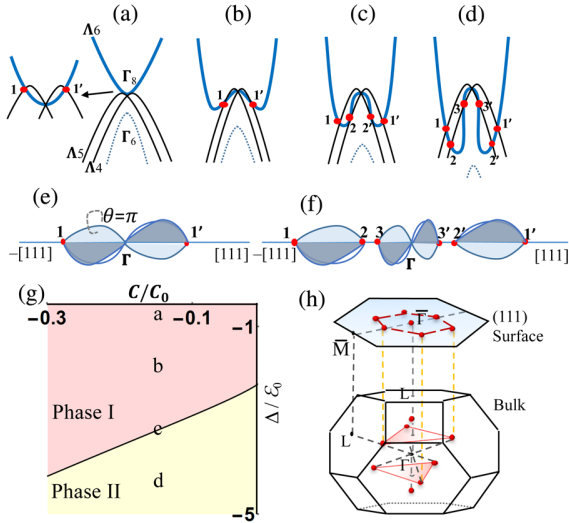


FIG. 1. Evolution of band structures with increasing numbers of triple points (TPs). (a) HgTe-type band structure along the line $L-\Gamma-L$. The Γ_8 bands (solid curves) lie above Γ_6 (dotted curves). The Γ_8 bands split into doubly degenerate Λ_6 (thick solid blue curve) and nondegenerate Λ_4 and Λ_5 bands (thin solid black curves) along the C_3 axis ($\Gamma-L$). Here Λ_6 crosses $\Lambda_{4,5}$, forming TPs (filled red circles) very close to the Γ point, where No. 1 and No. 1' represent a TP and its time-reversal partner, respectively. (b) Heusler-type band structure. The Λ_6 bands exhibit a double valley shape, pushing a pair of TPs out from the Γ point. (c), (d) Heusler-type band structure with two and three pairs of TPs along one C_{3v} axis, respectively. (e) Corresponding to the band structures in (a) and (b), three nodal lines (blue curves) inside the C_{3v} mirror planes connect a pair of TPs (1 and 1') along the C_3 axis by passing the Γ point. (f) Corresponding to the band structure in (d), the nodal lines connects these three pairs of TPs. (g) Phase diagram of TPs with respect to the band inversion strength Δ/ϵ_0 and the linear splitting term C/C_0 of $\Lambda_{4,5}$. Within the phase diagram, (a)–(d) correspond to the band structures of (a)–(d), respectively. (h) Distribution of TPs in the bulk Brillouin zone and their projection onto the (111) surface. The surface Fermi arcs that connect different TPs are illustrated by red dashed lines.

between Λ_6 and Λ_4 (or Λ_5) bands. Unfortunately, the TPs that are located extremely close to the Γ point ($\sim 0.8\%$ of the $\Gamma-L$ distance) [19] cannot be resolved by currently available techniques. In contrast, TPs in some Heusler materials can be pushed to very large momenta, because their Λ_6 bands exhibit a peculiar double-valley feature that is absent in HgTe [e.g., see Fig. 1(b)]. As illustrated in Fig. 1(b), a pair of TPs may exist near the Γ point along the C_3 axis ($\Gamma-L$), where two TPs are related by TRS and protected by C_3 rotational symmetry. Given four C_3 axes, four pairs of TPs form inside the first bulk BZ. When projected onto the (111) surface, three pairs are isolated from each other and are far from the surface $\bar{\Gamma}$ point, giving rise to Fermi arcs connecting these six TPs [Fig. 1(h)].

We first construct a phase diagram to reveal the emergence and properties of TPs in half-Heusler compounds based on the Kane model [40], in order to guide the

material search. The crystal symmetry of Half-Heusler materials is described by the space group $F\bar{4}3m$ and the point group T_d [41], respectively, and the corresponding low energy physics can be described by the six-band Kane model with two Γ_6 bands and four Γ_8 bands. Along any of the four C_3 axes, two Γ_6 bands are still degenerate, labeled as Λ_6^- bands, according to the irreducible representations of C_{3v} spin double group, while four Γ_8 bands are split into one doubly degenerate band, denoted as Λ_6^+ bands, and two nondegenerate bands, denoted as Λ_4 and Λ_5 bands, respectively. For the momentum close to Γ along the C_3 axis, the Λ_6^+ bands disperse quadratically while the $\Lambda_{4,5}$ bands disperse linearly with opposite velocities for two branches due to the linear C term in the Kane Hamiltonian. Thus, the Λ_6^+ bands must locate between two $\Lambda_{4,5}$ bands for small momenta. For larger momenta, the Λ_6^+ bands bend up and thus will be always above two $\Lambda_{4,5}$ bands that bend down. Thus, we conclude that at least one pair of TPs due to the crossing between the Λ_6 bands and the upper branch of $\Lambda_{4,5}$ bands must exist. According to energy dispersion along the C_3 axis for the Kane model (see details in Ref. [42]), we find that 1, 2, or 3 pairs of TPs can exist in one C_3 axis, depending on model parameters. The phase diagram as a function of the parameter C , which determines the energy splitting of two $\Lambda_{4,5}$ bands, and the gap Δ between Γ_6 and Γ_8 states, which influence the effective mass of Λ_6^+ bands, is shown in Fig. 1(g). For a small Δ , strong hybridization between Λ_6^+ and Λ_6^- bands can lead to a positive effective mass for the Λ_6^+ band and thus results in 1 pair of TPs between the Λ_6^+ bands and the upper branch of $\Lambda_{4,5}$ bands [Fig. 1(a)] in phase I in Fig. 1(g). As Δ increases, the effective mass for the Λ_6^+ bands become negative, leading to a double-hump structure [Fig. 1(b)]. With Δ increasing to a critical value, the double-hump Λ_6^+ bands can touch the lower branch of $\Lambda_{4,5}$ bands, giving rise to one more pair of TPs (TP #2 and 2') at the critical line in Fig. 1(g). As Δ further increases, the Λ_6^+ bands can cross the lower branch of $\Lambda_{4,5}$ twice, resulting in 3 pairs of TPs in total for the phase I in Fig. 1(g). TPs are connected by nodal lines and for different phases, we find the connections are different. For the phase I, four nodal lines, three in three mirror planes and one along the C_3 axis, connects the TP #1 to its time-reversal partner TP 1', passing through the Γ point, as shown in Fig. 1(e). The Berry phase around each of three nodal lines in the mirror plane is accumulated to π and characterizes its topological nature (Type-B TPs introduced in Ref. [20]). Three pairs of TPs exist the phase II, with TPs #1 and #2 (1' and 2') connected by nodal lines and TPs #3 and 3' connected by nodal lines through Γ , as shown in Fig. 1(f).

In addition, we note that TPs can also exist in the normal zinc-blende-type band structures without a band inversion, since Γ_6 bands commonly have different mass from $\Gamma_{4,5}$. It provides an alternative way to search for TPs in traditional

TABLE I. List of triple point (TP) half Heusler materials. The band inversion strength Δ is in units of eV. The number of TPs (#) is shown in Fig. 1. The distance of a TP to the Γ point (Δ_k) is specified as a percentage of the $\Gamma - L$ length. The energy of a TP is given with respect to the Fermi energy (ϵ) in unit of meV.

Material	#	Δ	Δ_k	ϵ	Material	#	Δ	Δ_k	ϵ
LuPtBi	1	-1.52	32.5%	-131	YPtBi	1	-1.07	17.1%	-38
	2		26.7%	-144		2		14.3%	-27
	3		1.3%	154		3		0.4%	50
LuAuPb	1	-1.07	24.2%	105	GdPtBi	1	-1.02	14.1%	-22
	2		15.9%	142	LuPdBi	1	-0.69	11.9%	-8
	3		5.0%	201	LaPtBi	1	-0.82	1.3%	8

semiconductors, where the Luttinger model [46] is applicable.

To search for ideal material candidates, we have performed *ab initio* band structure calculations for a large number of half-Heusler compounds using density-functional theory (DFT) with the generalized gradient approximation. We have identified many candidate materials exhibiting TPs with a large momentum separation in their band structure, as listed in Table I. For example, TPs #1 and #2 of $RPtBi$ ($R = Y, Lu$), LuAuPb, LuPdBi, and TP #1 of GdPtBi (paramagnetic phase) lie at large momenta greater than %10 of the $\Gamma - L$ length. The TP #3 is located too close to the Γ point for the observation. We also list the band inversion strength between the Γ_6 and Γ_8 bands in Table I to demonstrate the evolution of the band structure. Roughly consistent with the above phase diagram, TPs shift to larger momenta as the band inversion is enhanced. For comparison, we also show the band structure of LaPtBi in Fig. 2, where TPs appear very close to the Γ point. For convenience, we term materials with TPs at large momenta as long-TP materials, and those with TPs at tiny momenta as short-TP materials. When the Fermi energy crosses a TP in GdPtBi and YPtBi, the TP behaves as the touching point between hole and electron pockets, thereby showing the same feature as a type-II Weyl semimetal [47,48]. Many half-Heusler compounds are known to exhibit much larger band inversions than HgTe. Thus, it is not surprising to find

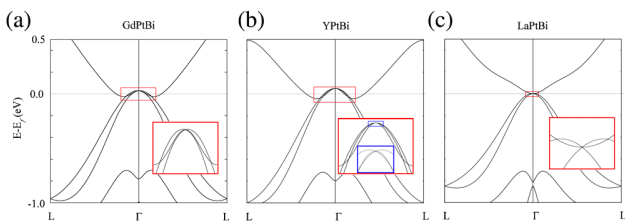


FIG. 2. Bulk band structures with triply degenerate band crossings. The long-TP materials (a) GdPtBi with 2 TPs along the C_3 axis and (b) YPtBi with 6 TPs. The band dispersion along the C_3 axis near the Γ point are magnified to show the TPs on the right panels. (c) The short-TP material LaPtBi are shown for comparison.

long-TP materials here. It has been reported that optimized exchange-correlation functionals in DFT tend to reduce the band inversion of Heusler compounds [49]. We note that this functional correction remains of the general order of the band inversion strength between different Heusler materials, where long-TP materials can still be found in the large band inversion region.

The existence of Fermi arcs on the surface is a hallmark of TPs for their experimental detection. When projected to the (111) surface, six TPs (TPs #1 and 1') locate at the $\bar{\Gamma} - \bar{M}$ line. Because a typical TP is equivalent to two degenerate Weyl points (WPs) with opposite chiralities, typically two Fermi arcs are expected to emerge from a TP. A natural choice is that these two Fermi arcs end at two neighboring TPs separately (one possible case is that a Fermi arc connects those two WPs and disappear as two WPs merge to be a TP). As a consequence, six Fermi arcs form a hexagonlike Fermi surface. We first employed a tight-binding regularization of the Kane model and calculated the surface states on a half-infinite (111) surface. As shown in the surface band structure of Fig. 3(a) with only 1 TP along the $\bar{M} - \bar{\Gamma}$ line, a surface band disperses from the Brillouin zone boundary to the center. Along $\bar{K} - \bar{\Gamma}$, it runs very close to the $\bar{\Gamma}$ point and merges into the bulk background. From \bar{M} to $\bar{\Gamma}$, however, it ends exactly at the TP. On the Fermi surface at E_F crossing the TP, one can clearly see that six Fermi arcs connect six TPs, forming a hexagon shape. Each Fermi arc starts at a TP and ends at the neighboring TP [Fig. 3(a)-(iii)]. Outside the hexagon of Fermi arcs, there is a larger Fermi ring due to the same surface band. When 3 TPs exist along the $\bar{M} - \bar{\Gamma}$ line [Fig. 3(b)], the original surface band still ends at the TP #1 while a new surface band appears to link TP #2 and TP #3 although it is weak in intensity. On the Fermi surface, one can observe that six Fermi arcs connect six TPs #1 [Fig. 3(b)-(ii)] and also six TPs #2 [Fig. 3(b)-(iii)]. We note that the Fermi arc states penetrate deeply into the bulk, similar to the Fermi arcs of a Weyl semimetal TaAs [50,51], since they appear close to the bulk pocket boundary on the Fermi surface. Therefore, we can summarize two important features of TP surface states. (i) The surface band ends at the TP #1 position in the energy dispersion along $\bar{M} - \bar{\Gamma}$.

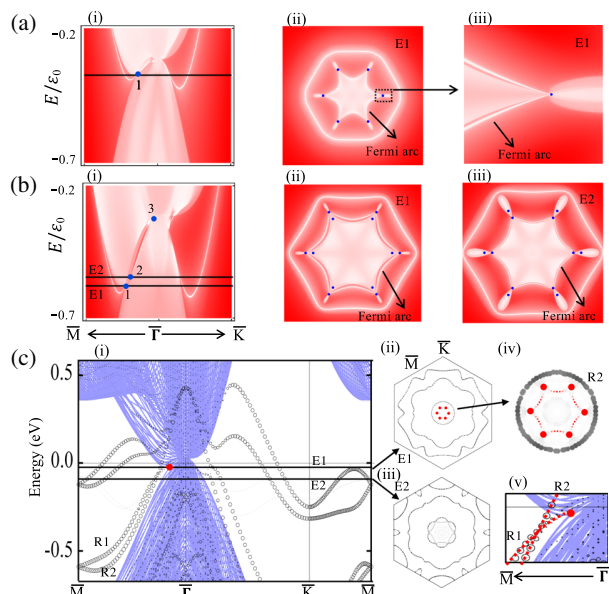


FIG. 3. Surface band structures. (a),(b) Band structure calculated by the tight-binding model on a half-infinite surface with 1 and 3 TPs along $\bar{\Gamma}-\bar{M}$, respectively. Red color stands for low surface intensity and white for strong surface intensity. The triple points are marked by blue points. (c) DFT band structure calculated on a slab model for GdPtBi (paramagnetic phase). (i) The size of the white circles represents the surface contribution and, thus, large circles show the surface states. Bulk bands are indicated by blue curves as a background, where the triple point is shown as the red point. $R1$ and $R2$ are a pair of Rashba-like surface states. (ii) and (iii), Fermi surfaces corresponding to energy $E1$ (crossing the triple point) and $E2$, respectively. The flowerlike Fermi surface in (iii) was measured in previous ARPES experiments. (iv) Magnified inner Fermi ring of (ii). Fermi arcs (red dotted lines) are artificially added as guides to the eye, for they are missing in the DFT band structure due to the finite slab thickness. (v) Expanded view near the triple point. Red dotted lines highlight $R1$ and $R2$ bands. The $R1$ band crosses $R2$ and later ends at the triple point.

(ii) Six Fermi arcs interconnect six TPs related by C_3 and TRS when E_F crosses the TPs.

Regarding materials we have calculated the surface states of GdPtBi based on *ab initio* DFT calculations within a slab model. The slab model includes 54 atomic layers of the (111) surface and the band structure is projected to the top surface that is terminated by Bi atoms. The projected band structure represents the dispersions of surface states [Fig. 3(c)], which agrees well with previous ARPES measurement [28]. There are several trivial surface states due to Bi dangling bonds in the band structure. We point out a pair of Rashba-like surface bands [noted $R1$ and $R2$ in Fig. 3(c)], which disperse up from -0.6 eV at \bar{M} to above E_F at $\bar{\Gamma}$. When approaching the TP, $R1$ does not disperse up together with $R2$, as ordinary Rashba bands do.

Instead, $R1$ crosses $R2$ at energy $E2 = -72$ meV and then ends at the TP at $E1 = -22$ meV [Fig. 3(c)-(v)], fulfilling the first feature of Fermi arc states. Here the surface band structure is a result of the strong hybridization between Fermi arc states and dangling bond states. We point out that the same feature that $R1$ ends at the TP can be found for another long-TP material YPtBi and even a short-TP material LaPtBi; see Ref. [42] for more information. For the Fermi surface corresponding to $E2$ [Fig. 3(c)-(iii)], there are two rings forming a flowerlike shape caused by the $R1$ - $R2$ crossing. For the Fermi surface corresponding to $E1$ [Fig. 3(c)-(ii)], there is only one apparent ring due to $R2$. Here six TPs locate inside the $R2$ ring, where Fermi arcs are expected to exist. However, these Fermi arcs are missing in the DFT band structure. This is due to the finite size effect of the slab model simulations. In experiment, corresponding Fermi arcs should appear but possibly with weak intensity, since they penetrate deeply into the bulk. In previous ARPES experiments, a flowerlike Fermi surface similar to Fig. 3(c)-(iii) was observed for LuPtBi, YPtBi, and GdPtBi [28,29], where $R1$ starts crossing $R2$. However, ARPES did not reach the energy window of TPs, because these Heusler samples are usually hole doped. To fully reach the TP region by ARPES, electron-doped samples are needed to shift E_F by ~ 50 meV with respect to current samples.

In summary, we have predicted the existence of TP fermions in the band structures of several half-Heusler TIs. By *ab initio* calculations and the $k \cdot p$ Kane model, we have identified the existence of multiple TPs at large momenta in the bulk and revealed the existence of Fermi arcs on the surface. The Fermi arcs states end at the TP position in the energy dispersion along $\bar{M}-\bar{\Gamma}$ and connect neighboring TPs at the Fermi surface. To observe TPs and Fermi arcs, currently available samples may need slightly more electron doping for ARPES studies. Alternatively, two-photon photoelectron spectroscopy or scanning tunneling spectroscopy, which can measure empty states, will be ideal for the detection of TP Fermi arcs. The predicted Heusler TP materials are known to exhibit AFM phase (e.g., GdPtBi) [41] and superconductivity (e.g., LuPtBi and YPtBi) [52,53] at low temperatures. They serve as a new platform to investigate the interplay between TPs and magnetism or superconductivity.

We thank Haim Beidenkopf, Nurit Avraham, and Ady Stern for helpful discussions. B. Y. acknowledges the support by the Ruth and Herman Albert Scholars Program for New Scientists and a research grant from the Willner Family Leadership Institute in Weizmann Institute of Science, Israel and by a grant from the German-Israeli Foundation for Scientific Research and Development (GIF Grant No. I-1364-303.7/2016). C.-X. L. acknowledges support from the Office of Naval Research (Grant No. N00014-15-1-2675).

- *binghai.yan@weizmann.ac.il
- [1] X.-L. Qi and S.-C. Zhang, *Rev. Mod. Phys.* **83**, 1057 (2011).
 - [2] M. Z. Hasan and C. L. Kane, *Rev. Mod. Phys.* **82**, 3045 (2010).
 - [3] S. M. Young, S. Zaheer, J. C. Y. Teo, C. L. Kane, E. J. Mele, and A. M. Rappe, *Phys. Rev. Lett.* **108**, 140405 (2012).
 - [4] Z. Wang, Y. Sun, X.-Q. Chen, C. Franchini, G. Xu, H. Weng, X. Dai, and Z. Fang, *Phys. Rev. B* **85**, 195320 (2012).
 - [5] Z. K. Liu, B. Zhou, Y. Zhang, Z. J. Wang, H. M. Weng, D. Prabhakaran, S.-K. Mo, Z. X. Shen, Z. Fang, X. Dai, Z. Hussain, and Y. L. Chen, *Science* **343**, 864 (2014).
 - [6] S. Xu, C. Liu, S. K. Kushwaha, R. Sankar, J. W. Krizan, I. Belopolski, M. Neupane, G. Bian, N. Alidoust, T. R. Chang, H. T. Jeng, C. Y. Huang, W. F. Tsai, H. Lin, P. P. Shibayev, F. C. Chou, R. J. Cava, and M. Z. Hasan, *Science* **347**, 294 (2015).
 - [7] X. G. Wan, A. M. Turner, A. Vishwanath, and S. Y. Savrasov, *Phys. Rev. B* **83**, 205101 (2011).
 - [8] G. E. Volovik, *The Universe in a Helium Droplet* (Clarendon Press, Oxford, England, 2003).
 - [9] A. A. Burkov, M. D. Hook, and L. Balents, *Phys. Rev. B* **84**, 235126 (2011).
 - [10] H. Weng, C. Fang, Z. Fang, B. A. Bernevig, and X. Dai, *Phys. Rev. X* **5**, 011029 (2015).
 - [11] S.-M. Huang, S.-Y. Xu, I. Belopolski, C.-C. Lee, G. Chang, B. Wang, N. Alidoust, G. Bian, M. Neupane, C. Zhang, S. Jia, A. Bansil, H. Lin, and M. Z. Hasan, *Nat. Commun.* **6**, 8373 (2015).
 - [12] B. Q. Lv, H. M. Weng, B. B. Fu, X. P. Wang, H. Miao, J. Ma, P. Richard, X. C. Huang, L. X. Zhao, G. F. Chen, Z. Fang, X. Dai, T. Qian, and H. Ding, *Phys. Rev. X* **5**, 031013 (2015).
 - [13] S.-Y. Xu, I. Belopolski, N. Alidoust, M. Neupane, G. Bian, C. Zhang, R. Sankar, G. Chang, Y. Zhujun, C.-C. Lee, H. Shin-Ming, H. Zheng, J. Ma, D. S. Sanchez, B. Wang, A. Bansil, F. Chou, P. P. Shibayev, H. Lin, S. Jia, and M. Z. Hasan, *Science* **349**, 613 (2015).
 - [14] L. X. Yang, Z. K. Liu, Y. Sun, H. Peng, H. F. Yang, T. Zhang, B. Zhou, Y. Zhang, Y. F. Guo, M. Rahn, D. Prabhakaran, Z. Hussain, S. K. Mo, C. Felser, B. Yan, and Y. L. Chen, *Nat. Phys.* **11**, 728 (2015).
 - [15] B. Yan and C. Felser, *Annu. Rev. Condens. Matter Phys.* **8**, 337 (2017).
 - [16] N. P. Armitage, E. J. Mele, and A. Vishwanath, [arXiv:1705.01111](https://arxiv.org/abs/1705.01111) [*Rev. Mod. Phys.* (to be published)].
 - [17] B. J. Wieder, Y. Kim, A. M. Rappe, and C. L. Kane, *Phys. Rev. Lett.* **116**, 186402 (2016).
 - [18] B. Bradlyn, J. Cano, Z. Wang, M. G. Vergniory, C. Felser, R. J. Cava, and B. A. Bernevig, *Science* **353**, aaf5037 (2016).
 - [19] S. Zaheer, S. M. Young, D. Cellucci, J. C. Y. Teo, C. L. Kane, E. J. Mele, and A. M. Rappe, *Phys. Rev. B* **87**, 045202 (2013).
 - [20] Z. Zhu, G. W. Winkler, Q. S. Wu, J. Li, and A. A. Soluyanov, *Phys. Rev. X* **6**, 031003 (2016).
 - [21] G. W. Winkler, Q. S. Wu, M. Troyer, P. Krogstrup, and A. A. Soluyanov, *Phys. Rev. Lett.* **117**, 076403 (2016).
 - [22] H. Weng, C. Fang, Z. Fang, and X. Dai, *Phys. Rev. B* **93**, 241202 (2016).
 - [23] H. Weng, C. Fang, Z. Fang, and X. Dai, *Phys. Rev. B* **94**, 165201 (2016).
 - [24] J. Yu, B. Yan, and C.-X. Liu, *Phys. Rev. B* **95**, 235158 (2017).
 - [25] I. C. Fulga and A. Stern, *Phys. Rev. B* **95**, 241116 (2017).
 - [26] B. Q. Lv, Z. L. Feng, Q. N. Xu, J. Z. Ma, and L. Y. Kong, *Nature (London)* **546**, 627 (2017).
 - [27] C. Shekhar, Y. Sun, N. Kumar, M. Nicklas, K. Manna, V. Suess, O. Young, I. Leermakers, T. Foerster, M. Schmidt, L. Muechler, P. Werner, W. Schnelle, U. Zeitler, B. Yan, S. S. P. Parkin, and C. Felser, [arXiv:1703.03736](https://arxiv.org/abs/1703.03736).
 - [28] C. Liu, Y. Lee, T. Kondo, E. D. Mun, M. Caudle, B. N. Harmon, S. L. Bud'ko, P. C. Canfield, and A. Kaminski, *Phys. Rev. B* **83**, 205133 (2011).
 - [29] Z. K. Liu, L. X. Yang, S. C. Wu, C. Shekhar, J. Jiang, H. F. Yang, Y. Zhang, S.-K. Mo, Z. Hussain, B. Yan, C. Felser, and Y. L. Chen, *Nat. Commun.* **7**, 12924 (2016).
 - [30] S. Chadov, X. L. Qi, J. K. Kübler, G. H. Fecher, C. Felser, and S. C. Zhang, *Nat. Mater.* **9**, 541 (2010).
 - [31] H. Lin, L. A. Wray, Y. Xia, S. Xu, S. Jia, R. J. Cava, A. Bansil, and M. Z. Hasan, *Nat. Mater.* **9**, 546 (2010).
 - [32] D. Xiao, Y. Yao, W. Feng, J. Wen, W. Zhu, X.-Q. Chen, G. M. Stocks, and Z. Zhang, *Phys. Rev. Lett.* **105**, 096404 (2010).
 - [33] B. Yan and A. de Visser, *MRS Bull.* **39**, 859 (2014).
 - [34] J. A. Logan, S. J. Patel, S. D. Harrington, C. M. Polley, B. D. Schultz, T. Balasubramanian, A. Janotti, A. Mikkelsen, and C. J. Palmström, *Nat. Commun.* **7**, 11993 (2016).
 - [35] M. Hirschberger, S. Kushwaha, Z. Wang, Q. Gibson, S. Liang, C. A. Belvin, B. A. Bernevig, R. J. Cava, and N. P. Ong, *Nat. Mater.* **15**, 1161 (2016).
 - [36] C. Shekhar, A. K. Nayak, S. Singh, N. Kumar, S.-C. Wu, Y. Zhang, A. C. Komarek, E. Kampert, Y. Skourski, J. Wosnitza, W. Schnelle, A. McCollam, U. Zeitler, J. Kübler, S. Parkin, B. Yan, and C. Felser, [arXiv:1604.01641](https://arxiv.org/abs/1604.01641).
 - [37] J. Ruan, S.-K. Jian, H. Yao, H. Zhang, S.-C. Zhang, and D. Xing, *Nat. Commun.* **7**, 11136 (2016).
 - [38] J. Cano, B. Bradlyn, Z. Wang, M. Hirschberger, N. P. Ong, and B. A. Bernevig, *Phys. Rev. B* **95**, 161306 (2017).
 - [39] B. A. Bernevig, T. L. Hughes, and S. C. Zhang, *Science* **314**, 1757 (2006).
 - [40] R. Winkler, S. Papadakis, E. De Poortere, and M. Shayegan, *Spin-Orbit Coupling in Two-Dimensional Electron and Hole Systems* (Springer, New York, 2003), Vol. 41.
 - [41] P. C. Canfield, J. Thompson, W. Beyermann, A. Lacerda, M. Hundley, E. Peterson, Z. Fisk, and H. Ott, *J. Appl. Phys.* **70**, 5800 (1991).
 - [42] See Supplemental Material at <http://link.aps.org/supplemental/10.1103/PhysRevLett.119.136401>, which includes Refs. [43–45], for more details of model Hamiltonians, calculation methods, and results.
 - [43] M. I. Aroyo, J. M. Perez-Mato, C. Capillas, E. Kroumova, S. Ivantchev, G. Madariaga, A. Kirov, and H. Wondratschek, *Zeitschrift für Kristallographie-Crystalline Materials* **221**, 15 (2006).
 - [44] W. Al-Sawai, H. Lin, R. S. Markiewicz, L. A. Wray, Y. Xia, S.-Y. Xu, M. Z. Hasan, and A. Bansil, *Phys. Rev. B* **82**, 125208 (2010).
 - [45] G. Burns, *Introduction to Group Theory with Applications: Materials Science and Technology* (Academic Press, New York, 2014).
 - [46] J. M. Luttinger, *Phys. Rev.* **102**, 1030 (1956).
 - [47] A. A. Soluyanov, D. Gresch, Z. Wang, Q. Wu, M. Troyer, X. Dai, and B. A. Bernevig, *Nature (London)* **527**, 495 (2015).

-
- [48] Y. Sun, S. C. Wu, M. N. Ali, C. Felser, and B. Yan, *Phys. Rev. B* **92**, 161107(R) (2015).
- [49] W. Feng, D. Xiao, Y. Zhang, and Y. Yao, *Phys. Rev. B* **82**, 235121 (2010).
- [50] R. Batabyal, N. Morali, N. Avraham, Y. Sun, M. Schmidt, C. Felser, A. Stern, B. Yan, and H. Beidenkopf, *Sci. Adv.* **2**, e1600709 (2016).
- [51] H. Inoue, A. Gyenis, Z. Wang, J. Li, S. W. Oh, S. Jiang, N. Ni, B. A. Bernevig, and A. Yazdani, *Science* **351**, 1184 (2016).
- [52] N. P. Butch, P. Syers, K. Kirshenbaum, A. P. Hope, and J. Paglione, *Phys. Rev. B* **84**, 220504 (2011).
- [53] F. F. Tafti, T. Fujii, A. Juneau-Fecteau, S. Rene de Cotret, N. Doiron-Leyraud, A. Asamitsu, and L. Taillefer, *Phys. Rev. B* **87**, 184504 (2013).

Supplementary Materials for “Prediction of triple point fermions in simple half-Heusler topological insulators”

Hao Yang,¹ Jiabin Yu,² Stuart S. P. Parkin,¹ Claudia Felser,³ Chao-Xing Liu,² and Binghai Yan^{4,*}

¹*Max Planck Institute of Microstructure Physics, Weinberg 2, 06120 Halle, Germany*

²*Department of Physics, the Pennsylvania State University, University Park, PA, 16802*

³*Max Planck Institute for Chemical Physics of Solids, 01187 Dresden, Germany*

⁴*Department of Condensed Matter Physics, Weizmann Institute of Science, Rehovot, 7610001, Israel*

The outline is in the following.

1. General Conditions for Existence of Triple Points.
2. Triple Points in a Chosen Parameter Region.
3. Kane Model Parameter Choices for Surface States.
4. Bands structure of LuPtBi, LuAuPb and LuPdBi.
5. *Ab initio* calculations of surface states for YPtBi and LaPtBi.

I. General Conditions for Existence of Triple Points

For half-Heusler materials without any external effects like magnetic field or distortion, their space group and point group are $F\bar{4}3m$ group and T_d group respectively.^{1,2} Therefore, their physics around Γ point near Fermi level is commonly described by six-band Kane model³. On the bases $|\Gamma_6, \frac{1}{2}\rangle$, $|\Gamma_6, -\frac{1}{2}\rangle$, $|\Gamma_8, \frac{3}{2}\rangle$, $|\Gamma_8, \frac{1}{2}\rangle$, $|\Gamma_8, -\frac{1}{2}\rangle$ and $|\Gamma_8, -\frac{3}{2}\rangle$, the standard six-band Kane model is³

$$H_{Kane}(\mathbf{k}) = \left(\begin{array}{c|c} H_{\Gamma_6}(\mathbf{k}) & V \\ \hline V^\dagger & H_{\Gamma_8}(\mathbf{k}) \end{array} \right), \quad (1)$$

where

$$V = \frac{P}{\sqrt{6}} \begin{pmatrix} -\sqrt{3}k_+ & 2k_z & k_- & 0 \\ 0 & -k_+ & 2k_z & \sqrt{3}k_- \end{pmatrix} + \frac{B_{8v}^+}{\sqrt{6}} \begin{pmatrix} \sqrt{3}k_-k_z & 2ik_xk_y & k_+k_z & 0 \\ 0 & k_-k_z & 2ik_xk_y & \sqrt{3}k_+k_z \end{pmatrix}, \quad (2)$$

$$+ \frac{B_{8v}^-}{3\sqrt{2}} \begin{pmatrix} 0 & \sqrt{3}K^2 & 0 & k_{\parallel}^2 - 2k_z^2 \\ -k_{\parallel}^2 + 2k_z^2 & 0 & -\sqrt{3}K^2 & 0 \end{pmatrix}$$

$$H_{\Gamma_6}(\mathbf{k}) = (E_c + \beta_c k^2) \mathbb{1}_2 \quad (3)$$

with $\mathbb{1}_2$ to be the 2×2 identity matrix,

$$H_{\Gamma_8}(\mathbf{k}) = H_0(\mathbf{k}) + H_C(\mathbf{k}) \quad (4)$$

with

$$H_0(\mathbf{k}) = \frac{4}{15}(J_x^2 + J_y^2 + J_z^2)h_0 + \frac{1}{3}(2J_z^2 - J_x^2 - J_y^2)h_1 + \frac{1}{\sqrt{3}}(J_x^2 - J_y^2)h_2 + \frac{2}{\sqrt{3}}J_{xy}h_3 + \frac{2}{\sqrt{3}}J_{zx}h_4 + \frac{2}{\sqrt{3}}J_{yz}h_5 \quad (5)$$

and

$$H_C(\mathbf{k}) = \frac{2}{\sqrt{3}}C(k_xV_x + k_yV_y + k_zV_z). \quad (6)$$

Here we have $h_0 = E_v - \beta_c\gamma_1k^2$, $h_1 = \beta_c\gamma_2(2k_z^2 - k_{\parallel}^2)$, $h_2 = \sqrt{3}\beta_c\gamma_2K^2$, $h_3 = 2\sqrt{3}\beta_c\gamma_3k_xk_y$, $h_4 = 2\sqrt{3}\beta_c\gamma_3k_xk_z$, and $h_5 = 2\sqrt{3}\beta_c\gamma_3k_yk_z$. J_i 's are angular momentum matrices for spin 3/2, $J_{ij} = \frac{1}{2}\{J_i, J_j\}$, $V_x = \frac{1}{2}\{J_x, J_y^2 - J_z^2\}$, $V_y = \frac{1}{2}\{J_y, J_z^2 - J_x^2\}$, $V_z = \frac{1}{2}\{J_z, J_x^2 - J_y^2\}$, $\beta_c = \hbar^2/(2m')$, m' is the effective mass of Γ_6 bands near Γ point, $k^2 = k_x^2 + k_y^2 + k_z^2$, $k_{\parallel}^2 = k_x^2 + k_y^2$, $K^2 = k_x^2 - k_y^2$ and $k_{\pm} = k_x \pm ik_y$.

In this work, $\gamma_2 \neq 0$ and $\gamma_3 \neq 0$ are always assumed. Moreover, $\beta_c > 0$ and $E_c < E_v$ are assumed, which means Γ_6 bands are lower than Γ_8 bands for half-Heusler materials with inverted band structure.⁴⁻⁷

For symmorphic triple points(TPs), C_{3v}^* spin double group is typically essential.⁸ The character table of C_{3v}^* spin double group is shown in Tab.I.

C_{3v}^*	E	R	C_3, C_3^2R	C_3^2, C_3R	$3\sigma_v$	$3\sigma_vR$
Λ_1	1	1	1	1	1	1
Λ_2	1	1	1	1	-1	-1
Λ_3	2	2	-1	-1	0	0
Λ_4	1	-1	-1	1	i	-i
Λ_5	1	-1	-1	1	-i	i
Λ_6	2	-2	1	-1	0	0

TABLE I. Character Table of Spin Double Group C_{3v}^* ⁹

Inside T_d group, there are 4 different C_{3v} subgroups with principle axis (axis of C_3) along (111), $(\bar{1}11)$, $(1\bar{1}1)$ and $(11\bar{1})$, which can be related by S_4^z operation. That means we only need to consider one C_{3v} group, and the one chosen to be studied here is C_{3v} with C_3 along (111) direction, noted as $C_{3v}^{(111)}$. Mirror planes of $C_{3v}^{(111)}$ are $(1\bar{1}0)$, $(\bar{1}01)$ and

(01 $\bar{1}$) planes.

For Γ_6 and Γ_8 bases, the generators of $C_{3v}^{(111)}$ are represented as

$$C_3(111) \doteq \begin{pmatrix} \exp(-i\frac{S_x+S_y+S_z}{\sqrt{3}}\frac{2\pi}{3}) & 0 \\ 0 & \exp(-i\frac{J_x+J_y+J_z}{\sqrt{3}}\frac{2\pi}{3}) \end{pmatrix}$$

$$\pi_{1\bar{1}0} \doteq \begin{pmatrix} \exp(-i\frac{S_x-S_y}{\sqrt{2}}\pi) & 0 \\ 0 & -\exp(-i\frac{J_x-J_y}{\sqrt{2}}\pi) \end{pmatrix}$$

, where $S_i = \sigma_i/2$ and σ_i 's are Pauli matrices. Based on that, we can group Γ_6 and Γ_8 bases into those three irreducible representations. Wave functions for each irreducible representation in bases $|\Gamma_6, 1/2\rangle$, $|\Gamma_6, -1/2\rangle$, $|\Gamma_8, 3/2\rangle$, $|\Gamma_8, 1/2\rangle$, $|\Gamma_8, -1/2\rangle$ and $|\Gamma_8, -3/2\rangle$ are shown below:

Λ_4 :

$$\psi_{\Lambda_4} = N_4 \left(0, 0, \frac{1-i}{\sqrt{2}}, \frac{\sqrt{2}-i}{\sqrt{3}}, i \left(\frac{1}{\sqrt{6}} + \frac{1}{\sqrt{3}} \right) - \sqrt{\frac{1}{6} (3-2\sqrt{2})}, 1 \right) \quad (7)$$

Λ_5 :

$$\psi_{\Lambda_5} = N_5 \left(0, 0, \frac{-1+i}{\sqrt{2}}, -\frac{\sqrt{2}+i}{\sqrt{3}}, i \sqrt{\frac{1}{6} (3-2\sqrt{2})} - \frac{1}{\sqrt{3}} - \frac{1}{\sqrt{6}}, 1 \right) \quad (8)$$

Λ_6 :

$$\psi_{\Lambda_6,1} = \frac{1}{\sqrt{6}} \left(0, 0, -1-i, i\sqrt{3}, 0, 1 \right), \psi_{\Lambda_6,2} = \frac{1}{\sqrt{6}} \left(0, 0, i, 0, \sqrt{3}, 1+i \right) \quad (9)$$

$$\phi_{\Lambda_6,1} = (1, 0, 0, 0, 0, 0), \phi_{\Lambda_6,2} = (0, 1, 0, 0, 0, 0) \quad (10)$$

, where N_4 and N_5 are normalization factors. Eq.9 and Eq.10 list two linearly independent sets of wavefunctions of the Λ_6 irreducible representation, and any linearly combination of wavefunctions in Eqs. 8 and 9 can still give a Λ_6 irreducible representation of C_{3v}^* . On bases $(\psi_{\Lambda_4}, \psi_{\Lambda_5}, \psi_{\Lambda_6,1}, \psi_{\Lambda_6,2}, \phi_{\Lambda_6,1}, \phi_{\Lambda_6,2})$, the $H_{Kane}(\mathbf{k})$ along $k_x = k_y = k_z = k$ direction takes the form,

$$\begin{pmatrix} E_{\Lambda_4}(k) & 0 & 0 & 0 & 0 & 0 \\ 0 & E_{\Lambda_5}(k) & 0 & 0 & 0 & 0 \\ 0 & 0 & E_v - 3k^2\beta_c(\gamma_1 + 2\gamma_3) & 0 & -\frac{2ik(P-iB_{8v}^+k)}{\sqrt{3}} & \frac{(1+i)k(P-iB_{8v}^+k)}{\sqrt{3}} \\ 0 & 0 & 0 & E_v - 3k^2\beta_c(\gamma_1 + 2\gamma_3) & \frac{(1+i)k(P-iB_{8v}^+k)}{\sqrt{3}} & \frac{2k(P-iB_{8v}^+k)}{\sqrt{3}} \\ 0 & 0 & \frac{2ik(P+iB_{8v}^+k)}{\sqrt{3}} & \frac{(1-i)k(P+iB_{8v}^+k)}{\sqrt{3}} & 3\beta_c k^2 + E_c & 0 \\ 0 & 0 & \frac{(1-i)k(P+iB_{8v}^+k)}{\sqrt{3}} & \frac{2k(P+iB_{8v}^+k)}{\sqrt{3}} & 0 & 3\beta_c k^2 + E_c \end{pmatrix} \quad (11)$$

, where $E_{\Lambda_4}(k) = E_v - k(3k\beta_c(\gamma_1 - 2\gamma_3) + C\sqrt{6})$, $E_{\Lambda_5}(k) = E_v + k(\sqrt{6}C - 3k\beta_c(\gamma_1 - 2\gamma_3))$, and the corresponding energy dispersion along $k_x = k_y = k_z = k$ is,

$$\begin{aligned} E_{\Lambda_4}(k) &= E_v - k(3k\beta_c(\gamma_1 - 2\gamma_3) + C\sqrt{6}) \\ E_{\Lambda_5}(k) &= E_v + k(\sqrt{6}C - 3k\beta_c(\gamma_1 - 2\gamma_3)) \\ E_{\Lambda_6^-}(k) &= \frac{1}{2} \left(E_c + E_v - 3\beta_c k^2(\gamma_1 + 2\gamma_3 - 1) - \sqrt{[E_c - E_v + 3\beta_c k^2(\gamma_1 + 2\gamma_3 + 1)]^2 + 8k^2(P^2 + (B_{8v}^+)^2 k^2)} \right) \\ E_{\Lambda_6^+}(k) &= \frac{1}{2} \left(E_c + E_v - 3\beta_c k^2(\gamma_1 + 2\gamma_3 - 1) + \sqrt{[E_c - E_v + 3\beta_c k^2(\gamma_1 + 2\gamma_3 + 1)]^2 + 8k^2(P^2 + (B_{8v}^+)^2 k^2)} \right) \end{aligned} \quad (12)$$

, where $E_{\Lambda_6^\pm}(k)$ are both doubly degenerate.

It is convenient to define the following dimensionless quantities, $\tilde{E} \equiv E/\varepsilon_0$, $\tilde{k} \equiv ka$, $\tilde{C} \equiv C/(\beta_c/a)$, $\tilde{B}_{8v}^\pm \equiv B_{8v}^\pm/\beta_c$

and $\tilde{P} \equiv P/(\beta_c/a)$, where $\varepsilon_0 \equiv \frac{\beta_c}{a^2}$ and a is a positive parameters with unit of length.

Since $\tilde{E}_{\Lambda_6^-}(0) = \tilde{E}_c$ and $\tilde{E}_{\Lambda_6^+}(0) = \tilde{E}_v$, only $\tilde{E}_{\Lambda_6^+}(k)$ is involved to create TPs. TPs are created by band crossing between $\tilde{E}_{\Lambda_6^+}(k)$ and $\tilde{E}_{\Lambda_4}(\tilde{k})$ or $\tilde{E}_{\Lambda_6^+}(\tilde{k})$ and $\tilde{E}_{\Lambda_5}(\tilde{k})$. Since $\psi_{\Lambda_4} \propto \Theta\psi_{\Lambda_5}$, $\psi_{\Lambda_{6,1}} \propto \Theta\psi_{\Lambda_{6,2}}$ and $\phi_{\Lambda_{6,1}} \propto \Theta\phi_{\Lambda_{6,2}}$, we have $\tilde{E}_{\Lambda_4}(\tilde{k}) = \tilde{E}_{\Lambda_5}(-\tilde{k})$ and $\tilde{E}_{\Lambda_6^\pm}(\tilde{k}) = \tilde{E}_{\Lambda_6^\pm}(-\tilde{k})$, where Θ is time reversal symmetry operation. That means we only need to consider the band crossing situation between $\tilde{E}_{\Lambda_6^+}(\tilde{k})$ and $\tilde{E}_{\Lambda_4}(\tilde{k})$ and the band crossing condition between $\tilde{E}_{\Lambda_6^+}(\tilde{k})$ and $\tilde{E}_{\Lambda_5}(\tilde{k})$ can be obtained from time reversal symmetry.

Band crossing condition between $\tilde{E}_{\Lambda_6^+}(\tilde{k})$ and $\tilde{E}_{\Lambda_4}(\tilde{k})$ is

$$\tilde{E}_{\Lambda_4}(\tilde{k}) = \tilde{E}_{\Lambda_6^+}(\tilde{k}) \Leftrightarrow \tilde{k} \left(2\sqrt{6}\tilde{C} + 3\tilde{k}(\gamma_1 - 6\gamma_3 + 1) \right) + \tilde{E}_c - \tilde{E}_v + \sqrt{\left[\tilde{E}_c - \tilde{E}_v + 3\tilde{k}^2(\gamma_1 + 2\gamma_3 + 1) \right]^2 + 8\tilde{k}^2(\tilde{P}^2 + (\tilde{B}_{8v}^+)^2\tilde{k}^2)} = 0 \quad (13)$$

That is equivalent to

$$\tilde{k} \left(2\sqrt{6}\tilde{C} + 3\tilde{k}(\gamma_1 - 6\gamma_3 + 1) \right) + \tilde{E}_c - \tilde{E}_v \leq 0 \ \& \ \tilde{k} \left(a_0 + a_1\tilde{k} + a_2\tilde{k}^2 + a_3\tilde{k}^3 \right) = 0 \quad (14)$$

, where $a_0 = \sqrt{6}\tilde{C}(\tilde{E}_v - \tilde{E}_c)$, $a_1 = -6\tilde{C}^2 + 12\gamma_3\tilde{E}_c - 12\gamma_3\tilde{E}_v + 2\tilde{P}^2$, $a_2 = -3\sqrt{6}\tilde{C}\gamma_1 + 18\sqrt{6}\tilde{C}\gamma_3 - 3\sqrt{6}\tilde{C}$ and $a_3 = 36\gamma_1\gamma_3 - 72\gamma_3^2 + 36\gamma_3 + 2(\tilde{B}_{8v}^+)^2$.

Eq.14 gives $\tilde{k} = 0$ solution, which is the 4-fold degenerate point at Γ point instead of a TP. All other $\tilde{k} \neq 0$ solutions are TPs if $\tilde{E}_{\Lambda_5}(\tilde{k})$ does not cross with $\tilde{E}_{\Lambda_4}(\tilde{k})$ at those solution \tilde{k} points.

The band crossing condition between $\tilde{E}_{\Lambda_5}(\tilde{k})$ and $\tilde{E}_{\Lambda_4}(\tilde{k})$ is

$$\tilde{E}_{\Lambda_4}(\tilde{k}) = \tilde{E}_{\Lambda_5}(\tilde{k}) \Leftrightarrow \tilde{C}\tilde{k} = 0 \quad (15)$$

, which means they only cross at Γ point if $C \neq 0$. If $\tilde{C} = 0$, $\tilde{E}_{\Lambda_4}(\tilde{k}) = \tilde{E}_{\Lambda_5}(\tilde{k})$ would be always true and there would be no TPs. TPs will emerge for $\tilde{C} \neq 0$.

Based on the discussion above, we have a condition for a TP to exist at \tilde{k} :

$$\tilde{C} \neq 0 \ \& \ b_0 + b_1\tilde{k} + b_2\tilde{k}^2 \leq 0 \ \& \ a_0 + a_1\tilde{k} + a_2\tilde{k}^2 + a_3\tilde{k}^3 = 0 \ \& \ \tilde{k} \neq 0 \quad (16)$$

, where $b_0 = \tilde{E}_c - \tilde{E}_v$, $b_1 = 2\sqrt{6}\tilde{C}$ and $b_2 = 3(\gamma_1 - 6\gamma_3 + 1)$.

Condition listed in Eq.16 only allows at most three solutions, which means there are at most six TPs along one C_3 axis after taking time reversal symmetry.

II. Triple Points in a Chosen Parameter Region

To illustrate the physics, we choose this set of parameters:

$\frac{E_v}{\varepsilon_0}$	γ_1	γ_3	$\frac{P}{\beta_c/a}$	B_{8v}^+/β_c	B_{8v}^-/β_c
0	2	$\frac{1}{2}$	$\frac{5}{2}$	0	0

, where $\varepsilon_0 = \frac{\beta_c}{a^2}$, a is a positive parameters with unit of length, $\tilde{E}_{cv} \equiv \frac{E_c - E_v}{\varepsilon_0} \in [-5, -0.5]$ and $\tilde{C} \equiv \frac{C}{\beta_c/a} \in [-0.3, -0.01]$. This is the parameter choice for the phase diagram shown in Fig.1g.

In this case,

b_0	b_1	b_2	a_0	a_1	a_2	a_3
\tilde{E}_{cv}	$2\sqrt{6}\tilde{C}$	0	$-\sqrt{6}\tilde{C}\tilde{E}_{cv}$	$12.5 - 6\tilde{C}^2 + 6\tilde{E}_{cv}$	0	36

Under these conditions,

$$b_0 + b_1\tilde{k} + b_2\tilde{k}^2 \leq 0 \Leftrightarrow \tilde{k} \geq -\frac{b_0}{b_1}$$

Now, we will prove that all roots of $a_0 + a_1\tilde{k} + a_2\tilde{k}^2 + a_3\tilde{k}^3 = 0$ lie in $[-\frac{b_0}{b_1}, +\infty)$ for the parameter region we choose.

Proof:

Define $\tilde{k}_0 \equiv -\frac{b_0}{b_1}$.

(i) Prove $a_0 + a_1\tilde{k}_0 + a_2\tilde{k}_0^2 + a_3\tilde{k}_0^3 < 0$ for the parameter region we choose.

$$a_0 + a_1\tilde{k}_0 + a_2\tilde{k}_0^2 + a_3\tilde{k}_0^3 = -\frac{\tilde{E}_{cv}}{4\sqrt{6}\tilde{C}^3} \left(12\tilde{C}^4 + 25\tilde{C}^2 + 12\tilde{C}^2\tilde{E}_{cv} + 3\tilde{E}_{cv}^2 \right)$$

. For the chosen parameter region, $-\frac{\tilde{E}_{cv}}{4\sqrt{6}\tilde{C}^3} < 0$ and $\left(12\tilde{C}^4 + 25\tilde{C}^2 + 12\tilde{C}^2\tilde{E}_{cv} + 3\tilde{E}_{cv}^2 \right) > 0$, therefore

$$a_0 + a_1\tilde{k}_0 + a_2\tilde{k}_0^2 + a_3\tilde{k}_0^3 < 0$$

(ii) Prove $\frac{d}{d\tilde{k}}(a_0 + a_1\tilde{k} + a_2\tilde{k}^2 + a_3\tilde{k}^3) > 0$ for any $\tilde{k} < \tilde{k}_0$ and the parameter region we choose.

$$\frac{d}{d\tilde{k}}(a_0 + a_1\tilde{k} + a_2\tilde{k}^2 + a_3\tilde{k}^3) = -6\tilde{C}^2 + 6\tilde{E}_{cv} + 108\tilde{k}^2 + \frac{25}{2}$$

, which means the minimum of $\frac{d}{d\tilde{k}}(a_0 + a_1\tilde{k} + a_2\tilde{k}^2 + a_3\tilde{k}^3)$ is at $\tilde{k} = 0$. Since $-6\tilde{C}^2 + 6\tilde{E}_{cv} + 108\tilde{k}_0^2 + \frac{25}{2} > 0$ and $\tilde{k}_0 < 0$ in the chosen parameter region, we have $\frac{d}{d\tilde{k}}(a_0 + a_1\tilde{k} + a_2\tilde{k}^2 + a_3\tilde{k}^3) > 0$ for any $\tilde{k} < \tilde{k}_0$.

In summary, for any parameter choice in the chosen parameter region, since $a_0 + a_1\tilde{k}_0 + a_2\tilde{k}_0^2 + a_3\tilde{k}_0^3 < 0$ and $\frac{d}{d\tilde{k}}(a_0 + a_1\tilde{k} + a_2\tilde{k}^2 + a_3\tilde{k}^3) > 0$ for any $\tilde{k} < \tilde{k}_0$, we have $a_0 + a_1\tilde{k} + a_2\tilde{k}^2 + a_3\tilde{k}^3 < 0$ for any $\tilde{k} < \tilde{k}_0$.

Therefore, all \tilde{k} solutions of $a_0 + a_1\tilde{k} + a_2\tilde{k}^2 + a_3\tilde{k}^3 = 0$ in the chosen parameter region are larger than $\tilde{k}_0 \equiv -\frac{b_0}{b_1}$.

End Of Proof.

It means the number of TPs is only determined by the number of roots of $a_0 + a_1(ka) + a_2(ka)^2 + a_3(ka)^3 = 0$ for our choices of parameters. For convenience, we define following parameters:

$$\begin{aligned} \eta &= 18a_0a_1a_2a_3 - 4a_2^3a_0 + a_2^2a_1^2 - 4a_3a_1^3 - 27a_3^2a_0^2 \\ \eta_0 &= a_2^2 - 3a_3a_1 \end{aligned} \quad (17)$$

It turns out, in the chosen parameter region,

- (i) if $\eta < 0$, and there is only one root, which means there are two TPs on one C_3 axis;
- (ii) if $\eta = 0$ and $\eta_0 \neq 0$, there are one single root and one double root, which means there are four TPs on one C_3 axis;
- (iii) if $\eta > 0$ and there are three roots, which means there are six TPs on one C_3 axis;
- (iv) $\eta = 0$ and $\eta_0 = 0$ doesn't exist.

Those give the phase diagram shown in Fig.1g.

III. Kane Model Parameter Choices for Surface States

$\frac{E_c}{\varepsilon_0}$	$\frac{E_v}{\varepsilon_0}$	γ_1	γ_2	γ_3	$\frac{C}{\beta_c/a}$	$\frac{P}{\beta_c/a}$	B_{sv}^+/β_c	B_{sv}^-/β_c
-2	0	2	-1	0.5	-0.15	2.5	0	0

TABLE II. Choices of Kane model parameters for Fig.3a with 2 TPs on one C_3 axis.

$\frac{E_c}{\varepsilon_0}$	$\frac{E_v}{\varepsilon_0}$	γ_1	γ_2	γ_3	$\frac{C}{\beta_c/a}$	$\frac{P}{\beta_c/a}$	B_{sv}^+/β_c	B_{sv}^-/β_c
-3	0	2	-1	0.5	-0.05	2.5	0	0

TABLE III. Choices of Kane model parameters for Fig.3b with 6 TPs on one C_3 axis.

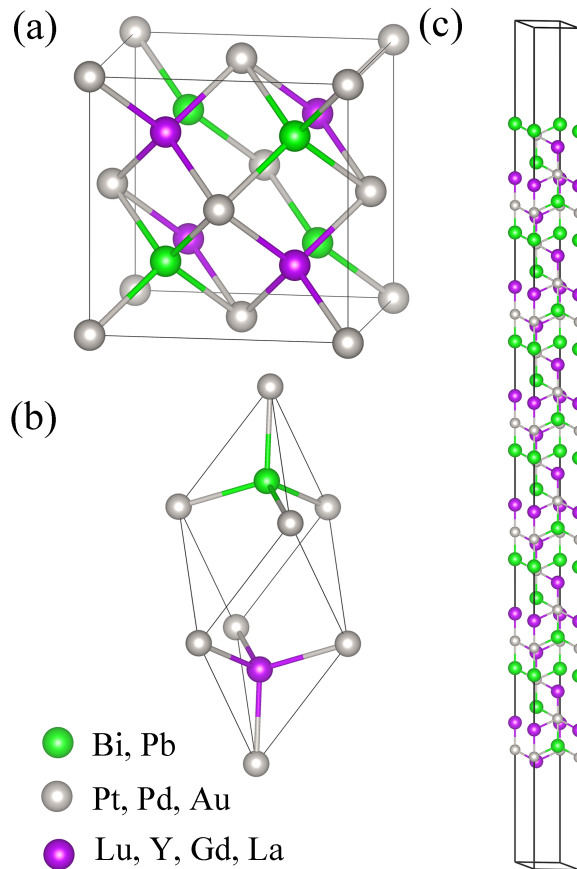


FIG. S1. Crystal structure of the calculated half-Heusler compounds. (a) unitcell, (b) primitive cell and (c) slab structure.

IV. Crystal structure and bands structure of LuPtBi, LuAuPb and LuPdBi

V. *Ab initio* calculations of surface states for YPtBi and LaPtBi.

The electronic ground states of these half Heusler compounds were calculated by using density-functional theory (DFT) within the Perdew-Burke-Ernzerhof-type generalized-gradient approximation (GGA)¹⁰ using the Vienna *ab initio* Simulation Package (VASP)¹¹. For the bulk materials calculation, primitive cells with experimental crystal parameters were selected as shown in Fig.S1(b). In order to get an accurate fermi energy, a dense k points with the mesh grid $21 \times 21 \times 1$ was utilized in each static calculation. To calculate the surface state, a slab, exposing (111) plane of the FCC structure, with 54 atom layers (around 60 \AA) and 20 \AA vacuum thickness was used for each material, as shown in Fig.S1(c). In the slab calculation, a $10 \times 10 \times 1$ k points mesh grid for static calculation and $51 \times 51 \times 1$ k points mesh grid for fermi surface calculation were utilized. While calculating the surface state dispersion and fermi surface of YPtBi and LaPtBi, the upmost 9 atom layers which are terminated by Bi(Pb) atoms are considered as surface atoms. Spin-orbit coupling (SOC) was included in all calculations.

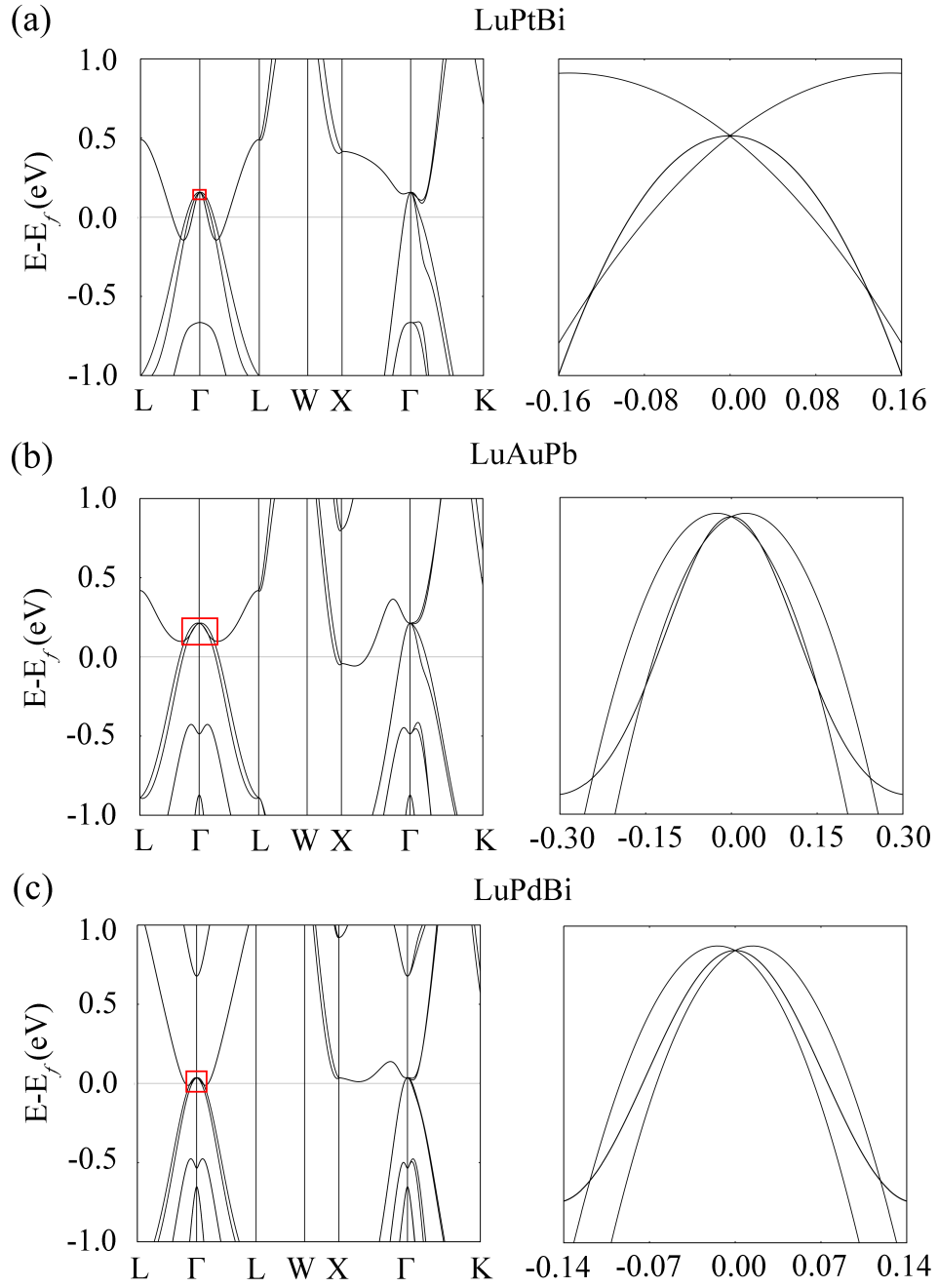


FIG. S2. Bulk band structures with triply degenerate band crossing. All these three materials are long-TP materials, holding different numbers of TPs: (a) LuPtBi with 6 TPs along the C3 axis, (b) LuAuPb with 6 TPs, and (c) LuPdBi with 2 TPs. To make it more clear, the band dispersion along the C3 axis in the red boxes are zoomed-in and shown in corresponding right panels.

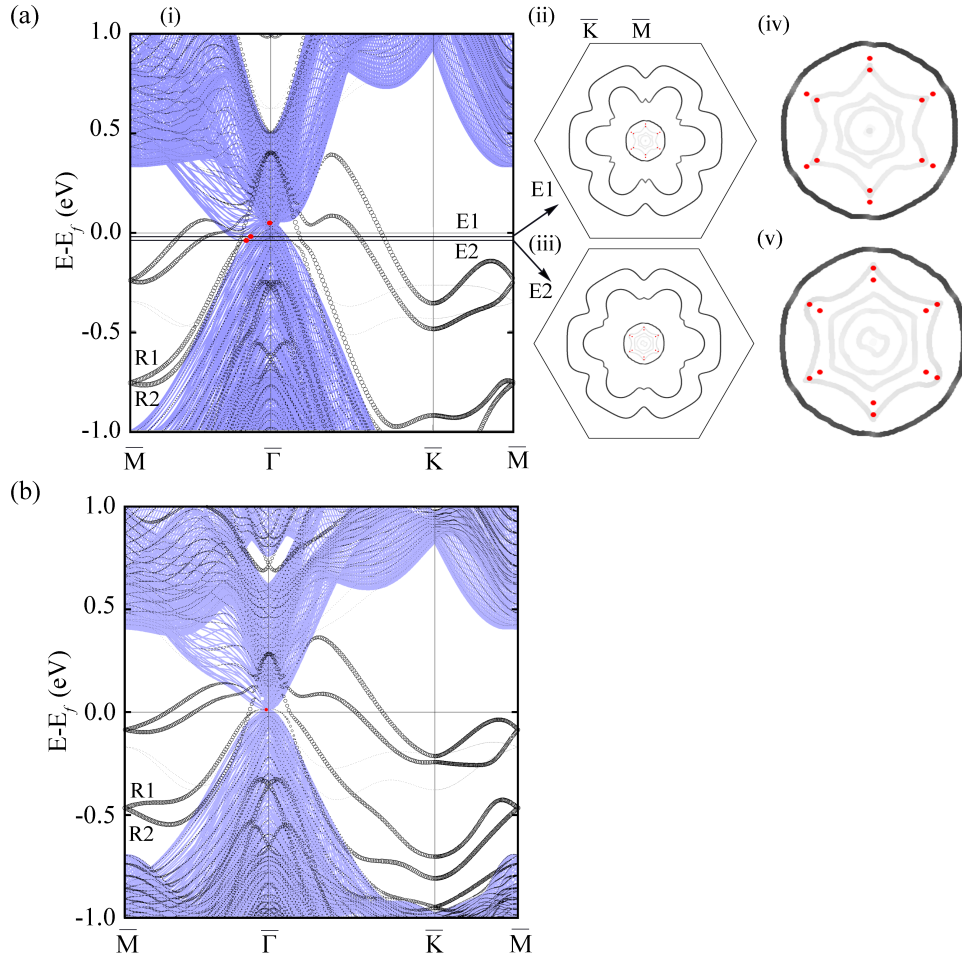


FIG. S3. The DFT surface band structures calculated on slab models for (a) YPtBi and (b) LaPtBi. The size of white circles represent the surface contribution and thus large circles indicate the surface states. The bulk bands are indicated by blue curves as a background, where the triple point is indicated by the red point. (ii) and (iii), Fermi surfaces corresponding to energy E1 (crossing the triple point) and E2 (crossing the triple point), respectively. (iv) and (v), The zoom-in of the inner Fermi ring of (ii) and (iii), respectively. For YPtBi, at each energy level Fermi arcs connect 6 TPs and form a hexagon-like Fermi surface, consistent with the Kane model. In both cases, the Rashba-like surface states R1 and R2 exist. The R1 bands end at the TPs after crossing the R2 band along $\bar{M} - \bar{\Gamma}$, similar to that of GdPtBi Fig.3(c).

-
- * binghai.yan@weizmann.ac.il
- ¹ P. C. Canfield, J. Thompson, W. Beyermann, A. Lacerda, M. Hundley, E. Peterson, Z. Fisk, and H. Ott, *Journal of applied physics* **70**, 5800 (1991).
 - ² M. I. Aroyo, J. M. Perez-Mato, C. Capillas, E. Kroumova, S. Ivantchev, G. Madariaga, A. Kirov, and H. Wondratschek, *Zeitschrift für Kristallographie-Crystalline Materials* **221**, 15 (2006).
 - ³ R. Winkler, S. Papadakis, E. De Poortere, and M. Shayegan, *Spin-Orbit Coupling in Two-Dimensional Electron and Hole Systems*, Vol. 41 (Springer, 2003).
 - ⁴ H. Lin, L. A. Wray, Y. Xia, S. Xu, S. Jia, R. J. Cava, A. Bansil, and M. Z. Hasan, *Nature materials* **9**, 546 (2010).
 - ⁵ S. Chadov, X. Qi, J. Kübler, G. H. Fecher, C. Felser, and S. C. Zhang, *Nature materials* **9**, 541 (2010).
 - ⁶ D. Xiao, Y. Yao, W. Feng, J. Wen, W. Zhu, X.-Q. Chen, G. M. Stocks, and Z. Zhang, *Phys. Rev. Lett.* **105**, 096404 (2010).
 - ⁷ W. Al-Sawai, H. Lin, R. S. Markiewicz, L. A. Wray, Y. Xia, S.-Y. Xu, M. Z. Hasan, and A. Bansil, *Phys. Rev. B* **82**, 125208 (2010).
 - ⁸ Z. Zhu, G. W. Winkler, Q. Wu, J. Li, and A. A. Soluyanov, *Phys. Rev. X* **6**, 031003 (2016).
 - ⁹ G. Burns, *Introduction to group theory with applications: materials science and technology* (Academic Press, 2014).
 - ¹⁰ J. P. Perdew, K. Burke, and M. Ernzerhof, *Phys. Rev. Lett.* **77**, 3865 (1996).
 - ¹¹ G. Kresse and J. Furthmüller, *Comp. Mater. Sci.* **6**, 15 (1996).

5.5 Paper IV: Quantum oscillations in the type-II Dirac semi-metal candidate PtSe₂

The last publication presents the collaboration work with Philip's group who did the experimental part. PtSe₂ has been proved to host type-II Dirac fermions both by the ab-initio calculations [74] and the ARPES measurements [75, 76]. Therefore, in our paper, instead of concentrating on the topological properties of PtSe₂, we mainly focus on its electronic structure near the Fermi level.

We have first calculated the band dispersion and 3D Fermi surfaces of PtSe₂. The results showed that two type-II Dirac fermions exist on the C_{3v} axis with the energy of 1.3 eV below the Fermi energy as shown in Fig. 1a in **Paper IV**. Then the quantum oscillation frequencies, which are proportional to the extreme k-space areas of the Fermi surfaces along certain directions, are calculated and experimentally measured. The experimental and calculated values match quite well, confirming the correctness of band structure calculations and the existence of the Dirac cones.

It is interesting to compare the hexagonal WC-structure materials aforementioned with the hexagonal PtSe₂ here, since both of them have C_{3v} symmetry. However, in distinguished with the WC-structure materials whose inversion symmetry is broken, both the time reversal and the inversion symmetries are present in PtSe₂, resulting in the topological difference between those two types of materials. In principle, the Dirac points in PtSe₂ can split to Weyl points by breaking either the time reversal symmetry or inversion symmetry, or to TPFs when inversion symmetry is broken. Therefore, PtSe₂ is a good candidate for studying the topological phase transition under different conditions like magnetic doping.



PAPER

Quantum oscillations in the type-II Dirac semi-metal candidate
PtSe₂

OPEN ACCESS

RECEIVED
16 November 2017REVISED
6 February 2018ACCEPTED FOR PUBLICATION
1 March 2018PUBLISHED
12 April 2018

Original content from this
work may be used under
the terms of the [Creative
Commons Attribution 3.0
licence](#).

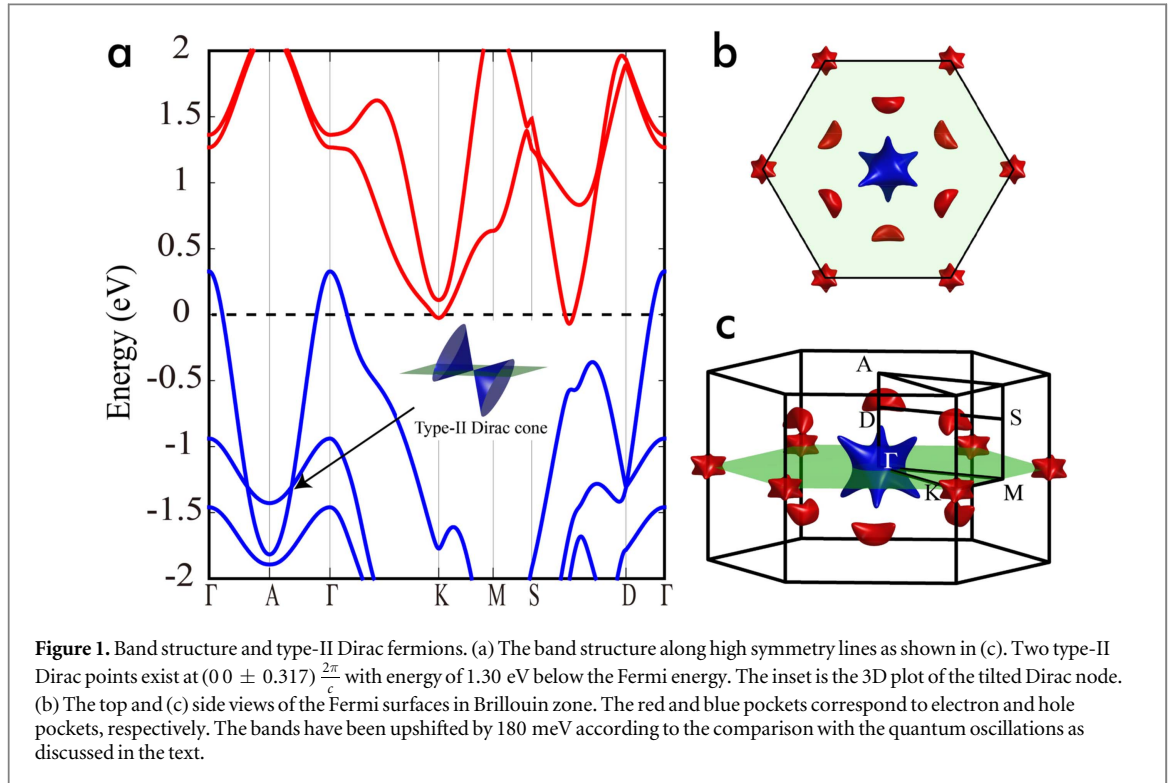
Any further distribution of
this work must maintain
attribution to the
author(s) and the title of
the work, journal citation
and DOI.

Hao Yang^{1,2}, Marcus Schmidt¹, Vicky Süß¹, Mun Chan³, Fedor F Balakirev³, Ross D McDonald³,
Stuart S P Parkin², Claudia Felser¹, Binghai Yan^{1,4,5} and Philip J W Moll^{1,5} ¹ Max-Planck-Institut für Chemische Physik von Festkörpern, D-01187 Dresden, Germany² Max-Planck-Institut für Mikrostrukturphysik, D-06120 Halle, Germany³ National High Magnetic Field Laboratory, LANL, MS-E536, Los Alamos, NM 87545, United States of America⁴ Department of Condensed Matter Physics, Weizmann Institute of Science, Rehovot, 7610001, Israel⁵ Authors to whom any correspondence should be addressed.E-mail: Binghai.Yan@weizmann.ac.il and Philip.moll@cpfs.mpg.de**Keywords:** Dirac-fermion, transition-metal dichalcogenide, focused ion beam, quantum oscillations, Fermi surface**Abstract**

Three-dimensional topological semi-metals carry quasiparticle states that mimic massless relativistic Dirac fermions, elusive particles that have never been observed in nature. As they appear in the solid body, they are not bound to the usual symmetries of space-time and thus new types of fermionic excitations that explicitly violate Lorentz-invariance have been proposed, the so-called type-II Dirac fermions. We investigate the electronic spectrum of the transition-metal dichalcogenide PtSe₂ by means of quantum oscillation measurements in fields up to 65 T. The observed Fermi surfaces agree well with the expectations from band structure calculations, that recently predicted a type-II Dirac node to occur in this material. A hole- and an electron-like Fermi surface dominate the semi-metal at the Fermi level. The quasiparticle mass is significantly enhanced over the bare band mass value, likely by phonon renormalization. Our work is consistent with the existence of type-II Dirac nodes in PtSe₂, yet the Dirac node is too far below the Fermi level to support free Dirac-fermion excitations.

Introduction

Band structure theory is one of the most successful concepts in condensed matter physics, classifying solids into metals and insulators. One of the key ongoing advances in our understanding of electronic materials is the increasing focus on topological aspects of the electronic bands in the solid [1, 2]. Topological metals and semi-metals are characterized by robust band crossing points near the Fermi energy, leading to linear electronic dispersions in the vicinity of these crossing points. This linear electronic dispersion can be mapped onto the Weyl- and Dirac-Hamiltonian [3, 4] describing massless relativistic fermions. While these have never been observed as elementary particles, in topological materials low energy quasiparticles emerge and mimic these elusive relativistic fermions. Their detection as quasiparticles in condensed matter systems has initiated a fruitful transfer of ideas between these fields of physics, with concepts envisioned for high energy physics now appearing in solids [5, 6]. Recently it was shown that the generalization of the Dirac equation to condensed matter systems also has solutions that cannot appear in elementary particles as they are forbidden by Lorentz symmetry [7]. In general, the dispersion relation in a solid arises due to the interaction of the electrons with the atoms in a periodic crystal, and thereby some of the symmetries of electronic behavior in free space are broken. One example is the appearance of the quasi-momentum of electrons as the translational invariance of free space is replaced by the discrete translation symmetry of the crystal lattice. Similarly in the case of quasiparticles following a massless relativistic dispersion, the rest frame of the crystal lattice defines an absolute frame of reference, and hence Lorentz-invariance is not a symmetry of the electronic system in the solid. This has intriguing consequences: some solutions to the Dirac equation are inherently non-Lorentz-invariant and thus are not allowed for elementary particles. Without Lorentz invariance, these may appear in the solid and new types of relativistic



quasiparticles with a positive Fermi velocity in some, but a negative in other crystal directions are predicted. These are called type-II Dirac nodes that correspond to a singular node at the touching point of an electron- and a hole-type Fermi surface, in contrast to the usual type-I Dirac fermions described by a single definite cone.

The non-degenerate analog, the type-II Weyl semi-metal [7, 8], has been predicted in transition-metal dichalcogenides such as MoTe_2 . Soon after, these predictions were experimentally verified by imaging the topologically protected Fermi arc surface states via angle-resolved photoemission spectroscopy (ARPES) [9–11]. Recently, a type-II Dirac semi-metal state has been predicted in PtSe_2 [12] and successively observed by ARPES studies [13, 14]. The main aim of the present work is to experimentally investigate its electronic structure at the Fermi level via quantum oscillations. In addition to its proposed topological character, PtSe_2 is a layered material that has recently attracted attention for its potential use in electronic applications for which a detailed knowledge of the band structure is essential. It can be synthesized in high quality thin film form [15] or as nanocrystallites [16, 17], and it has been proposed as a candidate material for spintronics [18] or electronic applications due to its combination of high electronic mobility, sizeable band-gap and strong spin-orbit coupling.

Band structure calculations

In order to have a direct visualization of the Fermi surface, we have performed first principle calculation using the Vienna *ab initio* simulation package [19]. An $8 \times 8 \times 8$ gamma centered grid of k points and a 520 eV plane-wave energy cutoff are adopted for the self-consistent field calculations. The Perdew–Burke–Ernzerhof [20] pseudopotentials with the generalized gradient approximation (GGA) was used in our calculation. In all the calculation, spin orbital coupling are included. We first obtained the band structure of PtSe_2 along high symmetry lines as shown in figure 1(a). Along the Γ – A direction, a Dirac-type band crossing is found to reside at 1.30 eV below the Fermi energy at the D point $(000.317) \frac{2\pi}{c}$, where c is the lattice parameter along z direction. The Dirac node (point D) tilts strongly along k_z (the Γ – D – A line) but only weakly in the k_x – k_y plane (e.g. the S – D line). Our result is fully consistent with [12], predicting a type-II Dirac node as shown in the inset of figure 1(a). As the Dirac node is far below the Fermi level, Dirac quasiparticle excitations are not expected to occur and the transport properties are dominated by non-topological electrons.

To compare these calculations to quantum oscillations arising from these charge carriers at the Fermi level, we have calculated the three-dimensional Fermi surfaces of bulk PtSe_2 . The Fermi surface consists of three main pockets, one hole-like and two electron-like. The shape of the hole pocket resembles an octahedron, shown in blue in figure 1. The electron bands exhibit two types of Fermi pockets (colored red in figure 1): an octahedron-like electron pocket located around the K point and six crescent-like electron pockets located between D and S points. Both the electron pockets and the hole pocket show three-fold rotation symmetry and inversion

symmetry around the Γ -point, consistent with the symmetry of the crystal structure. Since GGA usually underestimates the gap between conduction and valence bands, we should note that we applied an upshift of 0.18 eV for all conduction bands in figure 1. As discussed below, this constant shift matches the entire angle dependence of the quantum oscillation spectrum well.

Device fabrication

To meaningfully analyze quantum oscillations in metals with non-spherical Fermi surfaces, it is critical to measure an individual single crystal. Highest quality PtSe₂ is grown by chemical vapor transport. Yet the resulting crystals often suffer from intergrowth of smaller crystallites, rendering the sample effectively polycrystalline. Therefore we use focused ion beam (FIB) machining to selectively fabricate transport devices from pristine regions of the crystal, to access its true single crystal physics.

The starting material for the microstructure fabrication are conventionally grown single crystals of PtSe₂. Our single crystal growth procedure follows previous successful synthesis attempts by chemical vapor transport [21] in the system Pt/Sn/(S, Se)₂ using iodine as transport agent. The precursor material PtSe₂ was synthesized in a first step by direct reaction of the elements platinum (Alfa Aesar 99.95%) and selenium (Alfa Aesar 99.999%) at 500 °C and 650 °C in evacuated fused silica tubes for 5 d. Starting from this microcrystalline powder, PtSe₂ crystallized by a chemical transport reaction in a temperature gradient from 850 °C (source) to 750 °C (sink), and a transport agent concentration of 6 mg cm⁻³ iodine (Alfa Aesar 99,998%). The resulting crystals are thin platelets, with typical sizes of ~200 μm in-plane and <10 μm perpendicular to the plane. The hexagonal crystal structure is well reflected in the morphology of the platelets. Selected crystals were characterized by EDXS, x-ray powder, and x-ray single crystal diffraction.

The crystallites were patterned using FIB micromachining into meandering bar shapes that are ideally suited for precision resistance measurements. A typical microstructure is shown in figure 2(a). The crystals were patterned using a Ga-ion beam at incidence energies of 60 keV and with currents between 1 and 3 nA. Electrical contacts were made by evaporating gold electrodes onto the crystal (colored yellow in figure 2(a)). Two crystals have been patterned into similar shapes and fully characterized, including the quantum oscillation measurements in high fields, and all results were in quantitative agreement.

This approach has two main advantages for the present experiment, sample optimization for pulsed field experiments and the suppression of artefacts due to crystal defects. The shape of the crystal can be precisely trimmed to optimize the total device resistance given the materials natural specific resistivity. Thereby the device resistance can be set to an optimal value in the 10–100 Ω range for pulsed magnetic field measurements. At lower resistance, the accordingly smaller signal-to-noise ratio impedes the measurement of the oscillatory amplitude of the magnetoresistance. At higher resistance, the larger LRC-time constant of the measurement circuit would require to reduce the frequency of the applied ac-current. Yet lower measurement frequencies come close to the typical noise spectrum of a pulsed magnet which extends into the 10–20 kHz range. By proper design of the microstructure, these issues can be avoided and high quality data obtained from a metal regardless of its resistivity. This approach has proven to be a reliable method to fabricate crystalline samples for transport measurements in high magnetic fields in a large variety of different compounds [22, 23]. In addition, the microstructuring also allows to specifically probe the most pristine region of the crystal and to exclude damaged regions from influencing the measurement. The crystal in figure 2(a) depicts such a scenario: a secondary crystallite grew in into the bottom half of the otherwise perfectly regular hexagonal plate. By using the sub-micron precision of the FIB cutting, the active device area can be patterned into the pristine face of a crystal thus completely bypassing the intergrowth regions.

The temperature dependence in zero magnetic field is shown in figure 2(b). PtSe₂ is found to be a reasonably good metal with a resistivity of 130 $\mu\Omega$ cm at room temperature and 25 $\mu\Omega$ cm at 2 K. At lowest temperatures, we consistently observe a slight upturn of the resistance in all fabricated microstructures. This is directly related to a weak negative magnetoresistance at very low fields before the large positive magnetoresistance is observed (inset figure 3(a)). Given the topologically trivial nature of the charge carriers at the Fermi level and the isotropic behavior upon changing the angle of the magnetic field with respect to the current path, a topological origin related to the chiral anomaly can be clearly excluded [24]. A likely explanation is weak localization, however no such behavior was observed in previous studies [17] of the low-temperature resistivity of PtSe₂. Thus it may also be possible that electronic interactions conspire with the lateral finite size confinement in the microstructure to yield positive corrections to the apparent device resistance due to viscous effects in a hydrodynamic picture of electron transport [25–27]. Clearly future experiments quantifying the resistance variation among samples and microstructure dimensions are required to address this question.

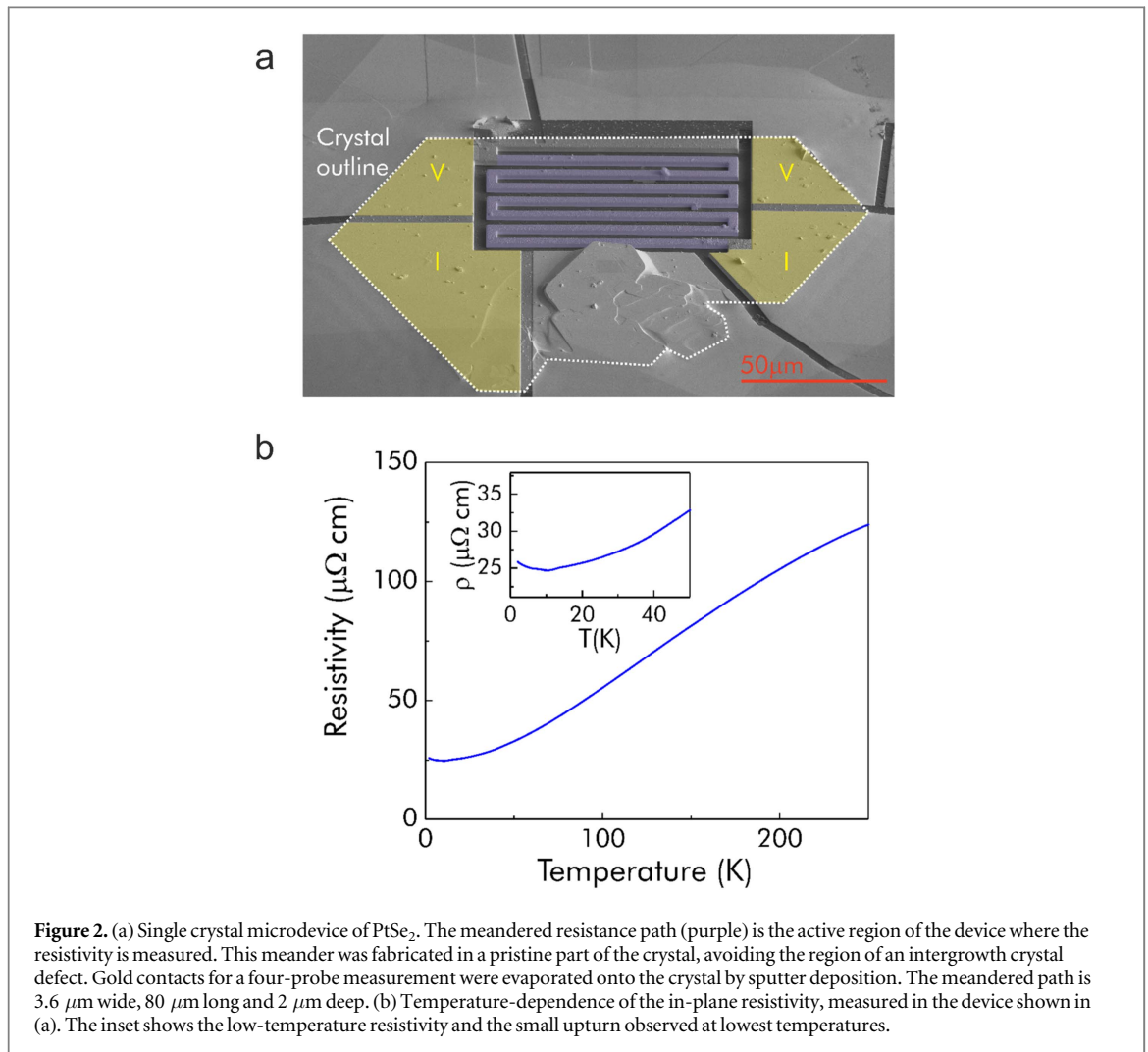


Figure 2. (a) Single crystal microdevice of PtSe₂. The meandered resistance path (purple) is the active region of the device where the resistivity is measured. This meander was fabricated in a pristine part of the crystal, avoiding the region of an intergrowth crystal defect. Gold contacts for a four-probe measurement were evaporated onto the crystal by sputter deposition. The meandered path is 3.6 μm wide, 80 μm long and 2 μm deep. (b) Temperature-dependence of the in-plane resistivity, measured in the device shown in (a). The inset shows the low-temperature resistivity and the small upturn observed at lowest temperatures.

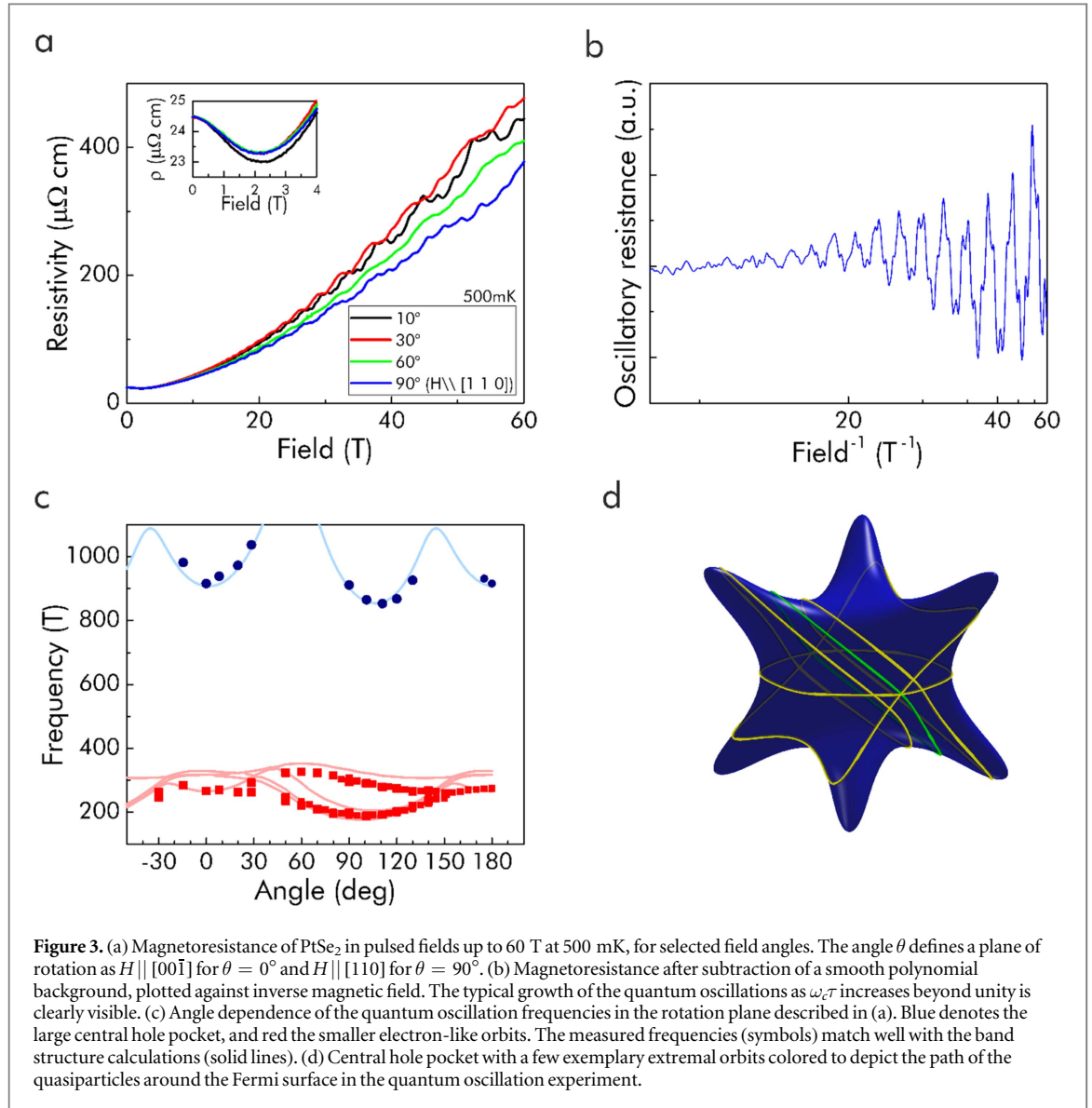
Pulsed field magnetoresistance

Angle dependent magnetoresistance measurements were performed at the National High Magnetic Field Laboratory in Los Alamos, using a 65 T short pulse magnet. These high-strength copper solenoids deliver magnetic field pulses with a characteristic time of 8 ms rise time to peak field and a slow fall time from peak field to zero of 100 ms. The magnetoresistance is measured by applying an ac-current of 380 μA at 297.5 kHz to the devices and detecting the voltage response via a lock-in procedure.

The magnetoresistance of PtSe₂ at 500 mK increases by a factor of 20 up to 60 T. The family of transition-metal dichalcogenides (TMD) exhibits a wide spectrum of behaviors in high magnetic fields. As in all semi-metals, the magnetoresistance is determined by the Fermi surface shape as well as the degree of compensation between electrons and holes [28]. Some tellurides, such as WTe₂ [29] or MoTe₂ [30], exhibit very large and non-saturating magnetoresistance, indicating an almost ideal electron–hole compensation. The electronic structure of PtSe₂ is clearly dominated by the central hole band, and the comparatively lower magnetoresistance is expected in light of the poorer electron–hole compensation. The overall magnetoresistance is found to be essentially independent of the angle of the magnetic field to the crystal (figure 3(a)), where 0° corresponds to fields along the [00 $\bar{1}$] and 90° along the [110] direction, reflecting the three-dimensional nature of the electronic system.

Fermiology

The magnetoresistance shows pronounced quantum oscillations containing multiple beating frequencies and in general is dominated by two classes of frequencies. The first around 1000 T disperses quickly to higher frequencies upon changing the field angle, indicating a local minimum of the cross-sectional area of this

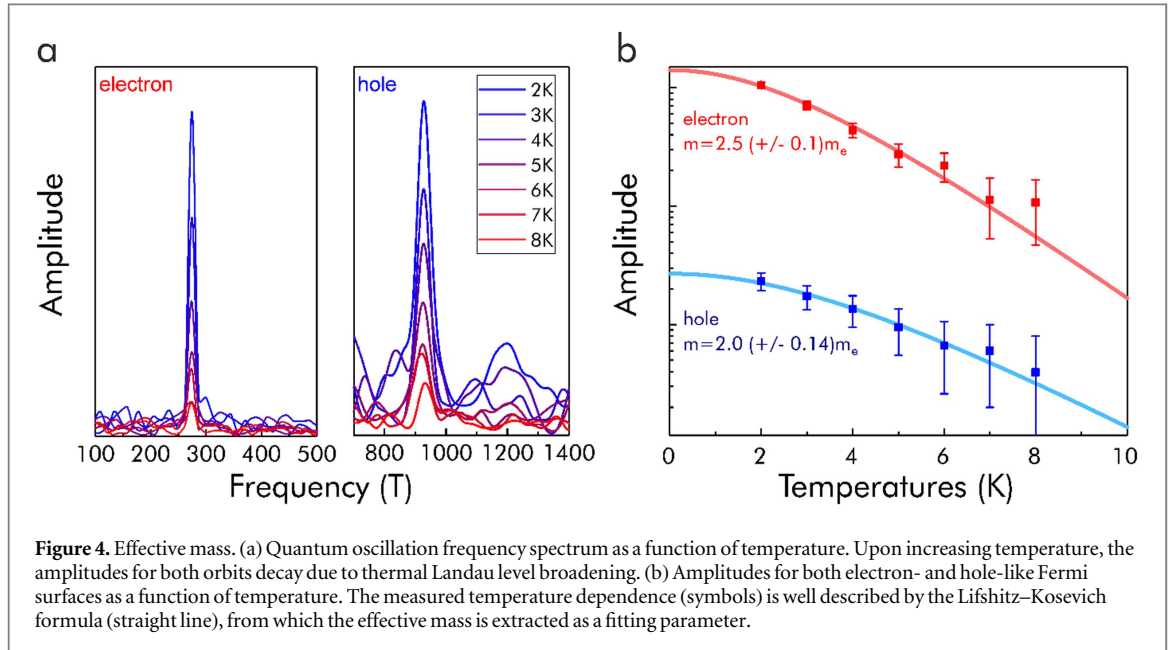


quantum orbit ('neck-frequency'). The second set of frequencies belongs to a weakly dispersive frequency band in the 200–300 T range.

The measured frequencies can be directly compared to the band structure calculations. Each frequency corresponds to a separate quantum orbit around the Fermi surface perpendicular to the magnetic field, where figure 3(d) shows an exemplary orbit on the hole pocket. The frequency F is directly proportional to the extremal k -space area S_k enclosed in the orbit, given by the Onsager relation as $F = (\Phi_0/2\pi^2)S_k$, where $\Phi_0 = h/2e$ is the magnetic flux quantum, e the electron charge and h is the Planck constant. We have calculated the quantum oscillation frequencies of electron pockets and hole pocket with the magnetic field rotated from $[00\bar{1}]$ direction to $[110]$ direction. Figure 3(c) displayed both the experimental and calculated quantum oscillation frequencies as a function of the angle between magnetic field and $[00\bar{1}]$ direction. The absence of a mirror plane symmetry perpendicular to the c -direction in the crystal is directly reflected by the lack of symmetry of the quantum oscillation frequency around 90° . The comparison to the band structure calculations allows us to identify the two types of frequencies as orbits on separate Fermi surface sheets. The large frequency belongs to the orbit around a star-shaped hole pocket centered in the Brillouin zone, while the low frequencies belong to the comparatively smaller electron-like Fermi surfaces.

Effective mass enhancement

Quantum oscillations also provide a direct measurement of the quasiparticle effective mass [31]. The temperature dependence of the amplitudes $A(T)$ due to the thermal broadening of the Fermi–Dirac distribution is well described by the Lifshitz–Kosevich formula as $A(T)/A_0 = X/\sinh(X)$, where $X = 2\pi^2k_B T/\hbar\omega_c$. Here, the cyclotron frequency $\omega_c = \frac{eB}{m^*}$ contains only the quasiparticle effective mass m^* as



an unknown fitting parameter to the data (figure 4). To extract the amplitude from the raw data, the non-oscillatory part of the magnetoresistance was fitted to a 3rd degree polynomial spline and subtracted from the data, to yield the purely oscillatory component (figure 3(b)). The frequency spectrum in figure 4(a) was obtained by standard Fourier analysis, and the peak height estimated above the experimental noise floor. Both pockets show a similar effective mass, with $2.0(\pm 0.14)m_e$ for the hole and $2.5(\pm 0.1)m_e$ for the slightly heavier electron pocket. Here m_e denotes the mass of the free electron. This can be directly compared to the effective mass calculated from the band structure, $m_{\text{band}}(k) = \hbar k/v_F$, which in general is k -dependent. The cyclotron effective mass measured in quantum oscillation experiments is the average effective mass around the quasiparticle orbit, $m_{\text{band}}^* = \frac{1}{L} \oint m_{\text{band}}(\mathbf{k}) d\mathbf{k}$, where L denotes the k -space length of the orbit. The cyclotron effective mass can also be expressed as the change of the k -space area A enclosed by the orbit upon changing the energy E around the Fermi energy, E_F , as $m_{\text{band}}^* = \frac{\hbar^2}{2\pi} \left(\frac{dA}{dE} \right)^{-1}_{|E_F}$. The latter can be more conveniently calculated from the band structure $E(k)$. For the orbits in the experimental situation of the temperature dependent measurements, $H \parallel [00\bar{1}]$, a cyclotron mass of $0.4m_e$ is calculated for the hole band, and $0.35m_e$ for the star-shaped electron pocket.

Given the good agreement of the calculated band structure with the measured Fermi surface topology, the most likely explanation for such a sizable disagreement is mass renormalization. When electrons in a solid are coupled to a bosonic field with a strength λ , the quasiparticle dispersion is renormalized as $m^* = (1 + \lambda)m_{\text{band}}^*$. In absence of magnetism in PtSe₂, the prime candidate for the origin of the sizable mass enhancement $\lambda \sim 5.5$ is strong electron-phonon coupling [32]. This picture is further supported by recent ARPES experiments finding good agreement between band structure calculations and photoemission spectra over the entire band, thus excluding bandwidth renormalizations due to correlations [13, 14].

Conclusions

The electronic system of the semi-metal PtSe₂ is dominated by a larger hole pocket and two small electron pockets, and our results experimentally confirm the band structure calculations of [12]. Thereby our quantum oscillation study provides experimental support for calculated band structures in the TMD that host type-II Dirac fermions. Yet the Dirac node is far below the chemical potential and thus no topological excitations appear in the material. The conductivity and materials properties are therefore dominated by non-topological charge carriers, and promoting the type-II Dirac fermions to the Fermi level is the next important challenge to study their physics and application prospects. Usual methods such as charge doping or gating techniques do not appear as a viable route, given the large energy difference of 1.3 eV between the Dirac node and the Fermi level in PtSe₂. Yet it may be possible to find materials in which they reside closer to the Fermi level within the class of TMD layered conductors. Also, recently type-II Dirac fermions closer to the Fermi energy (200–300 meV below E_F) were predicted in Heusler compounds [33]. The observed enhancement of the quasiparticle effective mass suggests a strong electron-phonon interaction in PtSe₂. The observation of mass enhancement is consistent with the appearance of low-temperature superconductivity in this materials class, such as in the related tellurides

WTe₂ ($T_c \sim 7$ K under pressure [34]) and MoTe₂ ($T_c \sim 0.1$ K at ambient pressure, 8.2 K under pressure [35]). This appearance of significant mass renormalization in a topologically non-trivial band structure is of particular interest for the ongoing search for strongly correlated topological materials.

Acknowledgments

We thank Horst Borrmann for the careful crystallographic analysis of the crystals. BY acknowledges the support by the Ruth and Herman Albert Scholars Program for New Scientists in Weizmann Institute of Science, Israel and by a Grant from the GIF, the German-Israeli Foundation for Scientific Research and Development. A portion of this work was completed at the National High Magnetic Field Laboratory's Pulsed Field Facility at Los Alamos National Laboratory, which is supported through National Science Foundation Cooperative Agreement No. DMR 1157490, the Department of Energy and the State of Florida. RDM acknowledges support from LANL LDRD-DR20160085 'Topology and strong correlations'. This project was supported by the European Research Council (ERC) under the European Union's Horizon 2020 research and innovation programme (GA No. 715730).

ORCID iDs

Philip J W Moll  <https://orcid.org/0000-0002-7616-5886>

References

- [1] Wehling T O, Black-Schaffer A M and Balatsky A V 2014 Dirac materials *Adv. Phys.* **63** 1–76
- [2] Yan B and Felser C 2017 Topological Materials: Weyl Semimetals *Annu. Rev. Condens. Matter Phys.* **8** 337–54
- [3] Armitage N P, Mele E J and Vishwanath A 2018 Weyl and Dirac semimetals in three-dimensional solids *Rev. Mod. Phys.* **90** 15001
- [4] Novoselov K S et al 2005 Two-dimensional gas of massless Dirac fermions in graphene *Nature* **438** 197–200
- [5] Dean C R et al 2012 Hofstadter's butterfly in moire superlattices: a fractal quantum Hall effect *Nature* **497** 598–602
- [6] Katsnelson M I, Novoselov K S and Geim A K 2006 Chiral tunneling and the Klein paradox in graphene *Nat. Phys.* **2** 620–5
- [7] Soluyanov A A et al 2015 Type-II Weyl semimetals *Nature* **527** 495–8
- [8] Sun Y, Wu S C, Ali M N, Felser C and Yan B 2015 Prediction of Weyl semimetal in orthorhombic MoTe₂ *Phys. Rev. B* **92** 161107(R)
- [9] Huang L et al 2016 Spectroscopic evidence for a type-II Weyl semimetallic state in MoTe₂ *Nat. Mater.* **15** 1155–60
- [10] Deng K et al 2016 Experimental observation of topological Fermi arcs in type-II Weyl semimetal MoTe₂ *Nat. Phys.* **12** 1105–11
- [11] Jiang J et al 2016 Signature of type-II Weyl semimetal phase in MoTe₂ *Nat. Commun.* **8** 13973
- [12] Huang H, Zhou S and Duan W 2016 Type-II Dirac fermions in the PtSe₂ class of transition metal dichalcogenides *Phys. Rev. B* **94** 121117
- [13] Li Y et al 2017 Topological origin of the type-II Dirac fermions in PtSe₂ *Phys. Rev. Mater.* **1** 74202
- [14] Zhang K et al 2017 Experimental evidence for type-II Dirac semimetal in PtSe₂ *Phys. Rev. B* **96** 125102
- [15] Yim C et al 2016 High-performance hybrid electronic devices from layered PtSe₂ films grown at low temperature *ACS Nano* **10** 9550–8
- [16] Wang Z, Li Q, Besenbacher F and Dong M 2016 Facile synthesis of single crystal PtSe₂ nanosheets for nanoscale electronics *Adv. Mater.* **28** 10224–9
- [17] Li Z et al 2017 Anomalous magnetotransport behaviors in PtSe₂ microflakes *J. Phys.: Condens. Matter* **29** 23LT01
- [18] Yao W et al 2017 Direct observation of spin-layer locking by local Rashba effect in monolayer semiconducting PtSe₂ film *Nat. Commun.* **8** 14216
- [19] Kresse G and Furthmüller J 1996 Efficiency of *ab-initio* total energy calculations for metals and semiconductors using a plane-wave basis set *Comput. Mater. Sci.* **6** 15–50
- [20] Perdew J P, Burke K and Ernzerhof M 1996 Generalized gradient approximation made simple *Phys. Rev. Lett.* **77** 3865–8
- [21] Tomm Y, Fiechter S, Diener K and Tributsch H 1997 Phase formation in the system Pt-Sn-(S, Se)₂ and crystal growth by chemical vapor transport *Int. Phys. Conf. Ser. No 152 Sect. A, Int. Conf. Ternary Multinary Compd.* pp 167–70
- [22] Jaroszynski J et al 2008 Upper critical fields and thermally-activated transport of Nd(O_{0.7}F_{0.3})FeAs single crystal *Phys. Rev. B* **78** 174523
- [23] Moll P J W, Zhu X, Cheng P, Wen H-H and Batlogg B 2014 Intrinsic Josephson junctions in the iron-based multi-band superconductor (V₂Sr₄O₆)Fe₂As₂ *Nat. Phys.* **10** 644–7
- [24] Xiong J et al 2015 Evidence for the chiral anomaly in the Dirac semimetal Na₃Bi *Science* **350** 413
- [25] Alekseev P S 2016 Negative magnetoresistance in viscous flow of two-dimensional electrons *Phys. Rev. Lett.* **117** 166601
- [26] Scaffidi T, Nandi N, Schmidt B, Mackenzie A P and Moore J E 2017 Hydrodynamic electron flow and hall viscosity *Phys. Rev. Lett.* **118** 226601
- [27] Moll P J W, Kushwaha P, Nandi N, Schmidt B and Mackenzie A P 2016 Evidence for hydrodynamic electron flow in PdCoO₂ *Science* **351** 1061–4
- [28] Pippard A B 1989 *Magnetoresistance in Metals* (Cambridge: Cambridge University Press)
- [29] Ali M N et al 2014 Large non-saturating magnetoresistance in WTe₂ *Nature* **514** 205–8
- [30] Chen F C et al 2016 Extremely large magnetoresistance in the type-II Weyl semimetal MoTe₂ *Phys. Rev. B* **94** 235154
- [31] Shoenberg D 1984 *Magnetic Oscillations in Metals* (Cambridge: Cambridge University Press)
- [32] Chakraborty B et al 2012 Symmetry-dependent phonon renormalization in monolayer MoS₂ transistor *Phys. Rev. B* **85** 161403(R)
- [33] Guo P J, Yang H C, Liu K and Lu Z Y 2017 Type-II Dirac semimetals in the YPd₂Sn class *Phys. Rev. B* **95** 155112
- [34] Pan X-C et al 2015 Pressure-driven dome-shaped superconductivity and electronic structural evolution in tungsten ditelluride *Nat. Commun.* **6** 7805
- [35] Qi Y et al 2016 Superconductivity in Weyl semimetal candidate MoTe₂ *Nat. Commun.* **7** 11038

Chapter 6

Summary

In the course of this thesis, fundamental topological and electronic properties of topological metals/semimetals along with the associated transport properties were theoretically studied. Three types of quasiparticles which can be distinguished according to the symmetry of the host materials are investigated. The wavefunctions and Hamiltonian of each system were extracted from the *ab-initio* calculations using the software package VASP and then projected to the Wannier functions. The topological invariants were calculated within the framework of the Berry curvature concept and revealed that the Weyl points and TPFs are topologically nontrivial. The topological properties of these two quasiparticles have been further verified through the topological surface states calculated using either the half-infinite model or slab model. As for Dirac points in PtSe₂, although the topological invariant has not been found yet, the surface states have been observed and are robust against the perturbations preserving the symmetry [74]. Being a cumulative dissertation, this thesis includes results published in peer-reviewed journals.

The first publication showed the possibility to find Weyl points in the chiral AFM ordered materials Mn₃Ge and Mn₃Sn. Those Weyl points appear in pairs and are distributed in accordance with the symmetry of the magnetic lattice. The Weyl points in each pair are separated by the M_y mirror plane and have opposite chirality characterized by the

all-in or all-out Berry curvature texture. For both compounds, Fermi arcs connecting two opposite Weyl points were found and require further experimental verification.

The second publication is also related to the Weyl points in the sense that it reveals that the origin of the intrinsic AHC and SHC are not exactly from the Weyl points. For the six studied materials, all of them showed strong anisotropic AHC and SHC, which are closely related to the symmetry of the AFM Kagome lattice. It is interesting to note that the electronic transport properties are not simply proportional to the strength or the trend of the SOC. Although we didn't search for the Weyl points in the other four materials, we have a strong indication from previous works that they can host Weyl points, due to the congruency of magnetic structures.

In the second study, which corresponds to the third publication, the existence of TPFs in the cubic structural materials has been examined via *ab-initio* calculations and the $\mathbf{k} \cdot \mathbf{p}$ Kane model. We searched more than thirty half-Heusler compounds and found six to be TPTMs and have odd pairs of TPFs, some of which are located at large momenta positions in first BZ and can be experimentally measured. These TPFs are connected by nodal lines in the bulk band structures and Fermi arcs in the half-infinite surface band structures.

Finally, in the last publication, the electronic structure at the Fermi level of Dirac semimetal PtSe₂ was calculated and experimentally measured. The quantum oscillation experiments and the simulations indicate that both the hole and electron pockets participate the transport and specifically they contribute to the magnetoresistance. The hole pocket, which is located near the Γ point and has Octahedral shape, contributes to the high-frequency branch. The electron pockets, on the other hand, exhibit two types of Fermi pockets: an octahedron-like electron pocket located around the K point and six crescent-like electron pockets located between D and S. All of them contribute to the low-frequency branches. The mismatch between the calculated and measured mass of electrons and holes suggests a strong electron-phonon interaction in PtSe₂.

In summary, three types of quasiparticles have been found in the aforementioned materials and related topological and electronic properties were investigated in this work. Since the topological materials and the quasiparticles have many practical applications, a more detailed investigation would be beneficial to further the understanding of this fundamental research. For example, in our work, there are still several issues to be solved, such as the experimental observation of topological surface states in the Weyl metals and TPTMs, the verification of SHE in the Weyl metals, and the tuning of Dirac points' energy in PtSe₂ for the measurement.

Bibliography

- [1] D. J. Thouless, M. Kohmoto, M. P. Nightingale, and M. den Nijs, “Quantized hall conductance in a two-dimensional periodic potential,” *Phys. Rev. Lett.*, vol. 49, 1982.
- [2] K. v. Klitzing, G. Dorda, and M. Pepper, “New method for high-accuracy determination of the fine-structure constant based on quantized hall resistance,” *Phys. Rev. Lett.*, vol. 45, 1980.
- [3] R. B. Laughlin, “Quantized hall conductivity in two dimensions,” *Phys. Rev. B*, vol. 23, 1981.
- [4] S. M. Bhattacharjee, M. Mj, and A. Bandyopadhyay, *Topology and Condensed Matter Physics*. 2017.
- [5] D. Xiao, M.-C. Chang, and Q. Niu, “Berry phase effects on electronic properties,” *Rev. Mod. Phys.*, vol. 82, 2010.
- [6] X.-L. Qi and S.-C. Zhang, “Topological insulators and superconductors,” *Rev. Mod. Phys.*, vol. 83, 2011.
- [7] M. Z. Hasan and C. L. Kane, “Colloquium: Topological insulators,” *Rev. Mod. Phys.*, vol. 82, 2010.
- [8] C. L. Kane and E. J. Mele, “ Z_2 topological order and the quantum spin hall effect,” *Phys. Rev. Lett.*, vol. 95, 2005.

-
- [9] C. L. Kane and E. J. Mele, “Quantum spin hall effect in graphene,” *Phys. Rev. Lett.*, vol. 95, 2005.
- [10] B. A. Bernevig, T. L. Hughes, and S.-C. Zhang, “Quantum spin hall effect and topological phase transition in hgte quantum wells,” *Science*, vol. 314, 2006.
- [11] L. Fu, C. L. Kane, and E. J. Mele, “Topological insulators in three dimensions,” *Phys. Rev. Lett.*, vol. 98, 2007.
- [12] J. E. Moore and L. Balents, “Topological invariants of time-reversal-invariant band structures,” *Phys. Rev. B*, vol. 75, 2007.
- [13] L. Fu and C. L. Kane, “Topological insulators with inversion symmetry,” *Phys. Rev. B*, vol. 76, 2007.
- [14] Z. K. Liu, B. Zhou, Y. Zhang, Z. J. Wang, H. M. Weng, D. Prabhakaran, S.-K. Mo, Z. X. Shen, Z. Fang, X. Dai, Z. Hussain, and Y. L. Chen, “Discovery of a three-dimensional topological dirac semimetal, na₃bi,” *Science*, vol. 343, 2014.
- [15] Z. Wang, Y. Sun, X.-Q. Chen, C. Franchini, G. Xu, H. Weng, X. Dai, and Z. Fang, “Dirac semimetal and topological phase transitions in A₃bi (a =na, k, rb),” *Phys. Rev. B*, vol. 85, 2012.
- [16] G. E. Volovik, *The Universe in A Helium Droplet*. Clarendon Press, Oxford, 2003.
- [17] X. Wan, A. M. Turner, A. Vishwanath, and S. Y. Savrasov, “Topological semimetal and fermi-arc surface states in the electronic structure of pyrochlore iridates,” *Phys. Rev. B*, vol. 83, 2011.
- [18] L. Balents, “Viewpoint: Weyl electrons kiss,” *Physics*, vol. 4, 2011.
- [19] A. A. Burkov, M. D. Hook, and L. Balents, “Topological nodal semimetals,” *Phys. Rev. B*, vol. 84, 2011.
- [20] P. Hosur and X. L. Qi, “Recent developments in transport phenomena in Weyl semimetals,” *C. R. Physique*, vol. 14, 2013.

-
- [21] O. Vafek and A. Vishwanath, “Dirac Fermions in Solids: From High-T cCuprates and Graphene to Topological Insulators and Weyl Semimetals,” *Annu. Rev. Condens. Matter Phys.*, vol. 5, 2014.
- [22] P. Hohenberg and W. Kohn, “Inhomogeneous electron gas,” *Phys. Rev.*, vol. 136, 1964.
- [23] W. Kohn and L. J. Sham, “Self-consistent equations including exchange and correlation effects,” *Phys. Rev.*, vol. 140, 1965.
- [24] R. J. Elliott, “Theory of the effect of spin-orbit coupling on magnetic resonance in some semiconductors,” *Phys. Rev.*, vol. 96, 1954.
- [25] J. E. Inglesfield and G. A. Benesh, “Surface electronic structure: Embedded self-consistent calculations,” *Phys. Rev. B*, vol. 37, 1988.
- [26] D. Kalkstein and P. Soven, “A green’s function theory of surface states,” *Surface Science*, vol. 26, 1971.
- [27] P. Phariseau, “On the theory of surface states - a green’s function method,” *physica status solidi (b)*, vol. 3, 1963.
- [28] J. M. MacLaren, S. Crampin, D. D. Vvedensky, and J. B. Pendry, “Layer korrington-rostoker technique for surface and interface electronic properties,” *Phys. Rev. B*, vol. 40, 1989.
- [29] H. L. Skriver and N. M. Rosengaard, “Self-consistent green’s-function technique for surfaces and interfaces,” *Phys. Rev. B*, vol. 43, 1991.
- [30] T. Kato, “On the adiabatic theorem of quantum mechanics,” *Journal of the Physical Society of Japan*, vol. 5, 1950.
- [31] “Quantal phase factors accompanying adiabatic changes,” *Proceedings of the Royal Society of London A: Mathematical, Physical and Engineering Sciences*, vol. 392, 1984.

-
- [32] D. J. Thouless, “Quantization of particle transport,” *Phys. Rev. B*, vol. 27, 1983.
- [33] R. Karplus and J. M. Luttinger, “Hall effect in ferromagnetics,” *Phys. Rev.*, vol. 95, 1954.
- [34] “The quantum theory of the electron,” *Proceedings of the Royal Society of London A: Mathematical, Physical and Engineering Sciences*, vol. 117, 1928.
- [35] H. Weyl, “Elektron und gravitation,” *Z. Phys.*, vol. 56, 1929.
- [36] S.-Y. Yang, H. Yang, E. Derunova, S. S. P. Parkin, B. Yan, and M. N. Ali, “Symmetry demanded topological nodal-line materials,” *arXiv:1707.04523*, 2017.
- [37] H. Weng, C. Fang, Z. Fang, B. A. Bernevig, and X. Dai, “Weyl semimetal phase in noncentrosymmetric transition-metal monophosphides,” *Phys. Rev. X*, vol. 5, 2015.
- [38] L. X. Yang, Z. K. Liu, Y. Sun, H. Peng, H. F. Yang, T. Zhang, B. Zhou, Y. Zhang, Y. F. Guo, M. Rahn, D. Prabhakaran, Z. Hussain, S.-K. Mo, C. Felser, B. Yan, and Y. L. Chen, “Weyl semimetal phase in the non-centrosymmetric compound taas,” *Nat. Phys.*, vol. 11, 2015.
- [39] B. Q. Lv, H. M. Weng, B. B. Fu, X. P. Wang, H. Miao, J. Ma, P. Richard, X. C. Huang, L. X. Zhao, G. F. Chen, Z. Fang, X. Dai, T. Qian, and H. Ding, “Experimental discovery of weyl semimetal taas,” *Phys. Rev. X*, vol. 5, 2015.
- [40] B. Q. Lv, N. Xu, H. M. Weng, J. Z. Ma, P. Richard, X. C. Huang, L. X. Zhao, G. F. Chen, C. E. Matt, F. Bisti, V. N. Strocov, J. Mesot, Z. Fang, X. Dai, T. Qian, M. Shi, and H. Ding, “Observation of weyl nodes in taas,” *Nat. Phys.*, vol. 11, 2015.
- [41] S.-Y. Xu, I. Belopolski, D. S. Sanchez, C. Zhang, G. Chang, C. Guo, G. Bian, Z. Yuan, H. Lu, T.-R. Chang, P. P. Shibayev, M. L. Prokopovych, N. Alidoust, H. Zheng, C.-C. Lee, S.-M. Huang, R. Sankar, F. Chou, C.-H. Hsu, H.-T. Jeng, A. Bansil, T. Neupert, V. N. Strocov, H. Lin, S. Jia, and M. Z. Hasan, “Experimental discovery of a topological weyl semimetal state in tap,” *Sci. Adv.*, vol. 1, 2015.

- [42] S.-Y. Xu, N. Alidoust, I. Belopolski, Z. Yuan, G. Bian, T.-R. Chang, H. Zheng, V. N. Strocov, D. S. Sanchez, G. Chang, C. Zhang, D. Mou, Y. Wu, L. Huang, C.-C. Lee, S.-M. Huang, B. Wang, A. Bansil, H.-T. Jeng, T. Neupert, A. Kaminski, H. Lin, S. Jia, and M. Zahid Hasan, “Discovery of a weyl fermion state with fermi arcs in niobium arsenide,” *Nat. Phys.*, vol. 11, 2015.
- [43] A. A. Soluyanov, D. Gresch, Z. Wang, Q. Wu, M. Troyer, X. Dai, and B. A. Bernevig, “Type-II Weyl semimetals,” *Nature*, vol. 527, 2015.
- [44] Y. Sun, S.-C. Wu, M. N. Ali, C. Felser, and B. Yan, “Prediction of weyl semimetal in orthorhombic mote_2 ,” *Phys. Rev. B*, vol. 92, 2015.
- [45] K. Deng, G. Wan, P. Deng, K. Zhang, S. Ding, E. Wang, M. Yan, H. Huang, H. Zhang, Z. Xu, J. Denlinger, A. Fedorov, H. Yang, W. Duan, H. Yao, Y. Wu, S. Fan, H. Zhang, X. Chen, and S. Zhou, “Experimental observation of topological fermi arcs in type-ii weyl semimetal mote_2 ,” *Nat. Phys.*, vol. 12, 2016.
- [46] L. Huang, T. M. McCormick, M. Ochi, Z. Zhao, M.-T. Suzuki, R. Arita, Y. Wu, D. Mou, H. Cao, J. Yan, N. Trivedi, and A. Kaminski, “Spectroscopic evidence for a type ii weyl semimetallic state in mote_2 ,” *Nat. Mater.*, vol. 15, 2016.
- [47] A. Tamai, Q. S. Wu, I. Cucchi, F. Y. Bruno, S. Riccò, T. K. Kim, M. Hoesch, C. Barreteau, E. Giannini, C. Besnard, A. A. Soluyanov, and F. Baumberger, “Fermi arcs and their topological character in the candidate type-ii weyl semimetal mote_2 ,” *Phys. Rev. X*, vol. 6, 2016.
- [48] J. Jiang, Z. K. Liu, Y. Sun, H. F. Yang, C. R. Rajamathi, Y. P. Qi, L. X. Yang, C. Chen, H. Peng, C.-C. Hwang, S. Z. Sun, S.-K. Mo, I. Vobornik, J. Fujii, S. S. P. Parkin, C. Felser, B. H. Yan, and Y. L. Chen, “Signature of type-ii weyl semimetal phase in mote_2 ,” *Nat. Commun.*, vol. 8, 2017.
- [49] X.-L. Qi and S.-C. Zhang, “Topological insulators and superconductors,” *Rev. Mod. Phys.*, vol. 83, 2011.

-
- [50] G. Xu, H. Weng, Z. Wang, X. Dai, and Z. Fang, “Chern semimetal and the quantized anomalous hall effect in HgCr_2Se_4 ,” *Phys. Rev. Lett.*, vol. 107, 2011.
- [51] Z. Fang, N. Nagaosa, K. S. Takahashi, A. Asamitsu, R. Mathieu, T. Ogasawara, H. Yamada, M. Kawasaki, Y. Tokura, and K. Terakura, “The anomalous hall effect and magnetic monopoles in momentum space,” *Science*, vol. 302, 2003.
- [52] P. Hosur and X. Qi, “Recent developments in transport phenomena in weyl semimetals,” *Comptes Rendus Physique*, vol. 14, 2013.
- [53] C. Fang, M. J. Gilbert, X. Dai, and B. A. Bernevig, “Multi-weyl topological semimetals stabilized by point group symmetry,” *Phys. Rev. Lett.*, vol. 108, 2012.
- [54] S. M. Young, S. Zaheer, J. C. Y. Teo, C. L. Kane, E. J. Mele, and A. M. Rappe, “Dirac semimetal in three dimensions,” *Phys. Rev. Lett.*, vol. 108, 2012.
- [55] S.-Y. Xu, C. Liu, S. K. Kushwaha, R. Sankar, J. W. Krizan, I. Belopolski, M. Neupane, G. Bian, N. Alidoust, T.-R. Chang, H.-T. Jeng, C.-Y. Huang, W.-F. Tsai, H. Lin, P. P. Shibayev, F.-C. Chou, R. J. Cava, and M. Z. Hasan, “Observation of fermi arc surface states in a topological metal,” *Science*, vol. 347, 2015.
- [56] H. Yi, Z. Wang, C. Chen, Y. Shi, Y. Feng, A. Liang, Z. Xie, S. He, J. He, Y. Peng, X. Liu, Y. Liu, L. Zhao, G. Liu, X. Dong, J. Zhang, M. Nakatake, M. Arita, K. Shimada, H. Namatame, M. Taniguchi, Z. Xu, C. Chen, X. Dai, Z. Fang, and X. J. Zhou, “Evidence of topological surface state in three-dimensional dirac semimetal Cd_3As_2 ,” *Sci. Rep.*, vol. 4, 2014.
- [57] M. Kargarian, M. Randeria, and Y.-M. Lu, “Are the surface fermi arcs in dirac semimetals topologically protected?,” *Proceedings of the National Academy of Sciences*, vol. 113, 2016.
- [58] A. C. Potter, I. Kimchi, and A. Vishwanath, “Quantum oscillations from surface fermi arcs in weyl and dirac semimetals,” *Nat. Commun.*, vol. 5, 2014.

- [59] S. K. Kushwaha, J. W. Krizan, B. E. Feldman, A. Gyenis, M. T. Randeria, J. Xiong, S.-Y. Xu, N. Alidoust, I. Belopolski, T. Liang, M. Z. Hasan, N. P. Ong, A. Yazdani, and R. J. Cava, “Bulk crystal growth and electronic characterization of the 3d dirac semimetal Na_3Bi ,” *APL Mater.*, vol. 3, 2015.
- [60] M. Neupane, S.-Y. Xu, R. Sankar, N. Alidoust, G. Bian, C. Liu, I. Belopolski, T.-R. Chang, H.-T. Jeng, H. Lin, A. Bansil, F. Chou, and M. Z. Hasan, “Observation of a three-dimensional topological dirac semimetal phase in high-mobility Cd_3As_2 ,” *Nat. Commun.*, vol. 5, 2014.
- [61] Z. K. Liu, J. Jiang, B. Zhou, Z. J. Wang, Y. Zhang, H. M. Weng, D. Prabhakaran, S.-K. Mo, H. Peng, P. Dudin, T. Kim, M. Hoesch, Z. Fang, X. Dai, Z. X. Shen, D. L. Feng, Z. Hussain, and Y. L. Chen, “A stable three-dimensional topological dirac semimetal Cd_3As_2 ,” *Nat. Mater.*, vol. 13, 2014.
- [62] S. Borisenko, Q. Gibson, D. Evtushinsky, V. Zabolotnyy, B. Büchner, and R. J. Cava, “Experimental realization of a three-dimensional dirac semimetal,” *Phys. Rev. Lett.*, vol. 113, 2014.
- [63] B.-J. Yang and N. Nagaosa, “Classification of stable three-dimensional dirac semimetals with nontrivial topology,” *Nat. Commun.*, vol. 5, 2014.
- [64] B.-J. Yang, T. Morimoto, and A. Furusaki, “Topological charges of three-dimensional dirac semimetals with rotation symmetry,” *Phys. Rev. B*, vol. 92, 2015.
- [65] T. Liang, Q. Gibson, M. N. Ali, M. Liu, R. J. Cava, and N. P. Ong, “Ultrahigh mobility and giant magnetoresistance in the dirac semimetalting Cd_3As_2 ,” *Nat. Mater.*, vol. 14, 2014.
- [66] J. Feng, Y. Pang, D. Wu, Z. Wang, H. Weng, J. Li, X. Dai, Z. Fang, Y. Shi, and L. Lu, “Large linear magnetoresistance in dirac semimetal Cd_3As_2 with fermi surfaces close to the dirac points,” *Phys. Rev. B*, vol. 92, 2015.

- [67] H. Li, H. He, H.-Z. Lu, H. Zhang, H. Liu, R. Ma, Z. Fan, S.-Q. Shen, and J. Wang, “Negative magnetoresistance in dirac semimetal cd_3as_2 ,” *Nat. Commun.*, vol. 7, 2016.
- [68] A. A. Burkov, “Negative longitudinal magnetoresistance in dirac and weyl metals,” *Phys. Rev. B*, vol. 91, 2015.
- [69] S. Jeon, B. B. Zhou, A. Gyenis, B. E. Feldman, I. Kimchi, A. C. Potter, Q. D. Gibson, R. J. Cava, A. Vishwanath, and A. Yazdani, “Landau quantization and quasi-particle interference in the three-dimensional diracting semimetal cd_3as_2 ,” *Nat. Mater.*, vol. 13, 2014.
- [70] J. Xiong, S. K. Kushwaha, T. Liang, J. W. Krizan, M. Hirschberger, W. Wang, R. J. Cava, and N. P. Ong, “Evidence for the chiral anomaly in the dirac semimetal na_3bi ,” *Science*, vol. 350, 2015.
- [71] E. V. Gorbar, V. A. Miransky, and I. A. Shovkovy, “Chiral anomaly, dimensional reduction, and magnetoresistivity of weyl and dirac semimetals,” *Phys. Rev. B*, vol. 89, 2014.
- [72] A. A. Burkov and Y. B. Kim, “ F_2 and chiral anomalies in topological dirac semimetals,” *Phys. Rev. Lett.*, vol. 117, 2016.
- [73] T.-R. Chang, S.-Y. Xu, D. S. Sanchez, W.-F. Tsai, S.-M. Huang, G. Chang, C.-H. Hsu, G. Bian, I. Belopolski, Z.-M. Yu, S. A. Yang, T. Neupert, H.-T. Jeng, H. Lin, and M. Z. Hasan, “Type-ii symmetry-protected topological dirac semimetals,” *Phys. Rev. Lett.*, vol. 119, 2017.
- [74] H. Huang, S. Zhou, and W. Duan, “Type-ii dirac fermions in the ptse_2 class of transition metal dichalcogenides,” *Phys. Rev. B*, vol. 94, 2016.
- [75] Y. Li, Y. Xia, S. A. Ekahana, N. Kumar, J. Jiang, L. Yang, C. Chen, C. Liu, B. Yan, C. Felser, G. Li, Z. Liu, and Y. Chen, “Topological origin of the type-ii dirac fermions in PtSe_2 ,” *Phys. Rev. Materials*, vol. 1, 2017.

-
- [76] K. Zhang, M. Yan, H. Zhang, H. Huang, M. Arita, Z. Sun, W. Duan, Y. Wu, and S. Zhou, “Experimental evidence for type-ii dirac semimetal in PtSe_2 ,” *Phys. Rev. B*, vol. 96, 2017.
- [77] B. Bradlyn, J. Cano, Z. Wang, M. G. Vergniory, C. Felser, R. J. Cava, and B. A. Bernevig, “Beyond dirac and weyl fermions: Unconventional quasiparticles in conventional crystals,” *Science*, vol. 353, 2016.
- [78] I. C. Fulga and A. Stern, “Triple point fermions in a minimal symmorphic model,” *Phys. Rev. B*, vol. 95, 2017.
- [79] G. Chang, S.-Y. Xu, S.-M. Huang, D. S. Sanchez, C.-H. Hsu, G. Bian, Z.-M. Yu, I. Belopolski, N. Alidoust, H. Zheng, T.-R. Chang, H.-T. Jeng, S. A. Yang, T. Neupert, H. Lin, and M. Z. Hasan, “Nexus fermions in topological symmorphic crystalline metals,” *Sci. Rep.*, vol. 7, no. 1, 2017.
- [80] B. Q. Lv, Z.-L. Feng, Q.-N. Xu, X. Gao, J.-Z. Ma, L.-Y. Kong, P. Richard, Y.-B. Huang, V. N. Strocov, C. Fang, H.-M. Weng, Y.-G. Shi, T. Qian, and H. Ding, “Observation of three-component fermions in the topological semimetal molybdenum phosphide,” *Nature*, vol. 546, 2017.
- [81] H. Weng, C. Fang, Z. Fang, and X. Dai, “Topological semimetals with triply degenerate nodal points in θ -phase tantalum nitride,” *Phys. Rev. B*, vol. 93, 2016.
- [82] M. K. Gaillard, P. D. Grannis, and F. J. Sciulli, “The standard model of particle physics,” *Rev. Mod. Phys.*, vol. 71, 1999.
- [83] T. T. Heikkilä and G. E. Volovik, “Nexus and dirac lines in topological materials,” *New J. Phys.*, vol. 17, no. 9, 2015.
- [84] Z. Zhu, G. W. Winkler, Q. Wu, J. Li, and A. A. Soluyanov, “Triple point topological metals,” *Phys. Rev. X*, vol. 6, 2016.
- [85] H. Weng, C. Fang, Z. Fang, and X. Dai, “Coexistence of weyl fermion and massless triply degenerate nodal points,” *Phys. Rev. B*, vol. 94, 2016.

-
- [86] G. W. Winkler, Q. Wu, M. Troyer, P. Krogstrup, and A. A. Soluyanov, “Topological phases in $\text{InAs}_{1-x}\text{Sb}_x$: From novel topological semimetal to Majorana wire,” *Phys. Rev. Lett.*, vol. 117, 2016.
- [87] A. A. Burkov, M. D. Hook, and L. Balents, “Topological nodal semimetals,” *Phys. Rev. B*, vol. 84, 2011.
- [88] C. Fang, Y. Chen, H.-Y. Kee, and L. Fu, “Topological nodal line semimetals with and without spin-orbital coupling,” *Phys. Rev. B*, vol. 92, 2015.
- [89] C. Fang, H. Weng, X. Dai, and Z. Fang, “Topological nodal line semimetals,” *Chin. Phys. B*, vol. 25, no. 11, 2016.
- [90] A. Alexandradinata, X. Dai, and B. A. Bernevig, “Wilson-loop characterization of inversion-symmetric topological insulators,” *Phys. Rev. B*, vol. 89, 2014.
- [91] J. C. Y. Teo, L. Fu, and C. L. Kane, “Surface states and topological invariants in three-dimensional topological insulators: Application to $\text{Bi}_{1-x}\text{Sb}_x$,” *Phys. Rev. B*, vol. 78, 2008.
- [92] M. Ezawa, “Symmetry protected topological charge in symmetry broken phase: Spin-charge, spin-valley-charge and mirror-charge numbers,” *Physics Letters A*, vol. 378, 2014.
- [93] H. Chen, Q. Niu, and A. H. MacDonald, “Anomalous Hall Effect Arising from Noncollinear Antiferromagnetism,” *Phys. Rev. Lett.*, vol. 112, 2014.
- [94] J. Yu, B. Yan, and C.-X. Liu, “Model hamiltonian and time reversal breaking topological phases of antiferromagnetic half-Heusler materials,” *Phys. Rev. B*, vol. 95, 2017.
- [95] S. Chadov, X. Qi, J. Kübler, G. H. Fecher, C. Felser, and S. C. Zhang, “Tunable multifunctional topological insulators in ternary Heusler compounds,” *Nat. Mater.*, vol. 9, 2010.

-
- [96] P. C. Canfield, J. D. Thompson, W. P. Beyermann, A. Lacerda, M. F. Hundley, E. Peterson, Z. Fisk, and H. R. Ott, “Magnetism and heavy fermion-like behavior in the rbipi series,” *J. Appl. Phys.*, vol. 70, 1991.
- [97] S. Khmelevskiy, “Antiferromagnetic ordering on the frustrated fcc lattice in the intermetallic compound gdptbi,” *Phys. Rev. B*, vol. 86, 2012.

Publications

- [1] **H. Yang**, M. Schmidt, V. Süß, M. Chan, F. F Balakirev, R. D McDonald, S. S P Parkin, C. Felser, B. Yan and P. J W Moll. "Quantum oscillations in the type-II Dirac semi-metal candidate PtSe₂". *New Journal of Physics*, 20, 043008 (2018).
- [2] **H. Yang**, J. Yu, S. S. P. Parkin, C. Felser, C. Liu and B. Yan. "Prediction of Triple Point Fermions in Simple Half-Heusler Topological Insulators". *Physical Review Letter*, 3, 136401 (2017).
- [3] **H. Yang**, Y. Sun, Y. Zhang, W. J. Shi, S. S P Parkin and B. Yan. "Topological Weyl semimetals in the chiralantiferromagnetic materials Mn₃Ge and Mn₃Sn". *New Journal of Physics*, 19, 015008 (2017).
- [4] S. Y. Yang, **H. Yang**, E. Derunova, S. S. P. Parkin, B. Yan and M. N. Ali. "Symmetry Demanded Topological Nodal-line Materials". *Advances in Physics: X*, 3, 1414631 (2017).
- [5] Y. Zhang, Y. Sun, **H. Yang**, J. Zelezny, S. S. P. Parkin, C. Felser and B. Yan. "Strong anisotropic anomalous Hall effect and spin Hall effect in the chiral antiferromagnetic compounds Mn₃X (X=Ge, Sn, Ga, Ir, Rh, and Pt)", *Physics Review B*, 95, 075128 (2017).
- [6] C. R. Rajamathi, U. Gupta, N. Kumar, **H. Yang**, Y. Sun, V. Süß, C. Shekhar, M. Schmidt, H. Blumtritt, P. Werner, B. Yan, S. Parkin, C. Felser and C. N. R. Rao. "Weyl Semimetals as Hydrogen Evolution Catalysts", *Advanced Materials*, 19, 1606202 (2017).

-
- [7] C. R. Rajamathi, U. Gupta, K. Pal, N. Kumar, **H. Yang**, Y. Sun, C. Shekhar, B. Yan, S. Parkin, U. V. Waghmare, C. Felser and C. N. R. Rao "Photochemical Water Splitting by Bismuth Chalcogenide Topological Insulators", *ChemPhysChem*, 18, 2322 (2017).

Acknowledgements

First and foremost, I would like to thank Prof. Dr. Stuart S. P. Parkin for his supervision and stunning support during my Ph.D. research in his group. I have benefitted a lot from his brilliance, enthusiasm and constant forward-thinking mindset during our discussions. Especially, his encouragement and continuous input of ideas to these projects have been important sources of motivation for me. It is an honor to have the opportunity to learn from him during this important stage of my professional life.

Furthermore, I'd like to thank Prof. Dr. Claudia Felser for providing me the opportunity to study at Max Planck Institute for Chemical Physics of Solids (MPI-CPfS). And I am also thankful to Dr. Binghai Yan, who directly supervised those projects when I was in MPI-CPfS. Due to his knowledge and experiences in topological materials, it was possible for me to benefit from him in every sense.

I'd like to thank all my colleagues at both the MPI-Halle and the MPI-CPfS for their help, discussions and continuous encouragement on various subjects, especially Dr. Mazhar Nawaz Ali, Prof. Philip Moll, Dr. Yan Sun and Dr. Gayles, Jacob. I am also thankful to my collaborators Prof. Chao-Xing Liu and Jiabin Yu at Penn State University.

Special thanks go to Simone Jäger and Antje Paetzold for their consistent assistance and precious suggestions. Their help makes the life in the Institute and in the University much more convenient.

I would like to acknowledge the technical support from the supercomputer center MPCDF, Udo Schmidt and Mike Borrmann. Likewise, I'd like to thank the co-workers from the administration office for their help.

Last but not least, I would like to thank my dear parents, my brother and sister, my girlfriend Jue and all of my friends here in Germany and back in China for their continuous love and encouragement. Being with them makes my life more delightful.

Curriculum Vitae

First Name: Hao
Family Name: Yang
Gender: Male
Date of Birth: 18.02.1991
Place of Birth: Jiangxi, China
Address: Ilmweg 11, Halle(Saale), Germany
Nationality: Chinese

ACADEMIC EDUCATION

08/2015-present *Doctor of Natural Sciences in Physics*
Martin-Luther-University Halle-Wittenberg, Halle, Germany

09/2012-07/2015 *Master's Degree in Materials Science and Engineering*
Tsinghua University, Beijing, China

09/2008-07/2012 *Bachelor's Degree in Materials Physics*
Nanjing University, Nanjing, China

Hao Yang
Weinberg 2, 06120 Halle(Saale), Germany
22.02.2019

Eidesstattliche Erklärung

Hiermit erkläre ich, Hao Yang, dass ich die vorliegende Arbeit mit dem Titel: **Investigation of novel quasiparticles in topological materials** in allen Teilen selbständig verfasst und keine anderen als die angegebenen Quellen und Hilfsmittel benutzt habe. Alle wörtlich oder sinngemäß übernommenen Textstellen habe ich als solche kenntlich gemacht.

Ferner liegen gegen mich weder gerichtliche Vorstrafen vor, noch sind staatsanwaltliche Ermittlungen oder Disziplinarverfahren eingeleitet worden.

Des Weiteren erkläre ich hiermit, dass ich bisher keine andere Arbeit zur Promotion eingereicht noch mit einer anderen Arbeit den Versuch zur Promotion unternommen habe.

Weingberg 2, 06120 Halle(Saale), Germany

den 22. Feb. 2019

Hao Yang